DESIGN AND IMPLEMENTATION OF THE NEW YORK STATE MESONET FLUX TOWER NETWORK

by

Jason Michael Covert

A Thesis

Submitted to the University at Albany, State University of New York

in Partial Fulfillment of

the Requirements for the Degree of

Master of Science

College of Arts & Sciences

Department of Atmospheric and Environmental Sciences

2019

ABSTRACT

The New York State Mesonet (NYSM) was established in 2014 to provide high-quality real-time meteorological data for weather monitoring and forecasting, emergency management, and research aimed at improving numerical weather prediction. The mainstay of the network consists of 126 surface weather stations located throughout New York State with an average spacing of 30 km. In 2017, 17 of the sites ("flux" sites) were equipped with additional (permanent) instrumentation to measure short and long-wave radiation components, soil heat flux, and turbulent fluxes of momentum, sensible and latent heat, and carbon dioxide (CO_2). The mesoscale resolution of the 17-site NYSM Flux Tower Network is distinctive among existing flux tower networks. The data have potential to improve surface parameterizations in numerical weather models as well as to address many research questions related to the surface energy and carbon budgets, ecosystems and agriculture, hydrology, and surface layer exchange processes. This thesis presents site selection, instrumentation, data acquisition, flux computations, quality control, and operation protocols of the NYSM Flux Tower Network. Data from the first two years of operation are used to evaluate the land cover representation of measured fluxes, examine spatial and temporal variability of surface fluxes and CO_2 concentration, and assess surface energy budget closure.

ACKNOWLEDGEMENTS

I would like to thank my advisor, Dr. Scott Miller, for helping me achieve this milestone. I am grateful for the guidance he has provided on this research, his patience, and genuine commitment to my professional development. I am also appreciative of Dr. Jeffrey Freedman and Dr. David Fitzjarrald. Their suggestions and feedback on my research have undoubtably added value to this work and have helped me improve as a researcher.

The establishment of the New York State Mesonet Flux (NYSM) Flux Tower Network would not have been possible without a team of highly dedicated technicians, scientists, engineers, and administrative staff. I wish to thank Nicholas Farruggio, with whom I've worked closely, to install, maintain, and enhance the flux network. I am grateful for the technical advice and assistance of John Sicker and Janie Schwab, whose expertise was essential in preparing the flux network for deployment. I must also acknowledge the past and continued contributions of NYSM personnel, Jerald Brotzge, Nathan Bain, Junhong Wang, Steven Perez, and Edward Kane Jr.

Original funding for the NYSM was provided by Federal Emergency Management Agency grant FEMA-4085-DR-NY, with the continued support of the New York State (NYS) Division of Homeland Security & Emergency Services; NYS; the Research Foundation for the State University of New York (SUNY); the Atmospheric Sciences Research Center (ASRC); and the Department of Atmospheric and Environmental Sciences at the University at Albany. This masters research was made possible, in part, by a first-year graduate student fellowship provided by the ASRC.

Finally, I must thank my friends and family for their continued support through the challenges of my scientific career thus far. I could not have made it this far without you.

TABLE OF CONTENTS

CHAPTER 1:

Introduction

The exchange of momentum, water (H_2O), heat, and carbon dioxide (CO_2) between the earth's surface and the atmosphere is crucial to planetary boundary layer (PBL) processes that influence weather and climate. As wind flows across landscapes, momentum continuously is lost to the rough surface (Taylor and Shaw 1915). Water evaporates from the surface and transpires from vegetation to be mixed throughout the PBL (Geiger 1950). The air temperature distribution in the PBL is influenced by the surface energy budget — the amount of energy reaching the surface, being absorbed into the soil, and being drawn away and reflected in the form of heat and radiation (Stull 1988). The surface energy budget is influenced by clouds which are products of moisture and heat originating from the surface (Stull 1988). Clouds cause precipitation, modulate surface temperature, and affect carbon exchange in vegetated ecosystems (Freedman et al. 2001; Garrett 1982). CO_2 flux plays a role in regulating global climate and can be an indicator of ecosystem productivity (Trenberth et al. 2014; Miller et al. 2004).

Fluxes of momentum (τ), latent heat (LE), sensible heat (H), and trace gasses such as carbon dioxide (FC), are predominantly driven by turbulence (Stull 1988). Turbulence is generated by either shear or buoyancy in the atmosphere (Stull 1988). The interaction of slow-moving air near the surface and fast-moving air above produces turbulence by shear. Buoyant air parcels, warmed by conduction at the surface, lift and displace cooler air above that is then forced to descend. This convective motion creates eddies whose length scale may be on the order of a kilometer or more (Stull 1988). Large eddies cascade into smaller and weaker eddies, as Lewis Fry Richardson elegantly describes in his poem:

"Big whorls have little whorls that feed on their velocity,

And little whorls have lesser whorls and so on to viscosity."

Turbulent eddies of all sizes mix quantities throughout the PBL and thus enable the interaction between earth's surface and the atmosphere (Stull 1988).

Turbulent fluxes can be directly measured using the eddy covariance (EC) method (Swinbank 1951). The turbulent fluxes of interest in this research are

$$\text{Momentum flux:} \quad \tau = -\overline{\rho_d}\overline{u'w'}, \tag{1}$$

$$\text{Latent heat flux:} \quad LE = \overline{\rho_d}\bar{L}_v\overline{w'q'}, \tag{2}$$

$$\text{Sensible heat flux:} \quad H = \overline{\rho_d}C_p\overline{w'T'}, \text{ and} \tag{3}$$

$$\text{CO}_2\text{ flux:} \quad FC = \overline{\rho_d}\overline{w'C'}\ , \tag{4}$$

where dry air density is ρ_d, latent heat of vaporization is L_v, the specific heat of dry air is C_p, horizontal and vertical wind are given by *u* and *w* respectively; the water vapor mixing ratio is *q*; the air temperature is T; and CO_2 mixing ratio is *C*. The primes denote perturbations away from the mean. For example, $w' = \overline{w} - w$, where $\overline{w}$ is the average vertical wind velocity over the flux averaging period and w is the instantaneous wind velocity.

The covariance of *w* and a given quantity (e.g. *q*) is proportional to the vertical flux of the quantity. The quantities, *u*, *q*, T, and *C* are typically measured at frequencies ≥ 10 Hz (Aubinet et al. 2012). The covariances are averaged over a period long enough to sufficiently capture all eddy frequencies that contribute to the flux. The averaging period for operational flux measurements is typically 30 minutes, but can be longer to capture low frequency contributions to fluxes (Sakai et al. 2002).

Figure 1.1 depicts daytime surface fluxes in an idealized grassy field. Net radiation (R_n) is defined as the net amount of energy leaving and being absorbed by the surface,

$$R_n = SW\downarrow - SW\uparrow + LW\downarrow - LW\uparrow, \tag{5}$$

where SW is shortwave radiation (300 nm – 2800 nm) and LW is longwave radiation (4.5 μm – 42 μm). The arrows are indicative of the direction of the radiation relative to the surface. Shortwave radiation from the sun penetrates the atmosphere and is absorbed and reflected at the surface, depending on the albedo (α) of the land cover. Some energy is emitted back into the atmosphere by LW radiation and some is absorbed from LW radiation emitted from the sky. A positive R_n indicates a net radiation flux into the surface and a negative R_n indicates a net radiation flux out of the surface.

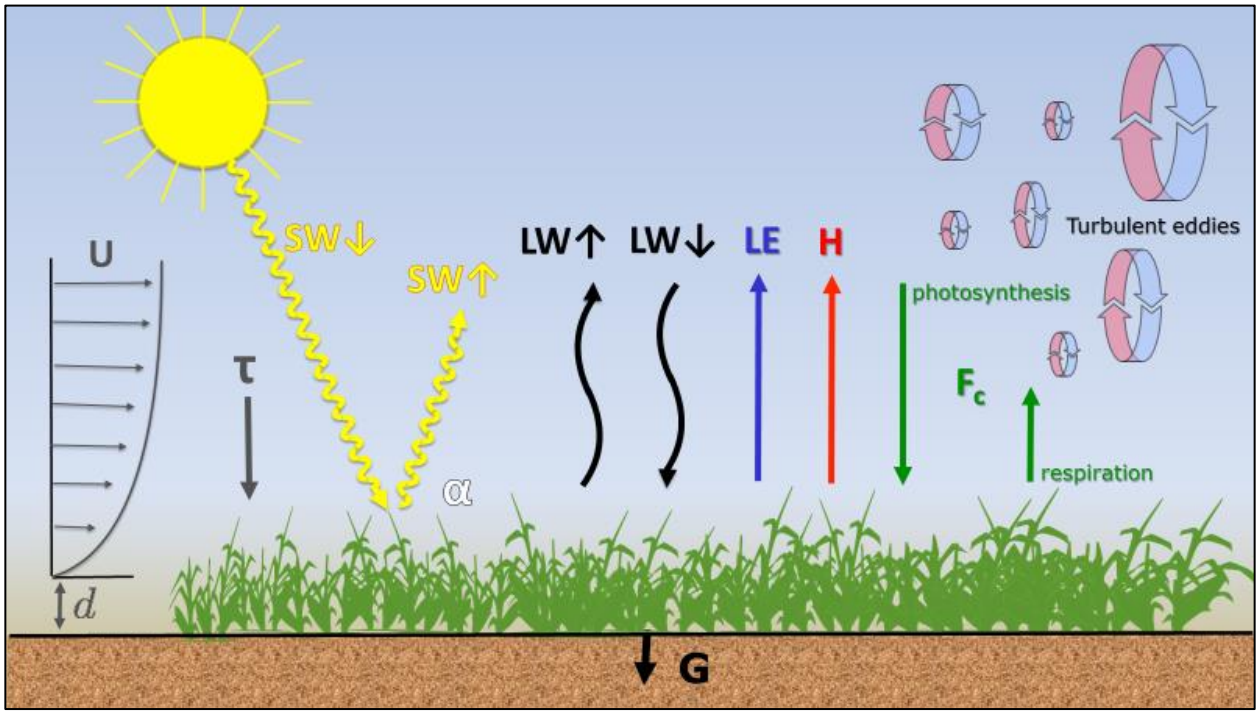

Figure 1.1. A depiction of surface fluxes during the day in an idealized grassy field.

The energy received by the earth's surface from the sun must be conserved. Assuming no advection of heat, the surface energy budget is given by,

$$0 = R_n - G - LE - H, \tag{6}$$

where the ground heat flux (G) is the amount of energy dissipated into the soil. Ground heat flux uses the same sign convention as R_n. A positive G indicates a downward heat flux into the soil and a negative G indicates an upward heat flux toward the surface. Latent heat is drawn away from the surface by LE when H_2O evaporates and transpires. Sensible heat is removed from the surface by eddies and is drawn away by H. Positive LE and H is directed up and away from the surface and a negative H and LE is directed down toward the surface.

Measured EC fluxes can be used to develop improved representations of fluxes in numerical weather prediction (NWP) models. Biases in LE, H, and τ, calculated within NWP model PBL schemes, contribute to inaccurate weather predictions (Cohen et al. 2015; Nielsen-Gammon et al. 2010). Current operational NWP models are incapable of resolving PBL turbulence in a timeframe that is suitable for weather forecasting. NWP models often assume complete surface energy budget closure, but are unable to account for small scale temporal and spatial phenomena that affect surface fluxes (Cuxart et al. 2015). Sub-grid phenomena, such as localized advection of heat or shading from clouds, can impact the weather at the surface, but remain unresolved by models (Cuxart et al. 2015).

In agricultural environments, EC flux measurements are used to monitor evaporative water losses from fields (Lee 2018). Knowledge of evapotranspiration occurring in agricultural fields gives farmers the ability to modulate water use according to need, thereby improving the efficiency of water use. Conventionally, evapotranspiration is estimated using parameterizations

that utilize commonly measured meteorological variables (e.g. Penman 1948; Monteith 1965). Evapotranspiration measured directly using EC has operational value and plays a role in developing and evaluating such parameterizations in hydrological models (e.g. Fang et al. 2016).

Anthropogenic CO_2 emissions have resulted in a global radiative imbalance that is causing tropospheric air temperature to increase (Trenberth et al. 2014). Terrestrial biospheres are essential components of the global carbon budget due to their ability to act as both sources and sinks for carbon (Wallace and Hobbs 2006). Multi-year deployments of EC towers have improved our understanding of how carbon exchange varies across temporal scales and over an increasingly diverse set of ecosystems (Baldocchi 2003). CO_2 flux measurements are critical to our ability to learn how land cover change and anthropogenic activities affect the carbon cycle (e.g. Sakai et al. 2004; Miller et al. 2011; Davis et al. 2017).

The Ameriflux network was founded in 1997 to facilitate data sharing among EC flux towers distributed throughout North and South America. FLUXNET was established to accomplish a similar goal, on a global scale, by combining regional flux tower networks such as Ameriflux and Euroflux (Baldocchi et al. 2001). Flux networks like Ameriflux and FLUXNET are conglomerations of hundreds of flux towers operated by independent researchers and organizations. Flux towers in these networks, mostly funded by research grants, are built to meet specific scientific goals (Baldocchi 2003). This has the advantage of diversifying the dataset, particularly regarding land cover representation. However, inconsistencies in instrumentation, tower design, maintenance protocols, and corrections applied to fluxes lead to uncertainties in the data that can make analysis and site intercomparisons challenging (Schmidt et al. 2012).

1.1 Mesoscale Weather Station Networks (Mesonets)

Mesoscale weather phenomena, such as thunderstorms, occur on a spatial scale of a few kilometers up to several hundred kilometers. The word *mesonet* is a combination of *mesoscale* and *network*, which reflect the horizontal extent of the stations and their interconnection aimed at resolving mesoscale weather phenomena. The weather stations typically measure barometric pressure, air temperature, relative humidity, wind speed, wind direction, insolation, and precipitation from a tripod or tower ranging in height between 2 and 10 meters (Mahmood et al. 2017). In 2017, there were 28 mesonets throughout the United States including 1619 weather stations (e.g. the Oklahoma Mesonet) (Mahmood et al. 2017; McPherson et al. 2007).

The implementation of a mesonet typically entails many logistical hurdles, such as executing land-use agreements with landowners, site preparation and tower installation, design of power, data acquisition and communications systems, and establishment of maintenance and repair protocols. Because these same resources are required for EC measurements, mesonets can be an efficient and economical platform for EC flux systems. In Oklahoma, Brotzge et al. (1999) instrumented 10 mesonet stations to measure EC sensible heat flux, net radiation, and soil heat flux which proved valuable for identifying sources of error in the closure of the surface energy budget (Brotzge and Crawford 2003; Brotzge 2000).

1.2 New York State Mesonet (NYSM)

The New York State Mesonet (NYSM) is a network of 126 weather stations (“standard sites”) distributed throughout New York State (NYS) as part of the Early Warning Weather Detection System established by the NYS Division of Homeland Security and Emergency Services. Initial funding came from the Federal Emergency Management Agency in response to the back-to-back disasters associated with Hurricanes Irene and Sandy. The primary goal of the

NYSM is to improve weather monitoring and forecasting in New York. The NYSM is overseen by the Research Foundation of the State University of New York (SUNY).

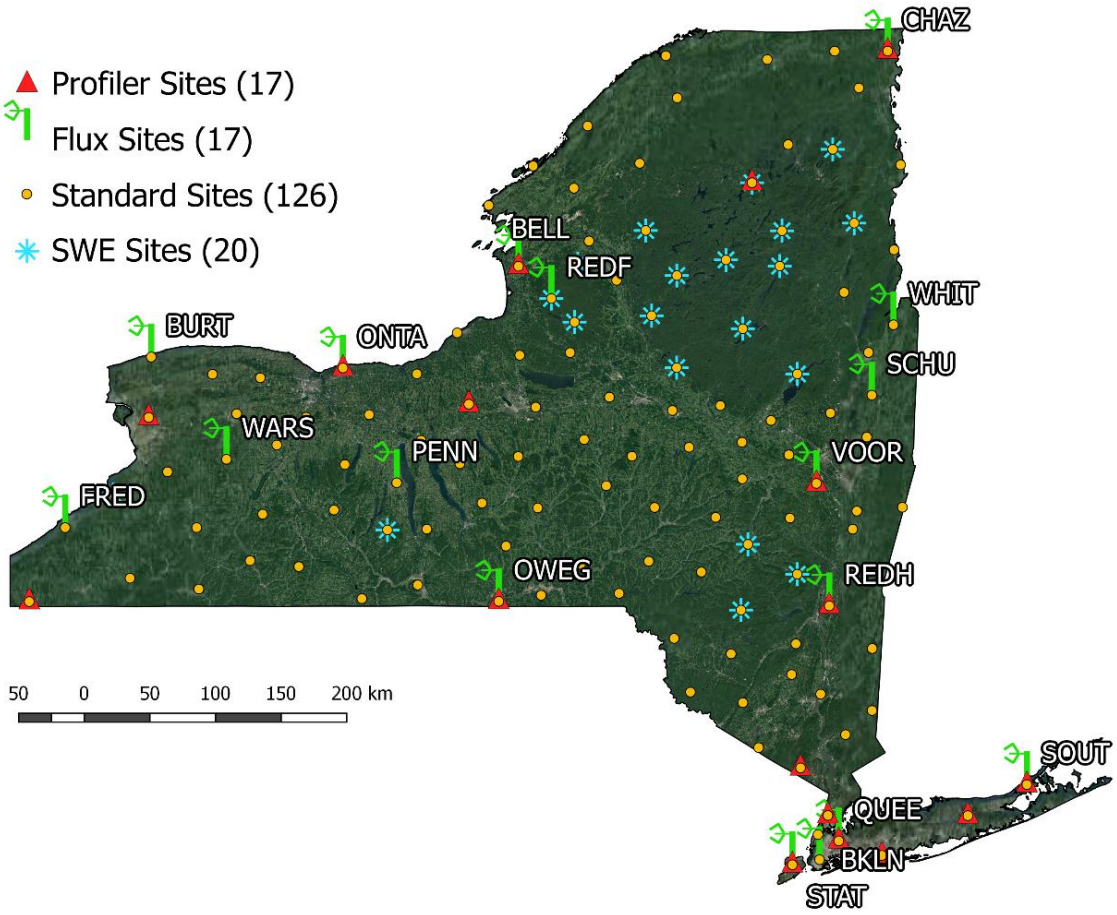

Figure 1.2: New York State Mesonet site locations placed over visible satellite imagery of New York State. Imagery is from Google Maps API.

Each NYSM weather station includes a 10 meter folding tower with instrumentation to measure barometric pressure, air temperature at 2 m and 9 m, relative humidity, wind speed and direction, insolation, precipitation, snow depth, and soil moisture, and temperature at three depths (Brotzge et al. 2016). Instrument specifications are listed in Table 1.1. At least one station is located in all 62 NYS counties with an average spacing of 30 kilometers (Dr. Jerald Brotzge,

personal communication). Stations are generally located in fields away from obstructions that may influence wind measurements. The stations were installed between August 2015 and February 2018. An example station is shown in Figure 1.3.

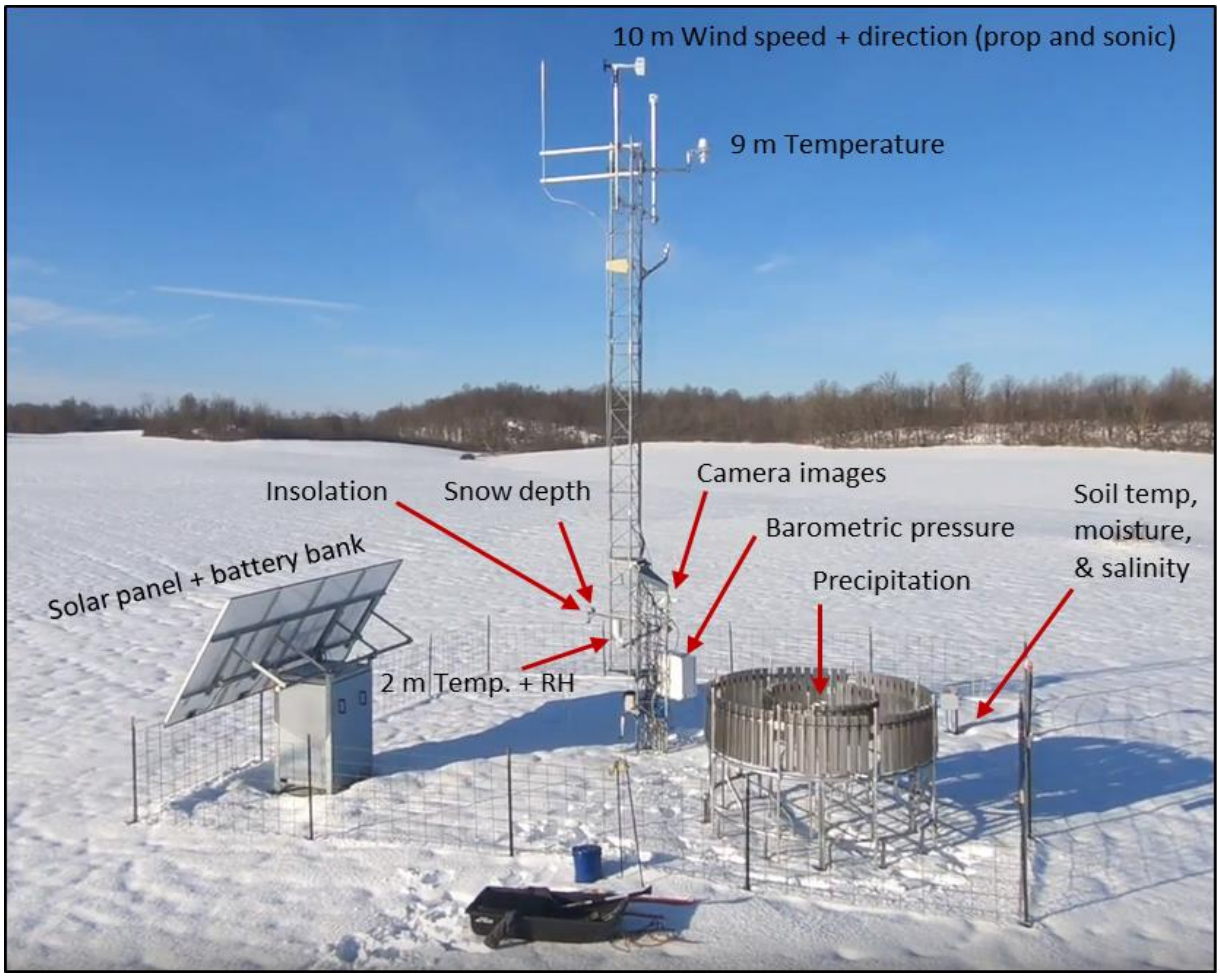

Figure 1.3: Standard NYSM site. Photo of the Philadelphia, NY standard site courtesy of NYSM Lead Technician, Scott McKim.

In addition to the 126 standard sites, the NYSM operates three sub-networks: 17 profiler sites, 20 snow sites, and 17 flux sites. At each of the seventeen profiler sites, temperature, relative humidity, and liquid water content profiles up to 10 km above ground level (AGL) are estimated using a Radiometrics MP-3000 series microwave radiometer, and wind speed and direction are estimated up to 3000 m AGL by a Leosphere Windcube 100S scanning lidar. The

snow sites include a Campbell Scientific CS725 to measure snow water equivalent. The flux sites include instrumentation to collect the measurements required to calculate τ, LE, H, FC, R_n, and G. Nine flux sites are co-located with profiler sites and one site exists at a snow site.

Table 1.1. NYSM instrument specifications

Measurement	Instrument	Units	Accuracy	Resolution	Sampling Interval
Standard Sites					
Irradiance	Licor LI-200X	Wm^{-2}	±3%[1]	0.1	3 s
10 m air temperature	RM Young 41342 w/ RM Young 43502-24V	°C	±0.3[2]	0.1	3 s
2 m air temperature	RM Young 41342 w/ RM Young 43502-24V	°C	±0.3[3]	0.1	s
9 m air temp 2 m relative humidity	Vaisala HMP155A w/ RM Young 41005-5	°C % RH	±0.3[3] ±1[4]	0.1 0.1	3 s
Barometric pressure	Vaisala PTB330	hPa	±0.20[5]	0.01	12 s
10 m Wind speed (sonic) 10 m Wind direction (sonic)	Lufft V200A	ms^{-1} degrees	±0.2[6] ±3[7]	0.1 0.1	3 s
10 m Wind speed (prop) 10 m Wind direction (vane)	RM Young 05103-5	ms^{-1} degrees	±0.3 or ±1%[8] ±3[8]	0.1 0.1	3 s
Precipitation accumulation	Ott Pluvio^2-1500	mm	±0.1 or ±1 %	0.1	60 s
Soil moisture Soil temperature	Stevens Hydra Probe II	WFV* °C	± 0.01[9] ± 0.3	0.001 0.1	12 s
Snow depth	Campbell Scientific SR-50A	cm	±1 or 0.4%[10]	0.025	60 s
Snow Sites					
Snow water equivalent	Campbell Scientific CS725	mm	±15 or ±15%	1 mm	6 h**
Profiler Sites					
Up to 7 km max wind speed/direction profile	Leosphere Windcube 100S	ms^{-1}	-	± 0.5 ms^{-1}	~5 min
0–10 km max temperature, RH, and liquid profile	Radiometrics MP-3000 series	°C/ %RH/ gm^{-3}	-	-	~2.5 min

* water fraction by volume
**continuous integration throughout interval
Conditions for accuracy as stated
1: ±3% typical; ±5% maximum in natural daylight
2: at 0 °C
3: Total accuracy between -40°C and 60°C; best accuracy of ±0.1°C achieved at 20°C
4: at 0-90% RH and 20°C; ±1.7% RH 90-100% RH and 20°C
5: at 20 °C 6 ±0.2m/s or ±2% RMS of reading (whichever is greater) at 0–6 5m/s, otherwise ±5%
7: when wind speed is > 1.0 ms-1
8: thresholds for windspeed is 1 ms-1; 1.1 ms-1 for wind direction
9: for most soils
10: of distance to target, whichever is greater. Excludes errors in the temperature compensation

1.3 Organization of Thesis

This thesis is focused on the design and implementation of the flux site sub-network of the NYSM (i.e. Flux Tower Network). Chapter 2 describes site selection, instrumentation, data acquisition, power management, flux calculations, quality control, and maintenance protocol for the network. Chapter 3 presents data recovery rates, flux quality grades, and flux footprints for each site. Preliminary results in Chapter 4 reveal observed seasonal, diurnal, inter-site, and regional variability in τ, H, LE, and FC. Energy budget closure is also presented. Chapter 5 discusses potential research opportunities and future work associated with the Flux Tower Network ("Flux Network" herein). A summary and concluding remarks are provided in Chapter 6.

CHAPTER 2:

Methods

The first flux site was installed in Voorheesville NY, in March 2017 and the network was fully operational by July 2017. The flux sites are listed in Table 2.1. Herein, individual flux sites will be referred to by their four-letter identifiers (e.g. VOOR).

Table 2.1: Flux site metadata

Site Name	ID	Latitude	Longitude	Site Description	Mesonet Site Type	Install date (dd/mm/yyyy)
Belleville	BELL	43.78962	-76.11373	Grass/ Crop field	Profiler (350 m WSW *)	05/15/2017
Brooklyn	BKLN	40.63176	-73.95368	Urban	NYC Standard	05/18/2017
Burt	BURT	43.31699	-78.74903	Vineyard/ Crop field	Standard	03/10/2017
Chazy	CHAZ	44.89565	-73.46461	Crop field	Profiler (752 m SE*)	03/17/2017
Fredonia	FRED	42.41817	-79.3666	Vineyard	Standard	06/28/2017
Ontario	ONTA	43.25941	-77.37331	Orchard	Profiler (3.2 km E*)	03/08/2017
Owego	OWEG	42.02571	-76.25543	Grassy field	Profiler (213 m SE*)	04/05/2017
Penn Yan	PENN	42.65578	-76.98746	Crop field	Standard	05/23/2017
Queens	QUEE	40.73434	-73.81586	Urban	NYC Profiler (10 m*)	04/18/2017
Redfield	REDF	43.62218	-75.87769	Grassy field	Snow	04/11/2017
Red Hook	REDH	42.00168	-73.88391	Grass/ Orchard	Profiler (206 m S*)	03/06/2017
Schuylerville	SCHU	43.11700	-73.57828	Grassy field/ Canal	Standard	02/27/2017
Southold	SOUT	41.04018	-72.46586	Vineyard	Profiler (23.6 km SE*)	05/10/2017
Staten Island	STAT	40.60401	-74.1485	Suburban	NYC Profiler (10 m*)	05/03/2017
Voorheesville	VOOR	42.65242	-73.97562	Orchard	Profiler (17.4 km NE*)	02/13/2017
Warsaw	WARS	42.77993	-78.20889	Crops/ Wind farm	Standard	06/29/2017
Whitehall	WHIT	43.48507	-73.42307	Grassy field/ Canal	Standard	02/27/2017

*Distance between flux tower and co-located vertical profiler

2.1 Siting

Of all the standard sites, 17 were chosen for installation of flux systems. We sought to locate flux systems in areas that were representative of NYS land surface types, conducive to the eddy covariance technique, distinctive among other sites, and co-located with profiler or snow sites. All NYSM sites were evaluated based on their land cover surroundings, obstruction proximity and significance, and terrain within 1000 m of the tower.

The distribution of land cover in NYS is shown in Figure 2.1a. Since the flux systems would be mounted to existing NYSM towers, EC instrumentation could not be placed higher than 9 m above ground level (agl). This constraint limited the NYSM's ability to sample fluxes from forests, which cover 60% of the state (Homer et al. 2015). However, a representative dataset of non-forested land cover is achievable (Figure 2.1a).

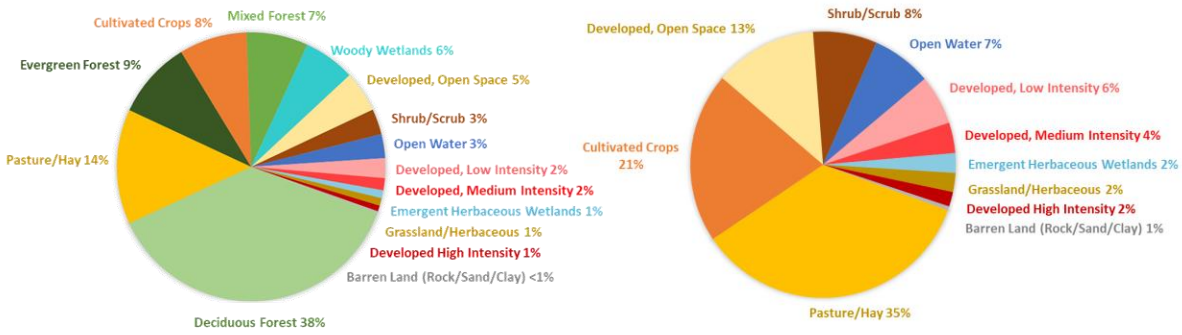

Figure 2.1. (a) Land cover distribution in NYS. (b) Land cover distribution in NYS without forests or woody wetlands. Distributions were determined using 2011 National Land Cover Database (NLCD 2011), which is a 30 m resolution, satellite derived, representation of land cover types across the United States (Homer et al. 2015).

Land cover type surrounding each NYSM site was classified by reviewing photographs and satellite images of the area contained within three ranges of distance from the tower; 0–100 m, 101–500 m, and 501 m–1000 m. During this process, potential wind obstructions were identified. Wind flow distortion, caused by obstructions such as trees or buildings, can cause

biases in the flux measurements (Munger et al. 2012). Given the height limitation of the flux towers, objects over 5 meters tall were considered potential obstructions. To estimate the potential for flow distortion, NYSM sites were scored based on the approximate quantity and significance of obstructions within 500 m of the tower. Each site was given one score per quadrant (Figure 2.2a) using the methodology in Table 2.2. Some discretion was required to identify obstructions because object size and quantity could not be precisely determined from satellite imagery or photographs. Sites with unobstructed fetches were desirable.

Table 2.2: Scoring method for comparing flow distortion potential at NYSM sites

Flow distortion potential	**Score***	**Number of obstructions ** within 100 m of tower**	**Number of obstructions 101–500 m from tower**
High	0	>4	≥50
Moderate	1	<4	<50
Low	2	<2	<25
Negligible	3	No obstructions	No obstructions

*Score defaults to whichever range from tower is worse

**1 obstruction ~ 1 mature maple tree with branches spanning 5 meters from the trunk

An 80 m resolution digital elevation model (DEM) was sourced for computing terrain statistics within 500 m and 1000 m of the NYSM towers. Buffer polygons were generated from the geographic coordinates of the towers and were used as input for ESRI ArcMap's slope tool to compute mean and standard deviation of terrain slope (Burrough and McDonell 1998). The mean and standard deviation of the slope within 500 m and 1000 m was calculated for each site. These metrics provided an indicator of terrain complexity (results in Appendix A). For example, terrain slope within 1000 m of the Sherburne standard site is shown in Figure 2.2b. Sherburne was subsequently rejected due to concern that the terrain may induce drainage flows to the tower, which would make the flux measurements difficult to interpret (Munger et al. 2012). The mean and standard deviation of terrain slope is 5.1° and 5.2° respectively.

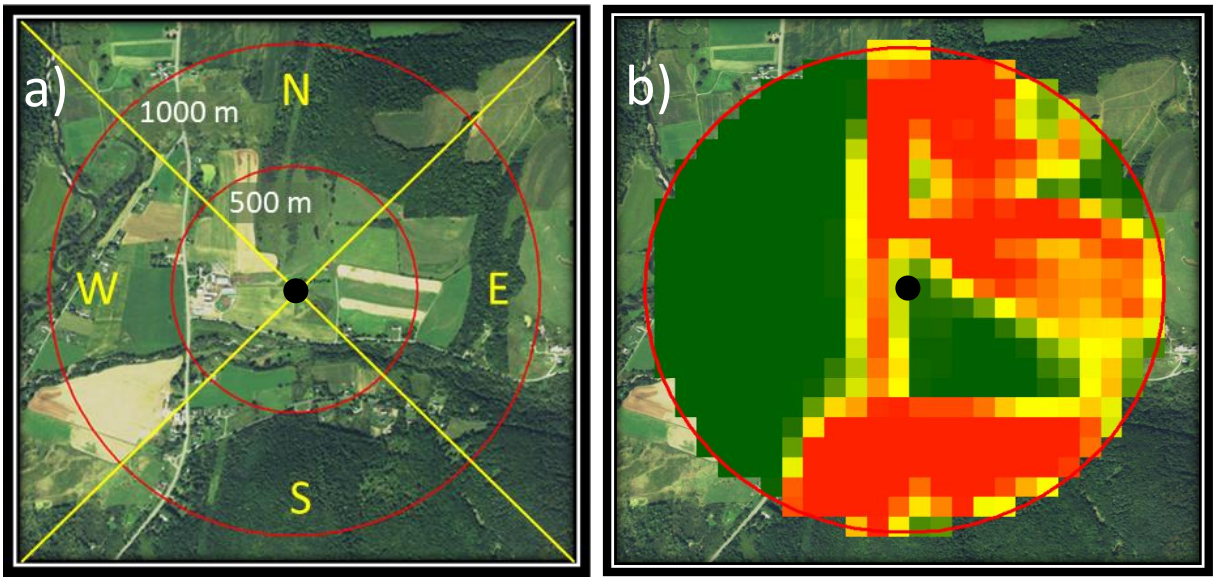

Figure 2.2. (a) Visible satellite imagery of the Sherburne, NY standard site with quadrants and rings corresponding to a 500 m and 1000 m radius from the tower. The black dot corresponds to the location of the tower. (b) The slope of terrain computed using ESRI ArcMap slope tool with an 80 m digital elevation model. The maximum slope of 20º is indicated by the deepest red and the minimum slope of 0º is indicated by the dark green.

A committee weighed site characteristics to finalize the locations of the seventeen flux sites. Sites that were co-located with snow or profiler sites were desirable because of potential research opportunities. Four sites (REDF, QUEE, BKLN, and STAT) had relatively high flow distortion potential due to nearby obstructions. However, REDF was chosen due to its status as a snow site and its location in the Tug Hill Plateau downwind of Lake Ontario which is subject to extreme snowfall. The New York City (NYC) sites (QUEE, BKLN, and STAT) had low scores because of flow distortion potential from surrounding buildings. While interpretation of measured fluxes from these sites will be challenging, they were selected for their potential value in monitoring urban CO_2 concentrations and studying atmospheric dispersion.

2.2 Instrumentation

A photo of a standard site that was enhanced with flux instrumentation is shown in Figure 2.3.

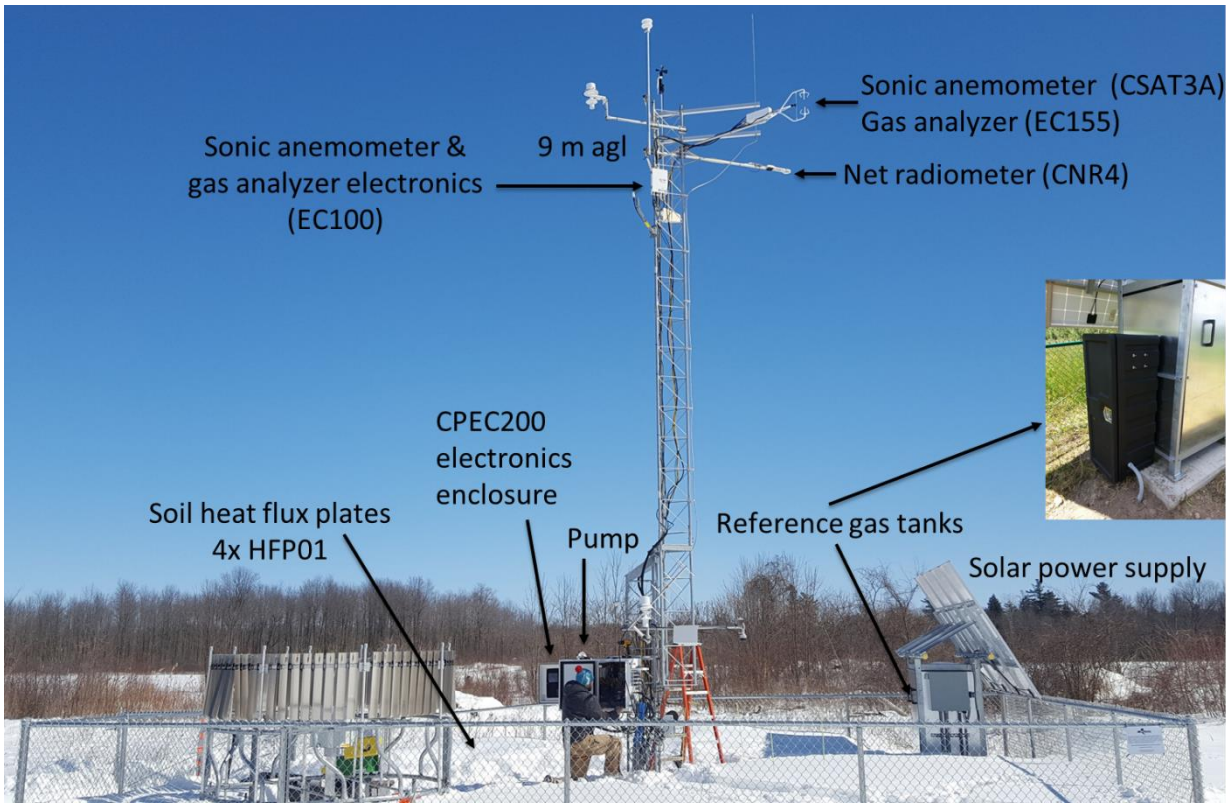

Figure 2.3. A typical NYSM flux site. Chazy (CHAZ) site shown.

The site consists of a 10 ×10 m fenced in area with a 10 meter tall Rohn 25 fold-over tower at the center. Each flux site includes an InfraRed Gas Analyzer (IRGA), an ultrasonic (sonic) anemometer, a four-component net radiometer, and four soil heat flux plates. The flux sensors were integrated into the standard site with minimal modification to the existing infrastructure. Power and communications infrastructure established at the standard site were also used for the flux sensors, namely a 550 Ahr battery bank charged by a 1,300 – 1,580-Watt solar panel array.

Two-way communication with the flux system is facilitated by the standard site's cellular modem.

The flux system electronics box and the IRGA's pump are mounted near the base of the tower, alongside the standard mesonet electronics box. Two reference CO_2 gas cylinders are stored in an enclosure attached to the side of the battery bank enclosure. Two 6.4 mm diameter Synflex (Dekabon) tubes are routed from the cylinders, through conduit, to the flux system enclosure. The HFP01 Soil heat flux plates are buried at the northwest corner of the fenced in an area, 1 meter south of the NYSM soil temperature sensors.

2.2.1. Net Radiometer

A four-component net radiometer (Kipp & Zonen CNR4) was mounted to the tower at a height of 9 m above ground level (agl). At non-NYC sites, the net radiometer is mounted to face the southeast (150º) and the IRGA and sonic anemometer is mounted to face southwest (210º). The surface field of view for the net radiometer is a circular area with a radius of 34 meters (Figure 2.4b). The CNR4 includes upward and downward facing thermopile pyranometers sensitive to SW between wavelengths of 300 and 2800 nm, and upward and downward facing thermopile pyrgeometers to measure LW between 4.5 and 42 μm. The bottom pyranometer measures reflected SW with a 150° field of view, and the top pyranometer measures downward SW with a 180° field of view. The mV signals from the pyranometers are converted to SW (Wm^{-2}) by

$$SW = mV_{pyranometer} * \frac{1000}{C_f}, \quad (9)$$

where $mV_{pyranometer}$ is the pyranometer output and C_f is the factory calibration coefficient. Longwave radiation is calculated from the pyrgeometer mV signal as

$$LW = mV_{pyrgeometer} * \frac{1000}{C} + \sigma {T_{nr}}^4 \,, \tag{10}$$

where T_{nr} is the temperature of the pyrgeometer and σ is the Stephen-Boltzman constant (5.670367×10^{-8} $Wm^{-2}K^{-4}$). The pyrgeometer sensor temperature is measured using a thermistor embedded in the net radiometer's body, adjacent to the pyrgeometers. The thermistor temperature can be found in units of K using Equations 11 through 13;

$$T_{nr} = (\mathrm{A} \cdot \mathrm{B}\ln_R \cdot \mathrm{C}{\ln_R}^3)^{-1} \tag{11}$$

$$\ln_R = \log\frac{1000 \cdot X}{1-X} \tag{12}$$

$$X = \frac{R_S}{R_S+R_f} \tag{13}$$

where A, B, and C are Steinhart-Hart coefficients (1.0295e-3, 2.3910e-4, and 1.5680e-7) that fit a line that runs through the points, 233°K, 293°K, and 353°K (Campbell Scientific Inc. 2017; Steinhart and Hart 1968).

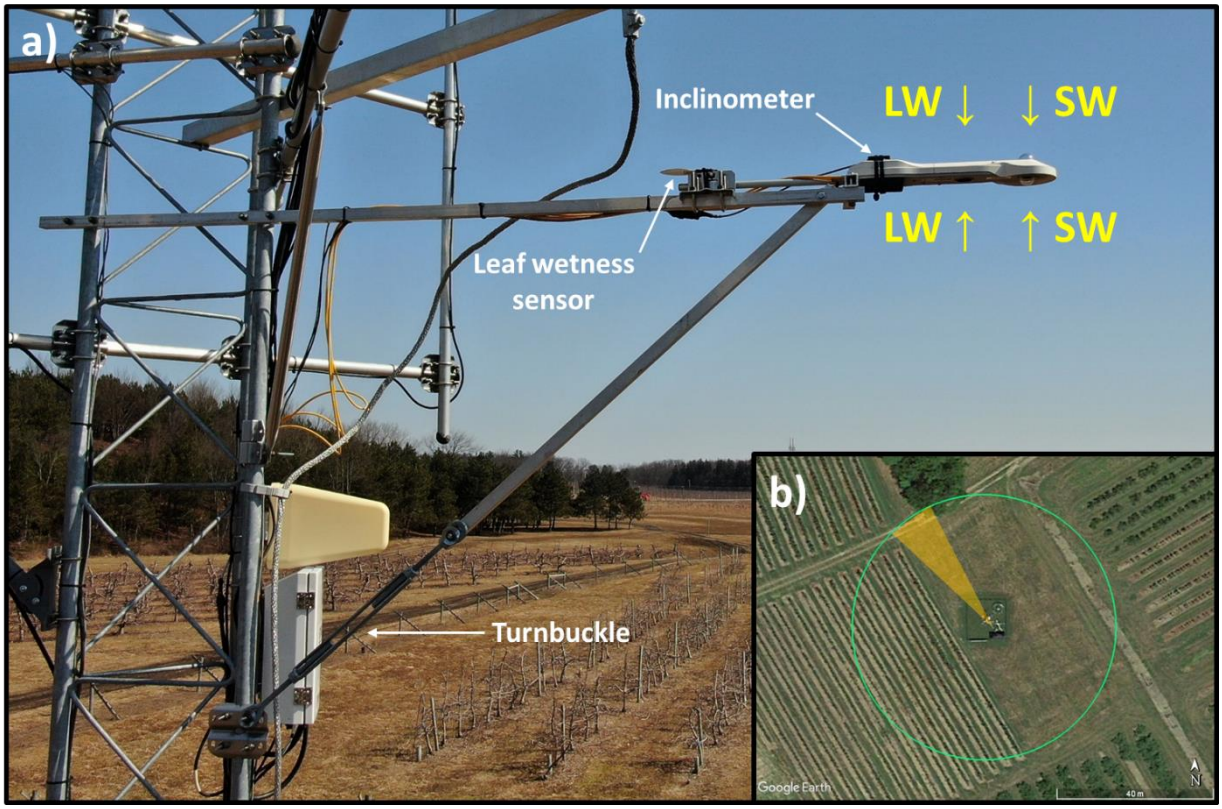

Figure 2.4. (a) A Kipp & Zonen CNR4 net radiometer installed at 9 m AGL on the VOOR flux tower using a custom square-tube mounting system. (b) The green circle indicates the 34 m radius footprint of upward SW and LW measurements. The yellow triangle indicates the approximate area where the footprint is compromised because of the net radiometer's location relative to the tower. Photo courtesy of NYSM technician Nicholas Farruggio.

The net radiometers include an optional heater/ventilator to remove dew and frost, which can cause biases in the radiation measurements (Michel et al. 2008). The ventilator draws 15 W to blow heated air over the sensor domes. Since the mesonet sites are solar powered, it is not feasible to operate the heater and ventilator continuously; instead, they are only used when dew or frost is detected. A dielectric leaf wetness sensor (LWS, Decagon) is used to identify when atmospheric conditions support dew or frost deposition. The LWS outputs a voltage proportional to the capacitance of the material (e.g. water) on its surface (Savage 2012). Table 2.3 shows how the LWS output is used to determine when to turn on the ventilator. When the LWS output voltage is below 274 mV, the sensor surface is dry (Campbell Scientific Inc. 2018). For $T_{nr} \leq$

$0°C$ and LWS between 274 mV and 284 mV, frost may be present, and when $T_{nr} > 0°C$ and LWS voltage is between 274 mV and 340 mV, dew may be present (Savage 2012). If the conditions exist for dew or frost, the ventilator will turn on until those conditions subside. The ventilator remains off in dry, rainy, or snowy conditions.

Table 2.3: LWS dependent operation of CNR4 ventilator operation

Surface Condition on LWS	LWS voltage (mV)	T_{nr} (°C)	Ventilator
Dry	< 274	n/a	Off
Frost	274 – 284	≤ 0	On
Dew	274 – 340	> 0	On
Rain	≥ 340	> 0	Off
Snow	≥ 284	≤ 0	Off

Achieving level installation of the CNR4 on the fold-over tower was challenging because the instrument needs to be installed while the tower was folded down. The initial method of installation resulted in CNR4s that were not reliably leveled due to sagging of the round tube used to extend the CNR4 off the tower; and roll could not be effectively controlled. An improved net radiometer mount was designed and installed in Spring 2018 (Figure 2.4a). The new mount replaced the round tube stock with square shaped tubing to reduce potential for roll. To eliminate sag and compensate for errors in tower alignment, a support brace and turnbuckle were added. During installation with the tower in the vertical orientation, a tiltmeter mounted on the top of the CNR4 allowed technicians to monitor the sag and to correct for it by adjusting the turnbuckle.

2.2.2. Eddy Covariance Fluxes

The turbulent fluxes of momentum, heat, moisture, and CO_2 were measured using a closed path eddy covariance system (CPEC200, Campbell Scientific, Inc) mounted at 9 m agl

(Figure 2.5b). The CPEC200 includes an enclosed infrared gas analyzer (EC155, Figure 2.5a) to measure CO_2 and H_2O mixing ratios, a 3D sonic anemometer (CSAT3A), a diaphragm pump, and a valve module (Table 2.4). The CSAT3A, included in Figure 2.5a, uses ultrasonic pulses between three pairs of non-orthogonal transducers to measure high frequency wind velocity in three dimensions (*u*, *v*, and *w*). The speed of sound, which is related to "sonic" air temperature (T_s), is also measured. Dry air temperature can be calculated from sonic temperature and in situ water vapor measurements for sensible heat flux computations (Schotanus et al. 1983).

Table 2.4. NYSM flux instrument specifications

Measurement	Instrument	Units	Accuracy	Resolution	Sampling interval
Shortwave radiation Longwave radiation	Kipp & Zonen CNR4	Wm^{-2} Wm^{-2}	< 5% [1] <10% [1]	- -	1 s
CO2 molar concentration H2O molar concentration	Campbell Scientific EC155	µmol·mol[1] mmol·mol^{-1}	±1% [2] ±2% [2]	0.15 0.006	0.1 s
U axis wind velocity V axis wind velocity W axis wind velocity Air temperature (sonic)	Campbell Scientific CSAT3A	ms^{-1} ms^{-1} ms^{-1} °C	±0.08 ±0.08 ±0.04 -	0.01 0.01 0.005 0.025	0.1 s
Soil heat flux (x4)	Hukseflux HFP01	Wm^{-2}	-	-	1 s
Leaf wetness	Decagon dielectric Leaf Wetness Sensor	mV	no standard	-	1 s

[1] reflects maximum achievable accuracy under ideal conditions with frequent calibrations
[2] ±15 mm from 0 to 300 mm; ±15 % from 300 to 600 mm

The closed path IRGA design was chosen over an open-path design for two reasons: 1) the closed path sensor can be automatically calibrated on a regular basis (e.g., daily), enabling more accurate measurements of CO_2 and H_2O; and 2) the closed path sensor is less susceptible to errors caused by rain, dust, and dew deposition on the source and detector windows of the sample cell (Novick et al. 2013). Further, the EC155 features a novel "vortex intake" that facilitates removal of relatively heavy particles and water droplets from the air stream before it

reaches the sample cell (Figure 2.5a) (Burgon et al. 2015). The relatively clean air is then drawn into the EC155 sample cell at 8 LPM by the CPEC200's diaphragm pump.

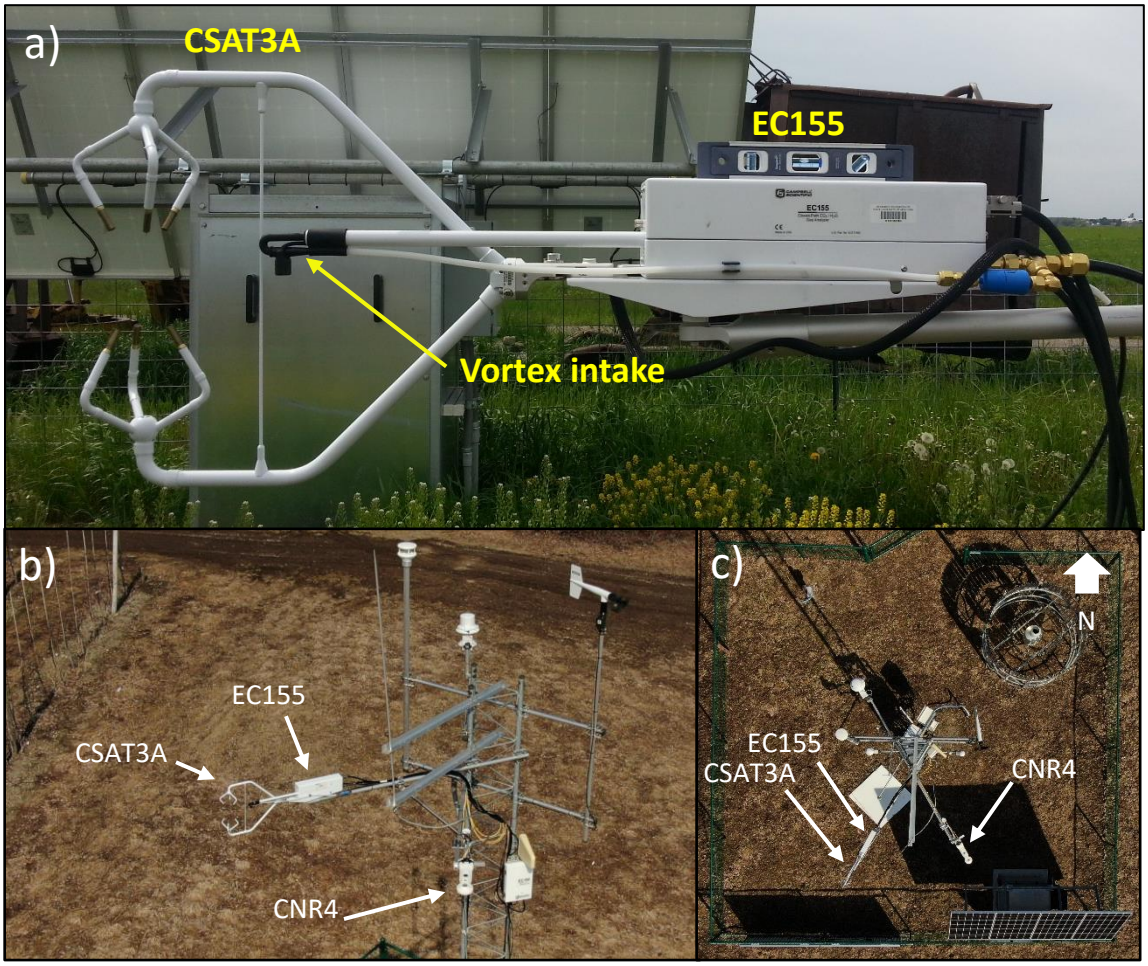

Figure 2.5. (a) EC155 gas analyzer with a CSAT3A sonic anemometer. The black end of the EC155 intake tube is a Vortex filter that removes particles from the sample air before reaching the gas analyzer's sample cell; (b) mounting of the EC155, CSAT3A, and CNR4 at 9 m agl on Rohn 25 tower (side view); (c) top-down view of VOOR NYSM site with EC155, CSAT3A, and CNR4 labeled. Photos courtesy of NYSM technician Nicholas Farruggio.

Occasional calibrations of the EC155 are recommended to maintain accuracy of the CO_2 and H_2O concentration measurements (Campbell Scientific Inc. 2016). IRGAs are prone to drift over time due to their sensitivity to ambient temperature and exposure to the elements (Campbell Scientific Inc. 2016). The EC155's CO_2 zero and span are automatically checked once daily using two reference gas concentrations stored in cylinders at each flux site.

The reference gasses are procured from a local gas supplier with targeted concentrations of 0 ppm and 420 ppm CO_2 mixed with air. The NYSM found that these concentrations can vary ±3 ppm of their targeted value. To achieve greater certainty in the reference gas concentrations, the cylinders are checked using a Picarro G4301 cavity ring-down spectrometer (CRDS) that was calibrated using two high quality National Oceanographic and Atmosphere Administration (NOAA) standard gasses and a known zero gas. Once the cylinders were tested by the CRDS, the concentrations become known to ±0.5 ppm accuracy.

When an automatic calibration check is activated, the CPEC200 valve module automatically switches between the two reference gasses to send a known concentration of CO_2 to the EC155. Gas flows to the EC155 at 1 LPM through a 6.4 mm diameter Synflex (Dekabon) tube. The steps in the calibration are noted on the time series of CO_2 mixing ratio in Figure 2.6: (a) At the start of the automatic calibration sequence, the sample pump is disabled. (b) After 10 seconds, zero gas from the prior calibration purges from the tube as CO_2 span gas (~420 ppm CO_2) begins to flow to the EC155. After a 300 second equilibrium period, the mixing ratio of CO_2 is checked against the reference. (c) Zero gas is then sent to the EC155 for 320 seconds, during which time, the mixing ratios of CO_2 and H_2O are checked for zero drift. (d) Once the offsets are archived, the system returns to normal operation. H_2O span calibrations are performed

in the field bi-annually using a LI-610 (LI-COR) portable dew point generator. For H_2O spans, the equilibrium time is 900 seconds.

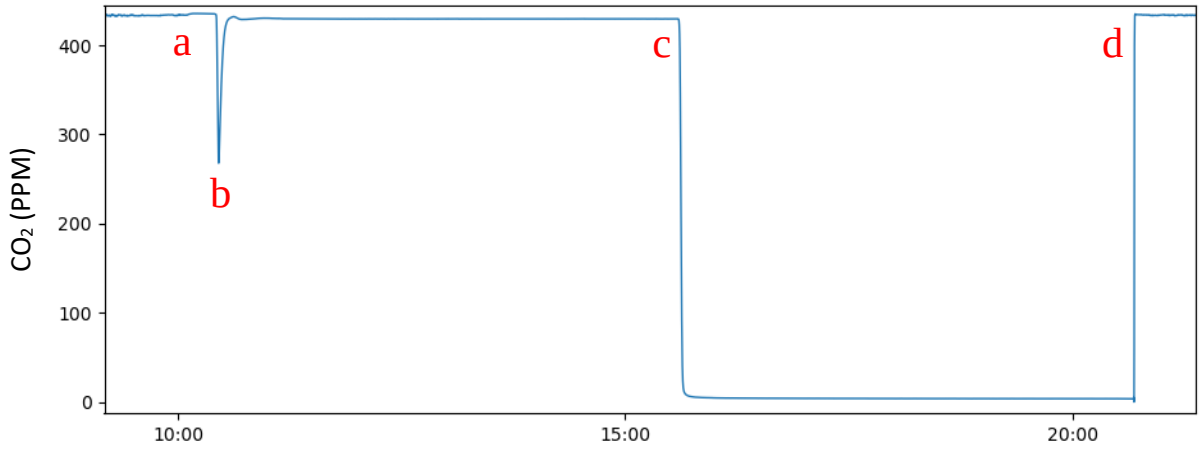

Figure 2.6. CO_2 mixing ratio measured during an automatic zero and span check.

Once the reference gas cylinders were installed during Spring 2018, automatic calibration checks were performed at 00z every day. Beginning in November 2018, the calibration check time was changed to 0510z. Automatic calibration checks were not performed December 2018 – February 2019, except at BKLN, QUEE, and STAT where full calibrations were performed.

2.2.3. Soil Heat Flux Plates

Four soil heat flux plates (HFP01, Hukseflux) were buried at a depth of 6 cm at the corners of a 1 × 1 m square located within the fenced in area of the NYSM site. The plates contain a passive thermopile that senses the temperature differential between its upper and lower surface (Figure 2.7b). The temperature differential is proportional to soil heat flux (Wm^{-2}). The output from the four flux plates are averaged to obtain a more spatially representative measure of soil heat flux at the measurement depth ($\overline{G_m}$). Soil heat flux at the measurement depth is,

$$\overline{G_m} = \frac{\left(mV_{p1}*\frac{1000}{C_{p1}}\right)+\left(mV_{p2}*\frac{1000}{C_{p2}}\right)+\left(mV_{p3}*\frac{1000}{C_{p3}}\right)+\left(mV_{p4}*\frac{1000}{C_{p4}}\right)}{4}, \quad (14)$$

where C_{px} is the factory calibration coefficient for each soil heat flux plate and mV_{px} is the raw output voltage of the sensor. The subscript x is the identifier for the individual heat flux plates.

The soil heat flux plates were inserted into the soil profile, as shown in Figure 2.7a. A shovel was used to vertically cut into the ground enabling the soil to be removed from the hole as an in-tact soil core. A knife was then used to gently remove a narrow slot of soil at a depth of 6 cm. The plate was then inserted into the slot prior to the soil core being returned to the hole. A narrow trench was dug to route the soil heat flux cables to conduit used for NYSM soil temperature and moisture probes (Figure 2.7c). Each plate's location was mapped using a grid system where the northwest corner of the NYSM standard site is the origin (0,0). Photos of the soil profile were taken upon each installation for future reference.

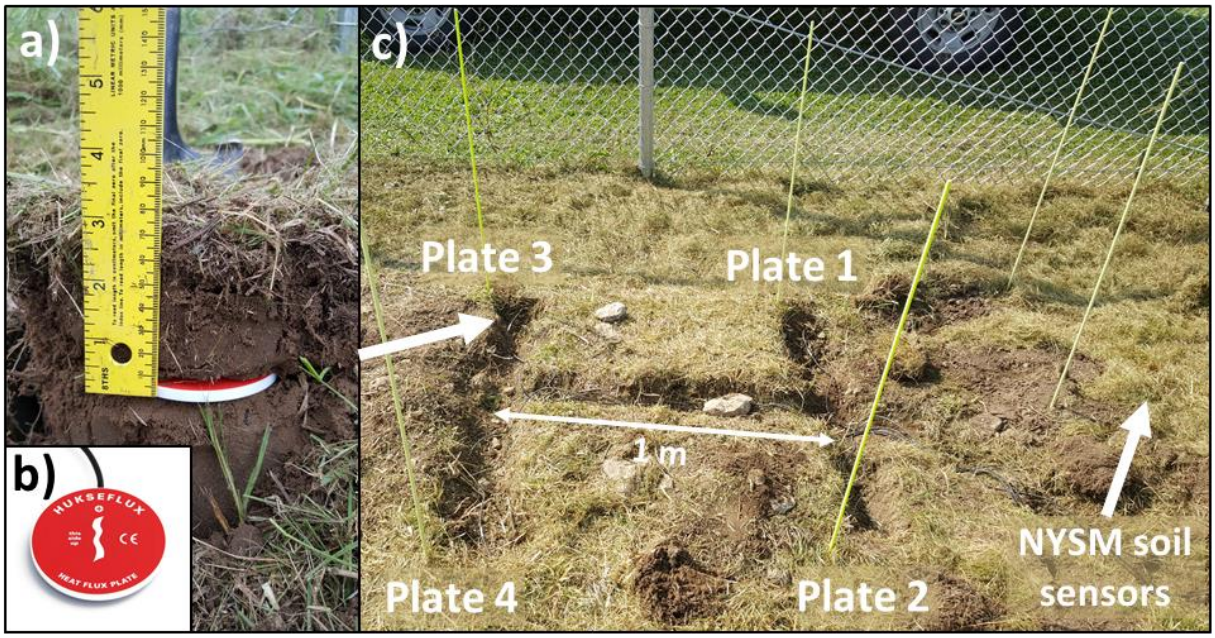

Figure 2.7: (a) An HFP01 soil heat flux plate inserted into the soil profile at a depth of 6 cm. (b) Image of top face of a Hukseflux HFP01. (c) Installation of the four soil heat flux plates at the corners of a 1x1 m square. Soil temperature and moisture sensors are buried about 1 m to the right (north) of the soil heat flux plates.

The configuration of the NYC flux sites is slightly different. BKLN, QUEE, and STAT use rooftop-mounted, fixed (not fold-over), towers and do not include soil heat flux plates. At BKLN, QUEE, and STAT, the net radiometer faces toward 141.5º, 247.5º, and 180º respectively. The IRGA and sonic anemometer face toward 201.5º, 307.5º, and 240º respectively. The tower at Southold (SOUT) was stand-alone due to a need for its higher wind load rating.

2.3 Data Acquisition

Figure 2.8 depicts the flow of data from the instruments to the preliminary quality-controlled fluxes. A datalogger (CR6, Campbell Scientific, Inc) is used to monitor the flux instruments, sample data, compute preliminary fluxes, and facilitate transmission of data to the NYSM servers. The gas analyzer and sonic anemometer are sampled at 10 Hz, and the net radiometer and four soil heat flux plates are sampled at 1 Hz. A CRBasic program (EasyFlux DL, Campbell Scientific Inc.) uses the 10 Hz data to compute preliminary fluxes every 30 minutes. Preliminary fluxes are transmitted to the NYSM server every 30 minutes using the cellular (cell) network. Raw data are transmitted every 5 minutes alongside meteorology data from the standard site. A 16 gigabyte (GB) micro SD card in the datalogger provides backup data storage in the event of a communications failure at the site. Flux data were archived and then quality controlled prior to the analysis in this research.

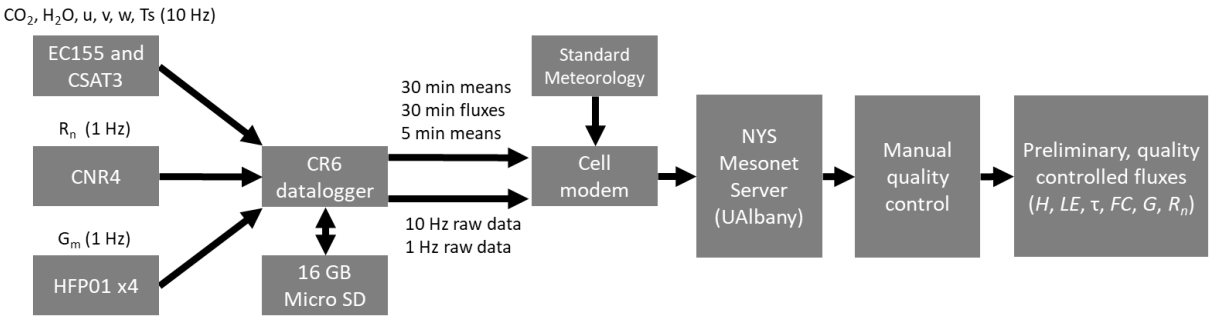

Figure 2.8. Flow of data at flux sites

2.4 Power Management

Figure 2.9 is a schematic of the power management configuration of the CPEC200 enclosure, which was modified to facilitate the NYSM power system. The flux system uses a smart regulator (CH200, CSI) coupled with a 7ah backup battery to regulate the incoming voltage from the NYSM solar system to 12 V. The CH200 outputs load and voltage information so that power consumption of the flux system can be monitored. Three solid state relays act to switch power to (1) the EC100 electronics box for the sonic anemometer and IRGA; (2) the net radiometer heater; and (3) the net radiometer fan. The relays are switched using analog signals from the datalogger. A multiplexer (CDM-A116, CSI) is used to sample the net radiometer and the soil heat flux plates, given the lack of available channels on the datalogger.

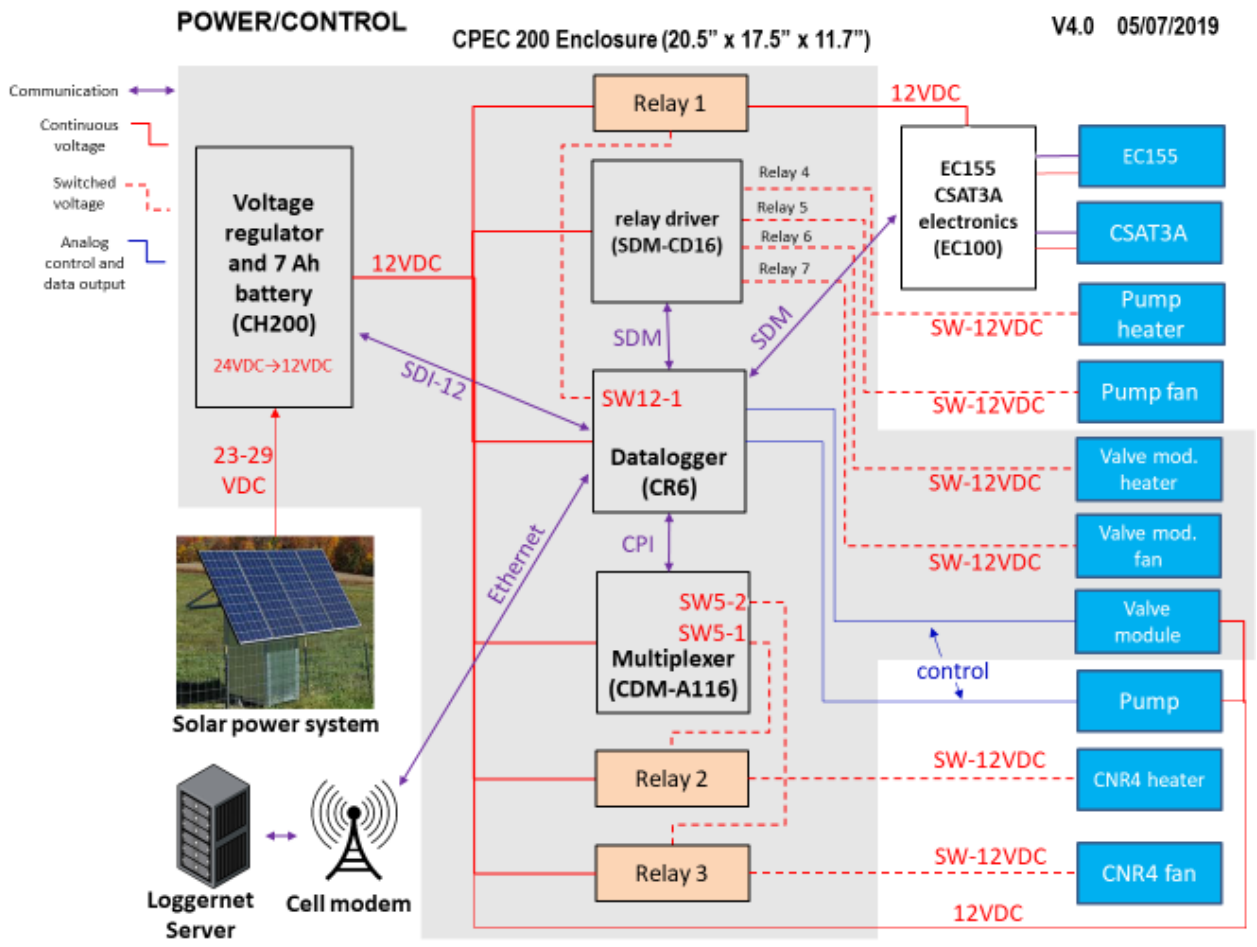

Figure 2.9. Schematic of power and communication hardware for the modified NYSM CPEC200 flux system. Power is controlled to flux system components, represented by the blue squares. All components of the system that are installed inside the CPEC200 enclosure are in the grey shaded area.

Though the standard site's power system is well under its capacity for most of the year, snow buildup on solar panels and reduced daylight hours during the winter occasionally limit the ability of the battery bank to fully recharge during the day. In addition, colder air temperatures require that some heating be performed to keep instruments within their operating temperature (note Figure 2.10). If energy needs to be conserved to keep the standard site operating, the flux system power consumption is reduced. In winter 2017/18 (Nov 1, 2017 – Mar 2018), the flux system power use was reduced by 10 W by turning off the IRGA and sonic anemometer. Since the net radiometer and soil heat flux plates required negligible power, they remained on during this period.

Table 2.5. Flux system power budget (numbers in Watts at 12 VDC)

	Flux system running modes			
Component	**Low**	**Standby**	**Full**	**Operating conditions**
Datalogger + peripherals	3.7	3.7	3.7	
Soil heat flux plates	0	0	0	
CNR4	0	0	0	
CNR4 Fan	off	off	5 W	if dew/frost is detected on LWS
CNR4 Heater	off	off	10 W	if dew/frost is detected on LWS
Sonic anemometer	off	3	3	
EC155	off	off	3	
Pump	off	off	4.3	
Pump fan	off	off	0.7 W	If pump temperature ≥ 45°C
Pump heater	off	off	8 W	If pump temperature ≤ 2°C
Valve module fan	off	off	0.7 W	prior to calibration if valve temperature ≥ 50°C
Valve module heater	off	off	8 W	prior to calibration if valve temperature ≤ 2°C
Power draw (-8 to 8 °C)	**3.7 W**	**6.7 W**	**14-37 W**	

The flux system power management was improved for the following winter (2018/19). The improved power management protocol has three power modes as summarized in Table 2.5: full power mode (all flux sensors operational, ~14 W); standby mode (~6.7 W) for data collection from the net radiometer, soil heat flux plates, and sonic anemometer; and low power mode (~3.7 W) when only the datalogger, soil heat flux plates, and net radiometer are active.

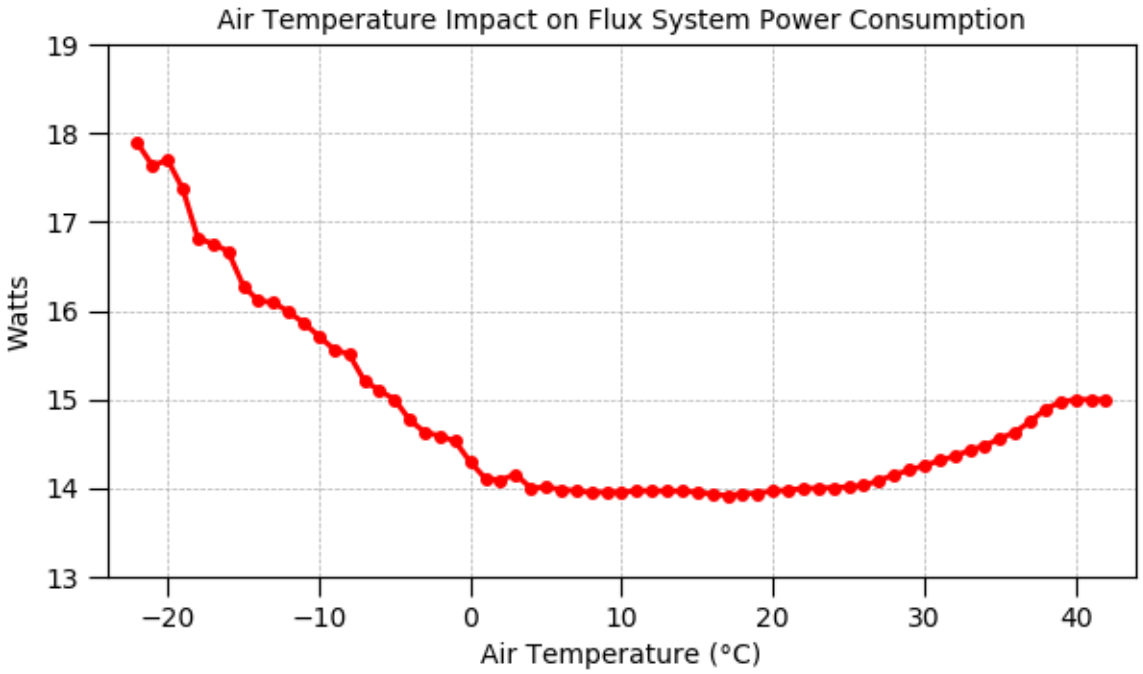

Figure 2.10. Power consumption of the NYSM flux system vs. air temperature as measured within the CPEC200 enclosure throughout the year of 2018. These data are averaged among all flux sites in cases where the systems were running at steady state in full power mode. Only periods without net radiometer heating and ventilating were considered.

The flux system's power management decisions are guided by input voltage as measured by the smart regulator. On a typical sunny day, the voltage output of the NYSM battery bank resembles the time series in Figure 2.11. The voltage of the battery bank increases during the day as it is charged by the solar panels and decreases when it is discharged at night. The down-step in voltage, that occurs just after hour 12, indicates that the battery bank is fully charged. On days where this plateau is not apparent, the batteries do not reach their full capacity. The inability of

the batteries to fully charge is typically caused by a succession of cloudy days or snow accumulation on the solar panels.

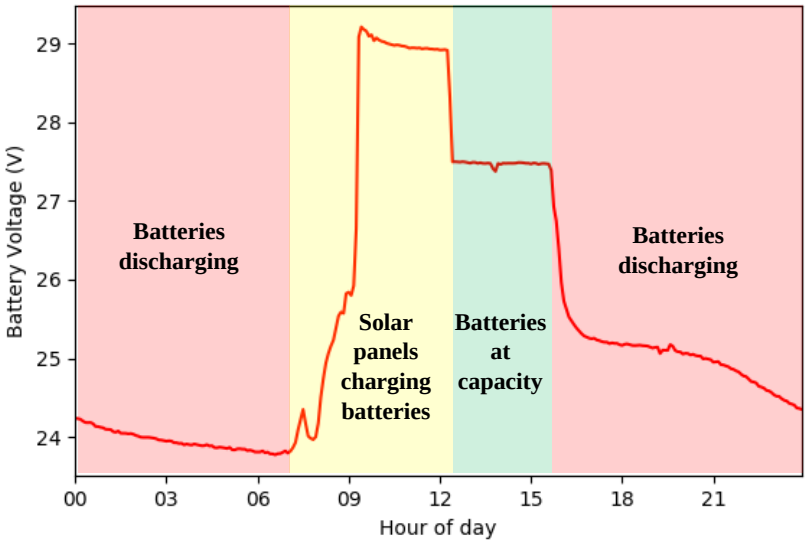

Figure 2.11. Mesonet battery voltage as measured by flux system's charge regulator. Note the plateaus in battery voltage occur when the batteries are charging and when batteries reach full capacity.

Summer and winter power management regimes were implemented in the datalogger program to automatically manage power consumption. On the summer schedule, the flux system switches between low power and full power mode at a threshold of 23.2 V incoming from the battery bank. The summer schedule is operated between March 1 and October 31. While running the winter schedule, the voltage thresholds are higher due to the increased likelihood that there will be days in which power is limited. If incoming voltage is less than 24.5 V, the flux system will switch to low power mode. If incoming voltage is less than 27 V or greater than 24.5 V, the system runs in standby mode. In cases where the voltage plateau is reached, the system will run in full power mode. The net radiometer's heater and ventilator always remain disabled when the system is on its winter schedule.

2.5 Flux Calculations

2.5.1. Turbulent Fluxes

The data acquisition program running on the CR6 datalogger (EasyFlux DL, CSI) computes preliminary fluxes every 30 minutes. The calculation of fluxes includes the steps and corrections outlined in Table 2.6.

The first correction employed by the datalogger program is the omission of suspect data. Raw 10 Hz data were omitted from the flux calculation if any diagnostic flag for the IRGA or sonic anemometer were tripped during its collection. Diagnostic flags can be tripped by several conditions, including, but not limited to, low power input, obstructions in the path of the sonic anemometer transducers, water ingest into the IRGA sample cell, or hardware faults. Data points were also omitted if they fell outside the calibrated output range for the instrument or if they were characterized as spikes. Spikes are defined as non-physical transient fluctuations in data caused by instrument error or electronic noise (Starkenburg et al. 2016; Brock 1986).

A double coordinate rotation is then performed to orient the sonic anemometer's coordinates into the mean wind flow. A spatial separation correction considers the wind direction dependent time lag in the measurement of gas relative to the measurement of wind. High and low frequency corrections account for losses in fluxes due to the dampening effects of the gas intake tube and insufficient length of the flux averaging interval. The sensor separation correction addresses the time lag for gas to flow from the IRGA's inlet to the sample cell. After this correction, the wind and gas measurements are effectively matched in time. The sonic temperature correction converts the sonic temperature to air temperature using H_2O mixing ratio measurements from the IRGA. Finally, CO_2 and H_2O fluctuations are corrected for density fluctuations.

Table 2.6. Corrections applied to compute fluxes of τ, H, LE, and FC

Correction/process	Description	Reference(s)
Double coordinate rotation into natural coordinate frame	Rotate sonic coordinates to where the u-axis is parallel to the mean wind vector, v-axis is perpendicular to the mean wind vector, and mean vertical wind velocity is zero over the 30-minute averaging period.	Tanner and Thurtell 1969
Spatial separation correction	Corrects for wind direction dependent time lag in wind and gas measurements due to spatial distance between the sonic anemometer measurement volume and that of the gas analyzer.	Horst and Lenschow 2009; Foken et al. 2012a
High frequency corrections	Accounts for loss due to inadequate sampling of high frequency fluctuations (e.g. due to sensor separation or damping in tubing).	Horst and Lenschow 2009; Foken et al. 2012a; Moore 1986; Moncrieff et al. 1997; Dijk 2002; Montgomery 1947; Shapland et al. 2014; Geankoplis 1993
Low frequency correction	Accounts for loss due to fluctuations with frequency too low to measure fully during the averaging period	Kaimal et al. 1989; Massman 2000; Moore 1986; Dijk 2002; Moncrieff et al. 1997
Sensor separation	Account for the physical separation between the sonic anemometer measurement volume and sample cell of gas analyzer	Horst and Lenschow 2009; Foken et al. 2012
Sonic temperature correction	Conversion of sonic temperature (T_s) to air temperature T	Schotanus et al. 1983; Dijk 2003
WPL correction	Accounts for the impact of air density fluctuations on CO_2 and H_2O fluctuations measured by the IRGA	Webb et al. 1980

2.5.2. Soil Heat Flux

Surface heat flux (G) is a function of $\overline{G_m}$ and the heat storage (S) in the layer of soil above the soil heat flux plates. Surface heat flux is given by,

$$G = S + \overline{G_m}. \quad (15)$$

Heat storage can be calculated by,

$$S = \rho_s c_s h \frac{\partial \bar{T}}{\partial t}\,, \tag{16}$$

where h is the depth of the soil heat flux plates in meters and $\frac{\partial \bar{T}}{\partial t}$ is the time rate of change of the average layer temperature above the plates (Campbell 1977). The volumetric heat capacity of soil is given by,

$$\rho_s c_s = \phi_m \rho_m c_m + \theta \rho_w c_w + \phi_o \rho_o c_o\,, \tag{17}$$

where ϕ_m is the volume fraction of minerals, θ is the volume fraction of water, and ϕ_o is the volume fraction of organic matter (Campbell and Norman 1998). Subscripts on density (ρ) and specific heat (c) denote which material they correspond to: soil (s), minerals (m), water (w), and organic matter (o).

Several assumptions about the soil composition must be made to estimate $\rho_s c_s$. These assumptions are outlined in Table 2.7. The volume fraction of water is measured by a Stevens Hydra Probe II buried 1-meter north of the heat flux plates, at a depth of 5 cm. All flux sites have varying types of loamy soil. The volume fraction of minerals and organic material was assumed to be 45% and 5% respectively. The remaining volume of material in the soil is partitioned between water and air.

Table 2.7: Variable assumptions and descriptions for Equation 17

Variable	Value	Units	Description
ϕ_m	0.45	$m^3\ m^{-3}$	Typical mineral fraction in loamy soil
ρ_m	2650	$kg\ m^{-3}$	From Campbell and Norman (1998), Table 8.2
c_m	870.0	$J\ kg^{-1}K^{-1}$	From Campbell and Norman (1998), Table 8.2
θ	Measured	$m^3\ m^{-3}$	By a Stevens Hydra Probe II buried near heat flux plates
ρ_w	999.7	$kg\ m^{-3}$	Liquid water at 10°C
c_w	4192	$J\ kg^{-1}K^{-1}$	Liquid water at 10°C
ϕ_o	0.05	$m^3\ m^{-3}$	Typical organic matter fraction in loamy soil
ρ_o	1300	$kg\ m^{-3}$	From Campbell and Norman (1998), Table 8.2
c_o	1920	$J\ kg^{-1}K^{-1}$	From Campbell and Norman (1998), Table 8.2

The average temperature ($\bar{T}$) of the layer of soil above the soil heat flux plates must be estimated using an empirical model of soil temperature (T) integrated from the surface ($z = 0$) to the depth of the soil heat flux plates ($z = 0.06$). The model is given by:

$$T(z,t) = T_{ave} + A(0)\exp\left(-\frac{z}{D}\right)\sin\left[\omega(t - t_o) - \frac{z}{D}\right], \quad (18)$$

where T_{ave} is the average surface temperature over the last 24 hour period, $A(0)$ is the amplitude of the 24 hour soil temperature fluctuation, D is the damping depth, ω is the angular frequency of the soil temperature oscillation, and t_o converts t from UTC to local time (Campbell and Norman 1998). The 24 hour average surface temperature (T_{ave}) and A(0) are calculated using radiometrically measured surface temperature data ($T_{surface}$). The surface temperature is given in units of °C by,

$$T_{surface} = \left(\frac{LW\uparrow}{\varepsilon\sigma}\right)^{\frac{1}{4}} - 273.15. \quad (19)$$

where ε is the emissivity and σ is the Stephen-Boltzmann constant. The emissivity is assumed to be 0.98, which is an appropriate assumption for grassy surfaces (Humes et al. 1994). Damping depth (D) is calculated by;

$$D = \sqrt{\frac{2K}{\omega}}, \quad (20)$$

where K is the thermal diffusivity of the soil and ω is the angular frequency of a diurnal cycle (7.3×10^{-5} s^{-1}) (Campbell and Norman 1998). K can be calculated using Equation 21 from Campbell and Norman (1998);

$$K = \frac{k}{\rho_s c_s}, \quad (21)$$

where k is thermal conductivity of the soil, assumed to be constant with depth. Thermal conductivity of the soil can be computed using the volume fraction of its components, as is discussed in Campbell and Norman (1998). The value for k, used in the computation of K, follows the curve for loam soil as shown in Figure 8.3 of Campbell and Norman (1998).

2.6 Quality Control

Data from the net radiometer, soil heat flux plates, and leaf wetness sensor were quality controlled using range and step tests (Shafer et al. 2000). Data points that failed either one of the tests were excluded from the results presented in this thesis. The range test eliminates data points that are not physically possible or are outside of the instrument's calibrated measurement range. The range of acceptable values for the measurements is shown Table 2.8. The step test removes data points that spike anomalously between samples. These spikes are often the result of instrumentation error. The range for acceptable step sizes were determined by reviewing time-series of steps over the course of one summer and one winter for each measurement. The step size in Table 2.8 was selected to accommodate realistic step sizes observed, which were determined qualitatively.

Table 2.8. Data filtering thresholds for quality control

Measurement	Units	Range	± Step (1 Hz data)
SW↓	Wm^{-2}	-15 – 1500	150
SW↑	Wm^{-2}	-15 – 1000	100
LW↓	Wm^{-2}	100 – 500	15
LW↑	Wm^{-2}	150 – 700	2
T_{nr}	°C	-30 – 60	0.2
G_m	Wm^{-2}	-150 – 200	0.2
CO_2	$\mu mol \cdot mol^{1}$	340 – 1000	500
H_2O	$mmol \cdot mol^{-1}$	0.1 – 60	5
u, v, w	ms^{-1}	-65 – 65	15
T_s	°C	-50 – 60	5

On calm days with solar irradiance exceeding 1000 Wm^{-2}, the LW↓ measurement can be biased positive up to 10 wm^{-2} because of dome heating (Kipp & Zonen B.V. 2014). Radiational cooling of the pyranometer domes can result in negative biases in SW measurements at night, up to 15 Wm^{-2} (Kipp & Zonen B.V. 2014). Shortwave radiation data between -15 Wm^{-2} and 0 Wm^{-2} were adjusted to 0 Wm^{-2} for computations in this thesis. CO_2 and H_2O data were removed if they were obtained during a calibration. Data were also excluded from the analyses if they were suspect due to instrumentation errors.

2.7 Maintenance

NYSM technicians visit every standard and enhanced site at least twice a year; during the fall for "fall pass" and during the spring for "spring pass." A sample fall pass checklist is included in Appendix B. During site visits, all flux instruments and gas tanks are inspected and cleaned according to manufacturer recommendations, desiccant and filters are replaced, and a field calibration of the IRGA is performed. On an annual basis, scrubbing chemicals consisting of magnesium perchlorate and ascarite II are replaced in the IRGA's optical cavities. Over time, when the chemicals become saturated, drift in the H_2O and CO_2 concentration measurements becomes increasingly visible. When the chemicals are replaced, CSI recommends waiting at least 24 hours before performing a recommended calibration of CO_2 and H_2O. This has posed a logistical challenge since flux sites distant from the NYSM office are not easily re-visited within 48 hours for calibration. Effort is underway to address this logistical challenge and to better determine the frequency required for chemical replacement.

Re-calibration of the net radiometers is recommended every two years. During factory calibrations, the two pyranometers on the net radiometer are individually measured against a primary standard pyranometer with World Radiometric Reference traceability (Fröhlich 1991).

The pyrgeometers are calibrated to a reference traceable to the World Reference at the World Meteorological Organization in Davos, Switzerland (Kipp & Zonen B.V. 2014). The NYSM is working to develop a strategy to calibrate the net radiometers in such a way that measurement downtime is minimized.

CHAPTER 3:
Flux Network Performance

3.1 Data Recovery

The data recovery rate was calculated from the quality-controlled 1 Hz data as,

$$recovery\ rate = \left(\frac{number\ of\ good\ records}{number\ of\ potential\ records}\right) \times 100. \quad (22)$$

The number of potential records per 3-month season was 7,948,800. Table 3.1 shows data recovery rates for all flux sites between the period of March 1, 2018 and February 28, 2019. The table is separated into four sections corresponding to the net radiometer, soil heat flux plates, sonic anemometer, and IRGA. The net radiometer has five measurements with individual recovery rates ($SW\downarrow$, $SW\uparrow$, $LW\downarrow$, $LW\uparrow$, and T_{nr}). Since each measurement is essential for the calculation of R_n, the lowest recovery rate was selected to represent the net radiometer. The same practice was adopted to determine the recovery rate for the soil heat flux plates and the sonic anemometer (u, v, w, and T_s) and IRGA (CO_2 and H_2O mixing ratios).

The average data recovery rate was 87.8% for all instruments. The highest rates occurred during the summer (JJA) when there was ample power from the solar panels. During JJA 2018, the average recovery rates for the net radiometers, soil heat flux plates, IRGAs, and sonic anemometers were 99.9%, 99.9%, 93.7%, and 99.4% respectively. Recovery rates for the IRGA and sonic anemometer were about 13% lower during the transition seasons (MAM and SON) due to the need for occasional power saving measures, particularly during late November and early March. The net radiometer and soil heat flux plates were unaffected by seasonal power saving measures because they are passive sensors.

Table 3.1. Data recovery rates for the period of March 1, 2018 – February 28, 2019.

	Net Radiometer (R_n)					Soil Heat Flux Plates (G)					Sonic Anemometer (u, v, w, T_s)					Gas Analyzer (CO_2, H_2O)				
ID	MAM	JJA	SON	DJF	Average	MAM	JJA	SON	DJF	Average	MAM	JJA	SON	DJF	Average	MAM	JJA	SON	DJF	Average
BELL	99.9	100.0	99.8	100.0	99.9	99.9	100.0	99.9	100.0	100.0	83	99.4	87.0	48.2	79.4	83.7	99.7	81.5	25.3	72.6
BKLN	99.9	100.0	99.9	100.0	100.0	NYC - No Plates					98	99.7	98.4	96.5	98.2	99.1	99.8	99.8	97.5	99.1
BURT	99.9	99.9	99.6	100.0	99.9	99.9	100.0	99.9	100.0	100.0	81.2	99.8	95.4	52.3	82.2	70.7	99.6	95.4	19.8	71.4
CHAZ	99.9	99.8	99.9	99.8	99.9	99.9	99.8	99.9	99.8	99.9	84.7	99.5	86.4	53.9	81.1	82.4	99.5	82.2	25.6	72.4
FRED	99.9	99.9	98.9	99.9	99.7	100.0	99.9	98.9	99.9	99.7	85.7	99.4	81.7	37.8	76.2	83	99.6	77.9	17.5	69.5
ONTA	99.9	100.0	94.6	84.3	94.7	99.9	100.0	99.7	100.0	99.9	82.2	99.8	95.7	56.4	83.5	81	99.8	95.1	19.7	73.9
OWEG	90.6	99.8	55.5	14.3	65.1	99.9	100.0	99.9	99.9	99.9	86.8	99.8	95.7	57.9	85.1	87.4	99.7	95.4	25.2	76.9
PENN	100	100.0	100.0	99.5	99.9	100.0	100.0	100.0	99.5	99.9	79.2	99.1	82.5	39.6	75.1	75.3	99.0	77.7	18.3	67.6
QUEE	99.9	100.0	100.0	99.9	100.0	NYC - No Plates					97.4	99.8	99.1	95.3	97.9	98.6	99.8	99.7	96.5	98.7
REDF	99.9	100.0	98.4	100.0	99.6	99.9	100.0	99.2	100.0	99.8	83.4	99.5	84.8	48.7	79.1	82	99.8	81.2	25.4	72.1
REDH	100	100.0	99.9	100.0	100.0	100.0	100.0	99.9	100.0	100.0	53.8	99.8	94.1	61.3	77.3	54	99.7	95.8	28.7	69.6
SCHU	99.8	100.0	99.8	100.0	99.9	99.8	100.0	99.9	100.0	99.9	91.8	99.5	92.8	62.6	86.7	84.9	99.8	94.6	26.5	76.5
SOUT	96.4	99.5	99.9	100.0	99.0	96.4	99.5	99.9	100.0	99.0	77.3	99.4	98.2	52.5	81.9	87.1	95.5	99.7	30.6	78.2
STAT	99.9	100.0	99.3	99.9	99.8	NYC - No Plates					98.2	99.8	97.9	98.4	98.6	99.2	99.8	99.4	97.8	99.1
VOOR	32.1	100.0	95.4	100.0	81.9	60.9	100.0	95.4	100.0	89.1	58	99.1	89.3	52.8	74.8	59.3	100.0	89.6	24.9	68.5
WARS	99.9	99.9	100.0	99.9	99.9	99.9	99.9	100.0	99.9	99.9	66.5	0.0	0.0	28.0	23.6	79	99.7	86.3	20.9	71.5
WHIT	95.3	99.9	99.5	98.0	98.2	95.3	99.9	99.8	98.0	98.3	53.9	99.6	93.6	36.4	70.9	54.7	99.7	94.2	16.9	66.4
Average	94.9	99.9	96.5	93.9	96.3	96.6	99.9	99.5	99.8	98.9	80.1	93.7	86.6	57.6	79.5	80.1	99.4	90.9	36.3	76.7

During the winter (DJF), the IRGA and sonic anemometer were powered down at night to reduce the energy load on the battery bank. These power-saving measures are reflected in the IRGA and sonic anemometer winter recovery rates of 36.3% and 57.6%, respectively. The sonic anemometer recovery rate was higher than the IRGA due to its lower power requirement. The year-round average sonic anemometer and gas analyzer recovery rate was 98.6% at the NYC sites and 73.7% for all other sites. The NYC sites were operated continuously year-round because they are not reliant on solar power.

Here, the causes of site-specific instrumentation data gaps are listed:

(1) Random and sporadic data "freeze-ups" were experienced at several sites during the first four months of operation (up to late-June 2017). The issue was resolved in coordination with CSI by updating the datalogger operating system.

(2) At BURT, mice chewed through all four soil heat flux plate cables in early September 2017. The plates were replaced on November 8, 2017.

(3) The IRGA and sonic anemometer electronics box at BKLN was replaced with the box from REDH due to its need for factory repair. This affected IRGA and sonic anemometer data between September 8, 2017 and April 11, 2018 at REDH and between August 3, 2017 and September 1, 2017 at BKLN.

(4) A network-wide data outage occurred between December 22, 2017 and January 1, 2017. All net radiometer and soil heat flux data were lost during this period.

(5) At OWEG, the net radiometer developed a fault in October 2017 that caused suspect LW↓ and SW↑ measurements. The issue was resolved for most of summer 2018 but resurfaced again during fall 2018, prompting the instrument's removal from the field

for repair on October 24, 2018. It was re-installed on February 14, 2019, but the NYSM continues to troubleshoot the issue.

(6) The sonic anemometer at WARS experienced a transducer failure that affected data between May 20, 2018 and January 15, 2019.

(7) Sporadic net radiometer outages occurred at ONTA between November 2018 and mid-January 2019 due to a loose wire.

(8) At VOOR, the entire flux system was temporarily removed from the field between January 11, 2018 and April 5, 2018 to develop and test the IRGA calibration procedure. The net radiometer was not re-installed until May 18, 2018, as it was being used to develop an improved levelling mount.

(9) One defective heat flux plate was replaced at WHIT (Plate 1) on August 16, 2018. The lack of data from this plate did not affect the soil heat flux data recovery rate at WHIT because there were three other redundant plates.

3.2 Flux Quality Grading

A measure of quality for each 30-minute flux is calculated by the CSI software running on the datalogger (EasyFlux DL). "QC grades" reflect how well atmospheric conditions within flux averaging periods align with the assumptions on which the application of the EC method is based (Foken et al. 2012b; Campbell Scientific Inc. 2017). Three criteria are included in the determination of QC grades for *FC*, *H*, *LE*, and τ: non-stationarity (RN_{cov}), relative integral turbulence characteristics (ITC), and wind direction (Campbell Scientific Inc. 2017).

The non-stationarity parameter, RN_{cov}, reflects the degree to which the turbulent flow structure of the atmosphere is steady-state within each 30-minute flux averaging period. Non-

stationarity can be caused by micro and mesoscale phenomena such as wind direction shifts, gravity waves, or cloud passage. The non-stationarity parameter is calculated as a percent by,

$$RN_{cov} = 100 \times \left| \frac{\frac{1}{6}\sum_{i=1}^{6}(\overline{s'w'})_{ri} - (\overline{s'w'})_r}{(\overline{s'w'})_r} \right|, \quad (23)$$

where $\overline{s'w'}$ is the covariance *w* and some measured quantity (e.g. air temperature, CO_2 density, or water vapor mixing ratio) (Campbell Scientific Inc. 2017; Foken et al. 2012b). Six 5-minute covariances are computed within the flux averaging period and then are compared to the 30-minute covariance. According to Foken et al. (2006), an RN_{cov} value of 30% or less indicates that atmospheric conditions are sufficiently close to steady state.

The relative integral turbulence characteristics parameter, ITC, is the standard deviation of a scalar (e.g. u' and T') normalized by scaling variable (e.g. friction velocity [u_*] or scaling temperature [T_*])(Campbell Scientific Inc. 2017). Friction velocity and T_* are calculated by,

$$u_* = \sqrt[4]{(\overline{u'w'})^2 + (\overline{v'w'})^2}, \quad (24)$$

$$\text{and} \qquad T_* = -\frac{\overline{T'w'}}{u_*} \text{ (Kaimal and Finnigan 1994).} \quad (25)$$

The ITC can be measured using the variance of a scalar (α) or modelled for the scalar in conditions of fully developed turbulence. If turbulence is fully developed, the measured ITC ($ITC_{\alpha\_measured}$) should be the same as the modeled ITC (ITC_{α_model}). ITC_{α_model} is determined using stability;

$$ITC_{\alpha\_model} = \begin{cases} c_{\alpha 1} \ln \frac{z+f}{u_*} + c_{\alpha 2} & \frac{z}{L} > 0 \\ c_{\alpha 1} \left(\frac{z}{|L|}\right)^{c_{\alpha 2}} & \frac{z}{L} \leq 0 \end{cases} \quad (26)$$

where $c_{\alpha 1}$ and $c_{\alpha 2}$ are parameters dependent on stability and scalar (See Table F-2 in Campbell Scientific Inc. 2017).

The stability parameter is $\frac{z}{L}$, where z is the measurement height and L is the Obukhov length,

$$L = -\frac{u_*{}^3(\overline{T_s}+273.15)}{kg(\overline{w'T_s'})}, \tag{27}$$

where T_s is the sonic temperature, k is the Von Kármán constant (0.41), and g is the acceleration of gravity. The Coriolis parameter in Equation 25 is given by,

$$f = 2\Omega \sin \emptyset \tag{28}$$

where Ω is angular velocity of earth's rotation ($7.292 \times 10^{-5} \cdot s^{-1}$) and $\emptyset$ is the latitude.

The relative difference of measured and modeled ITC for a scalar of interest ($\alpha = u, v,$ or w) can be calculated by,

$$ITC_{\alpha} = 100 \times \frac{\left| ITC_{\alpha\_model} - \left(\frac{\sqrt{(\alpha'^2)_r}}{u_*} \right)_{\alpha\_measured} \right|}{ITC_{\alpha\_model}}. \tag{29}$$

The relative difference of measured and modeled ITC for air temperature (T) is given by:

$$ITC_{T} = 100 \times \frac{\left| ITC_{T\_model} - \left(\frac{\sqrt{(T'^2)_r}}{T_*} \right)_{T\_measured} \right|}{ITC_{T\_model}}, \tag{30}$$

where ITC_{T_model} is calculated by:

$$ITC_{T\_model} = c_{\alpha 1} \left(\frac{z}{|L|} \right)^{c_{\alpha 2}}. \tag{31}$$

To determine the ITC for scalars (ITC_{sw}), ITC_T and ITC_w are calculated. The maximum value of the two parameters is set to be ITC_{sw}, which is used to grade *FC*, *H*, and *LE*. To determine the ITC for τ, ITC_u and ITC_w are calculated separately. Whichever has the maximum value is assigned to ITC_{tau} which is used only to grade τ. Values of ITC_{sw} and ITC_{tau} that are closer to zero indicate better development of turbulence. An ITC value of less than 30% indicates that turbulence is sufficiently well developed (Foken et al. 2006).

Foken et al. (2012) recommends a scale of 1–3 to describe the degree to which wind flow is contaminated by the CSAT3A anemometer's design. Note that the IRGA and supporting arms of the CSAT3A exist at the same elevation as the sensing area (Figure 2.4a). Relative to the sonic anemometer, winds prevailing from 180° ± 10° are likely distorted due to blocking from the supporting arms and IRGA. Flux averaging periods with a wind direction between 170° and 190° are assigned a wind direction grade of 3. If the wind direction is between 151° and 169° or between 191° and 209°, the wind direction grade is assigned a 2. All other wind directions receive the best grade of 1. In a cardinal frame, the most contaminated wind direction at the flux sites is the northeast. This is due to the tower location relative to the sonic anemometer. The author suggests that a wind direction grade of 2 or 3 encompasses the potential for flow distortion caused by the tower. This needs to be verified specifically for NYSM towers.

The datalogger program (EasyFlux DL) outputs a single QC grade for τ, *H*, *LE*, and *FC* every 30 minutes. For a given overall QC grade, the values for RN_{cov} and ITC, will fall within the ranges noted in Table 3.2. Foken et al. (2006) suggests that overall QC grades between 1 and 3 are sufficient for robust research applications (e.g. development of parameterizations). A grade between 4 and 6 indicates that the data are appropriate for more general applications where

accuracy is less critical. Data with grades of 7 and 8 should avoided, except where they may be useful for filling gaps in the data record. Data with a grade of 9 should not be used.

Table 3.2. Ranges of RN_{cov}, ITC_{sw}, ITC_{tau}, and wind direction corresponding to overall QC grade. Values are summarized from Tables F-1 and F-3 in Campbell Scientific Inc. (2017). Method is sourced from Foken et al. (2012). Wind direction is given in the sonic anemometer's coordinate frame. *Grade corresponding to Figure 3.3.

Overall QC grade	RN_{cov} (%)	ITC_{sw} and ITC_{tau} (%)	Wind direction (º)
1	0–15	0–30	0–150 or 210–360 (1)*
2	15–30	0–30	
3	0–30	30–75	
4	30–75	0–30	
5	0–75	30–100	
6	75–100	75–100	150–170 or 190–210 (2)
7	100–250	100–250	
8	250–1000	250-1000	
9	≥1000	≥1000	170–190 (3)

The overall average QC grade for the Flux Network is 4.8 (since installation and up to April 1, 2019). As shown in Figure 3.1, overall QC grades differ considerably for each flux and each site. The network average QC grade for τ was 3.9, which was 1.5 points better, than the other fluxes (*FC*, *H*, and *LE*). Latent heat flux had an average grade of 5.1; *FC* was 5.2; and *H* was 5.8. In terms of overall QC grade, SOUT, STAT, and QUEE were consistantly ranked in the top 5 for all fluxes. PENN, REDF, REDH, SCHU, and WHIT were consistantly ranked in the bottom 5. Daytime QC grades were, on average, 1.1 points better than nighttime average QC grades. The range of the night-day difference was 1.8 points on average.

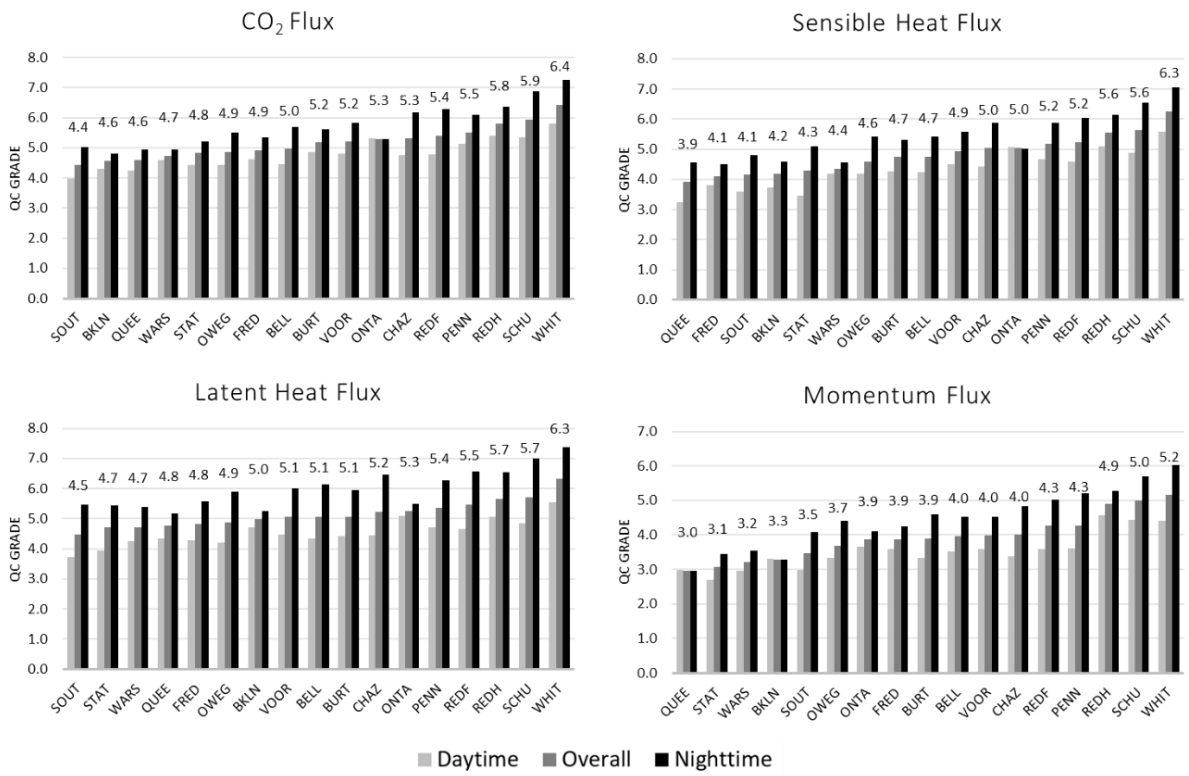

Figure 3.1. Average QC grades for all flux sites and fluxes. Data period is from the site installation to April 1, 2019. Overall average QC grade is labeled above each site. The sites are ordered from best to poorest (left to right) in terms of overall QC grade. Daytime includes data periods where SW↓ ≥ 5 Wm^{-2}. Nighttime data periods include records if SW↓ < 5 Wm^{-2}.

As shown in Figure 3.2a, flux sites with higher average wind speeds have better QC grades. Each point represents an average QC grade and wind speed at a single flux site. The QC grades for *H*, *LE*, and *FC* were averaged together for simplicity and given their similarity. The QC grade for τ improves approximately 0.57 points for every 1 ms^{-1} of wind speed (r^2=0.57). The QC grade for *H*, *LE*, and *FC* improves by about 0.49 points per 1 ms^{-1} of wind speed (r^2=0.60). This trend explains the tendency for QC grade to be worse at night. Nocturnal boundary layers are often stable and calm (Stull 1988). A lack of turbulence in the surface layer can compromise EC measurements (Munger et al. 2012). The overall QC grade takes turbulence characteristics into account with the ITC_{tau} and ITC_{sw} parameters. A linear regression analysis was also

performed to identify how QC grade was influenced by average fetch size (Figure 3.2b), mean terrain slope within 500 m of the tower (Figure 3.2c), and standard deviation of slope within 500 m of the tower (Figure 3.2d). No significant trend could be identified.

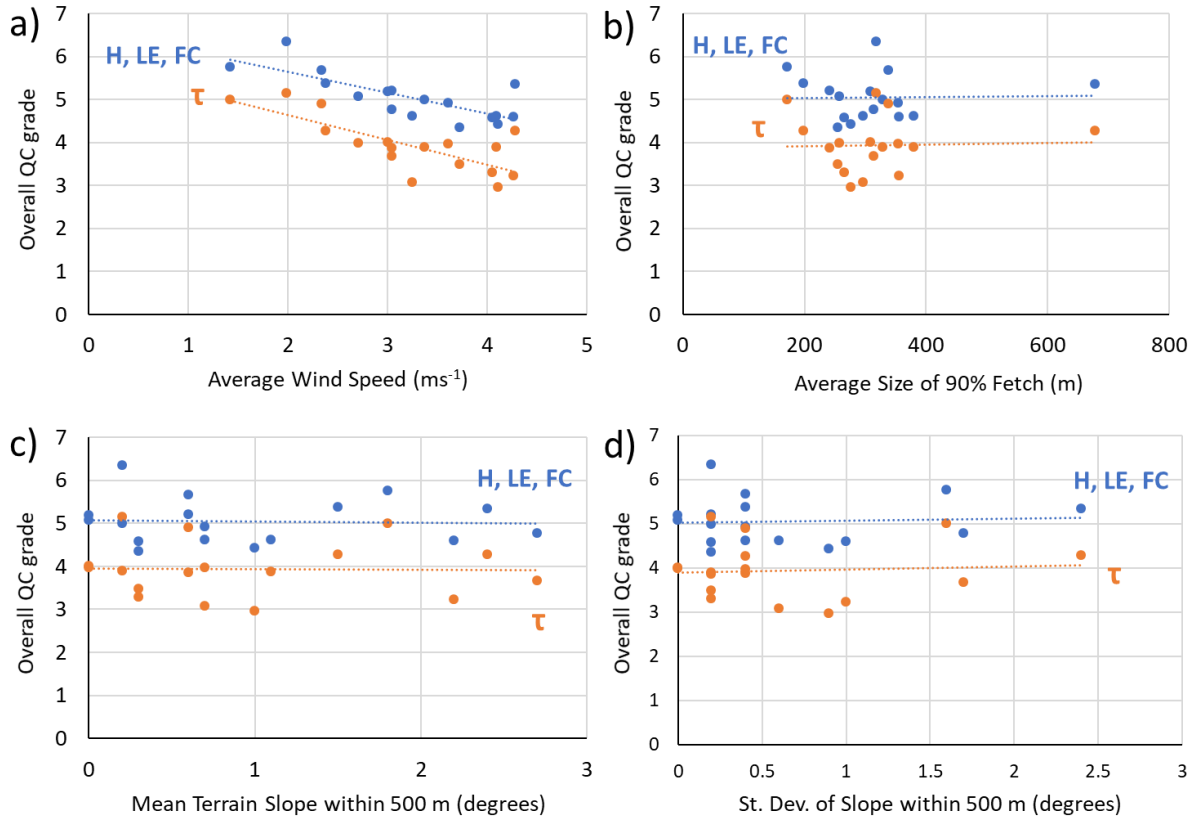

Figure 3.2. Linear regression of overall average QC grades with (a) average wind speed, (b) average size of 90% Fetch determined using the Kljun et al. (2015) two-dimensional Flux Footprint Prediction (FFP) model, (c) mean terrain slope within 500 m of the tower, and (d) standard deviation of slope within 500 m of the tower. Data period is between March 1, 2017 and April 1, 2019. QC grades for *H*, *LE*, and *FC* were averaged together.

Figure 3.3 shows the percent of flux data records graded according to each wind direction category defined in Table 3.2. The sites are listed from highest to lowest (left-right) weighted average ($\overline{QC_{weighted}}$) of the three QC grade categories for wind direction (1, 2, and 3), indicated by the subscripts in Equation 32:

$$\overline{QC_{weighted}} = \frac{3}{3}QC_1 + \frac{2}{3}QC_2 + \frac{1}{3}QC_3. \quad (32)$$

Infrastructure-sourced flow distortion from the structure of the sonic anemometer and tower is the least impactful at the sites on the left, and the most impactful at the sites on the right. Eighty percent or more of the data records at WARS, ONTA, BKLN, VOOR, REDF, and STAT were likely unaffected by infrastructure-sourced wind flow distortion. The differences observed between the sites are correlated to the climatological wind direction. WHIT, SCHU, and REDH, for instance, all experience northeast-southwest valley axis flow. Northeasterly wind must pass through or around the tower before being measured by the sonic anemometer, hence flow distortion is significant (note the placement of the instruments in Figure 2.5c).

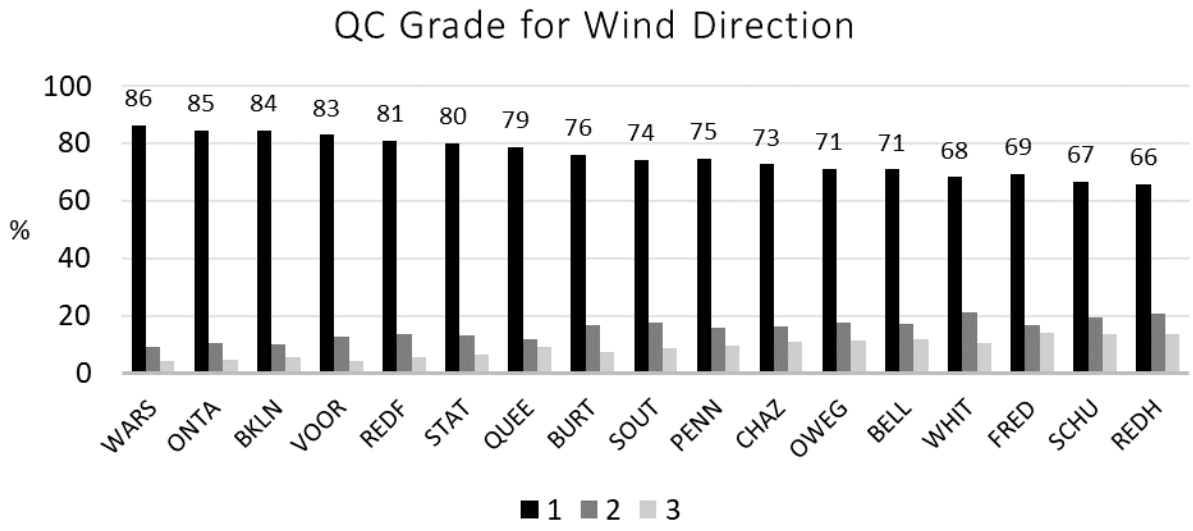

Figure 3.3. Percent of the data record assigned wind direction grades, as defined in Table 3.2. A grade of 1 suggests minimal flow distortion from the structure of the sonic anemometer and tower. The label indicates the value for % of records in category 1.

Figure 3.4 shows the percent of flux data records with four ranges of overall QC grades, separated by flux. The sites are listed from highest to lowest (left-right) by weighted average ($\overline{QC_{weighted}}$) of the four QC grade categories (1–3, 4–6, 7–8, and 9), indicated by the subscripts in Equation 33:

$$\overline{QC_{weighted}} = \frac{4}{4}QC_{1-3} + \frac{3}{4}QC_{4-6} + \frac{2}{4}QC_{7-8} + \frac{1}{4}QC_{9} \quad (33)$$

QC grade categories, 1–3, 4–6, 7–8, and 9, will be referred to in terms of flux data quality: 1–3 = good, 4–6 = fair, 7–8 poor, and 9 = unacceptable. On average, 46% of flux data records are good quality, 12% are fair quality, 25% are poor quality, and 17% are unacceptable. Momentum flux had the highest percentage of good and fair quality data at 70%; followed by *H* at 57%, *LE* at 53%, and *FC* at 53%. CO_2 flux had the highest percentage of unacceptable fluxes at 19%, followed by LE at 18%, H at 18%, and τ at 15%. WHIT, SCHU, and REDH were the only sites that had a higher percentage of poor and unacceptable data than good and fair quality data. The percent of poor and unacceptable data at WHIT, SCHU, and REDH was 62%, 54%, and 53% respectively.

The low overall QC grades at WHIT, SCHU, and REDH sites are due to a combination of low average wind speed and their valley axis wind flow. Switching the location of the sonic anemometer and gas analyzer with the net radiometer, will likely improve the overall data quality of fluxes at these sites. CHAZ and VOOR are subject to a valley axis wind and similar average wind speeds as WHIT, SCHU, and REDH. However, the dominant wind directions at CHAZ and VOOR are northwest and southeast, as opposed to northeast and southwest. Since the sonic anemometer extends off the tower toward the southwest, the tower is rarely upwind of the sonic anemometer at CHAZ and VOOR. The percentage of good and fair data quality data at CHAZ and VOOR is 24% higher than at WHIT, SCHU, and REDH.

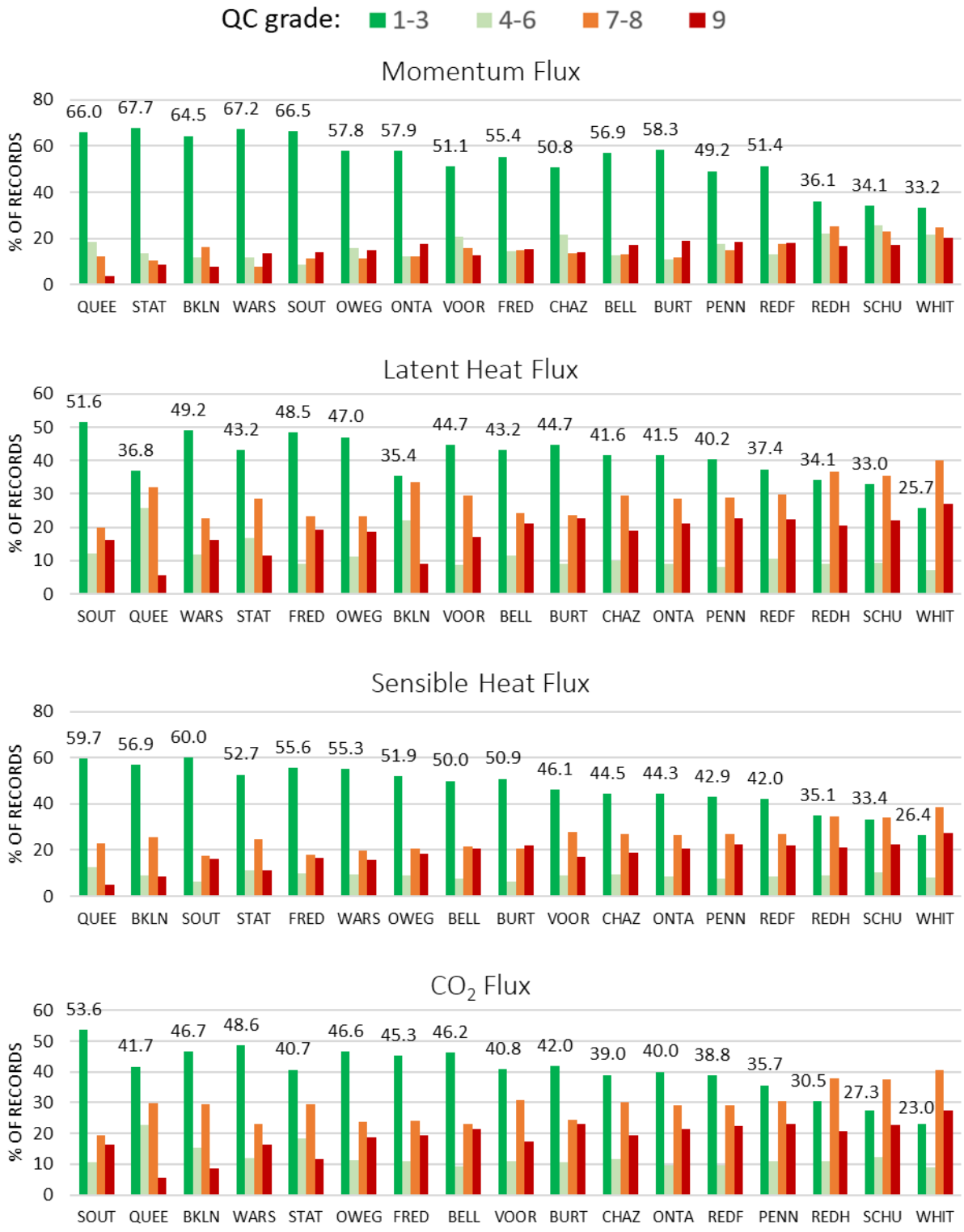

Figure 3.4. Percent of 30-minute flux records graded in four categories.

3.3 Flux Footprints

A fetch is defined as a range of distance upwind of the tower from which the flux was sourced. When a fetch is calculated many times (once per half hour interval), it can be used to generate a flux footprint as a function of wind direction. A two-dimensional footprint was created for each NYSM flux site using the Kljun et al. (2015) two-dimensional Flux Footprint Prediction (FFPonline) model. The model generates estimates of the flux tower's fetch using mean wind speed at the measurement height, L, standard deviation of lateral wind velocity, u_*, and wind direction. The model also requires input of measurement height, d, and z_0. A minimum of 3 months of flux measurements were used to compute the footprints.

A labelled example of these footprints is provided in Figure 3.5a. In Figure 3.5b, the footprint was overlaid on a visible satellite image that was classified according to land cover. The land cover classification was weighted according to the 2D footprint to determine the land cover representation for each flux site. The land cover representation for each flux site is presented for all flux sites in Figure 3.7.

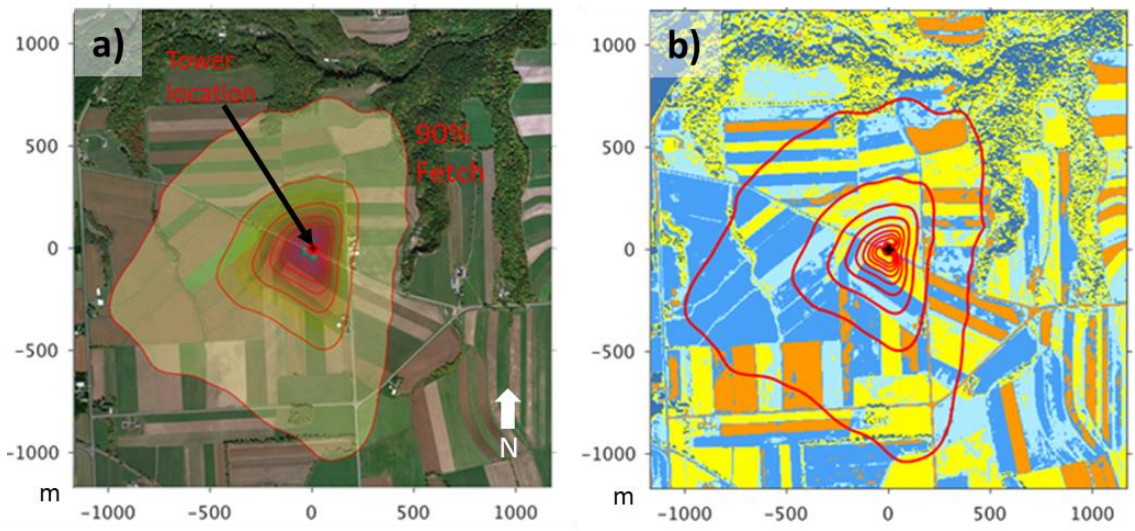

Figure 3.5. (a) A climatological flux footprint for PENN with a visible satellite basemap. The shading of the 2D footprint corresponds to frequency of the fetch. The outermost contour indicates the extent of the 90% fetch. Each additional contour approaching the tower location is a 10% interval (i.e. 80%, 70%, 60%, etc.) (b) A climatological flux footprint of PENN overlaid over an unsupervised classification of the land cover. Both plots are generated using the FFPonline tool (Kljun et al. 2015).

Land cover representation is dependent on wind direction at flux sites with heterogeneous surroundings. As shown in Figure 3.6, CHAZ, VOOR, and REDH experience along-valley flows that result in their footprints extending in opposite directions at equal frequency. At CHAZ, northerly winds cause the flux to be representative of shrubbery while southerly winds result in fluxes representative of a crop field. The crop fields to the east and west are rarely sampled. At VOOR, northeast wind yields flux measurements of a grassy field, while southwest wind results in measurements representative of an orchard. At REDH, north winds result in fluxes from an area of grass and small trees while south winds yield fluxes from a developed area. At ONTA, a 2500 m^2 irrigation pond exists to the south of the flux tower. Though southerly wind is less common than westerly and easterly wind, users of the data should be aware that fetches extending south may include influence from the pond. BURT is unique among flux sites because it sits at the edge of a crop field and a vineyard. Wind tends to prevail from the west, but the two

fields are sampled equally in terms of frequency. PENN has the longest fetch, extending a kilometer to the southwest and south.

One third of the flux, average over the NYSM Flux Network, is sourced from agricultural land. Cropland accounts for 55% of the agricultural representation; followed by vineyard at 30%, and orchard at 15%. Another third of the flux measured by the Flux Network is from grassy fields. Grass is sampled at nearly all flux sites because of its presence nearby to the tower. Landscaped grass refers to grassy fields that are kept at a short height for recreational or aesthetic purposes (e.g. a soccer field). The footprint of BKLN, STAT, and QUEE is dominated by asphalt pavement and rooftops. Together, these sites account for 93% of the urban features represented by the network. SCHU is the only site that contains a significant amount of open water, at 14%.

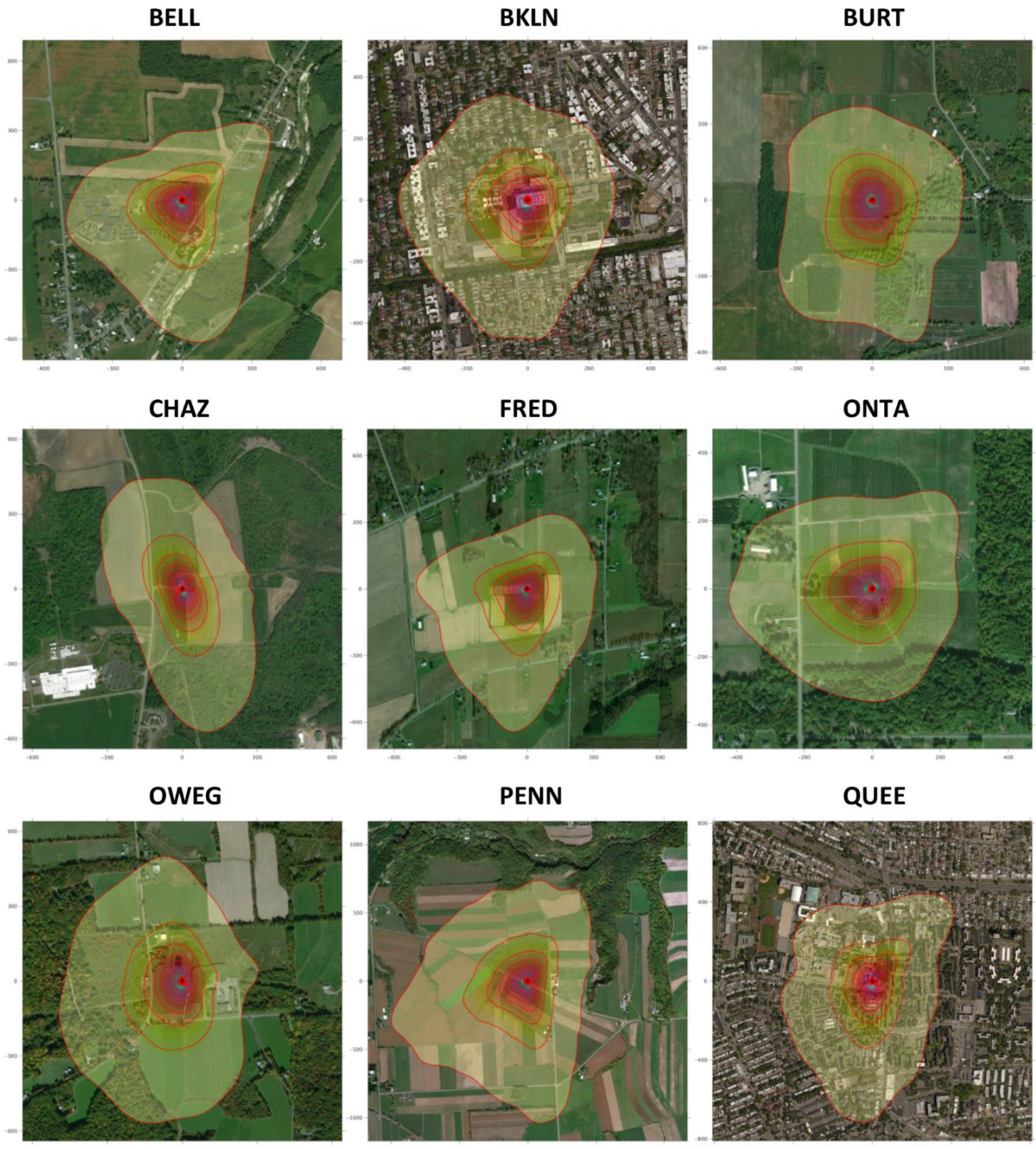

Figure 3.6a. A climatological flux footprint of flux sites over satellite imagery. Plots are generated using FFPonline tool (Kljun et al. 2015). Footprints are calculated using flux data collected between June 1, 2018 and August 31, 2018. Shading indicates frequency of fetch.

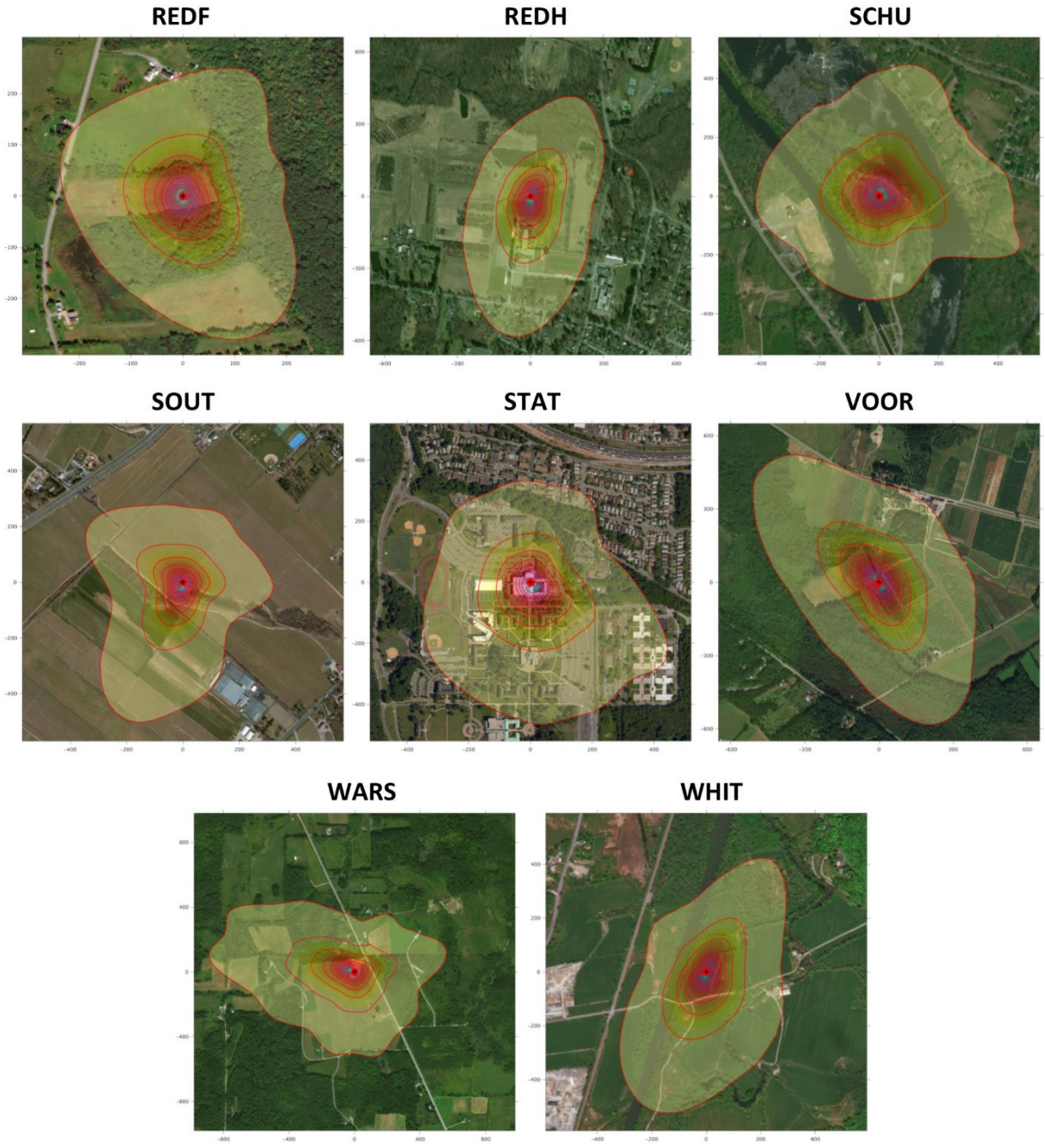

Figure 3.6b. A climatological flux footprint of flux sites over satellite imagery. Plots are generated using FFPonline tool (Kljun et al. 2015). Footprints are calculated using flux data collected between June 1, 2018 and August 31, 2018. At WARS and SCHU footprints were generated using flux data between March 11, 2018 and June 1, 2018. Shading indicates frequency of fetch.

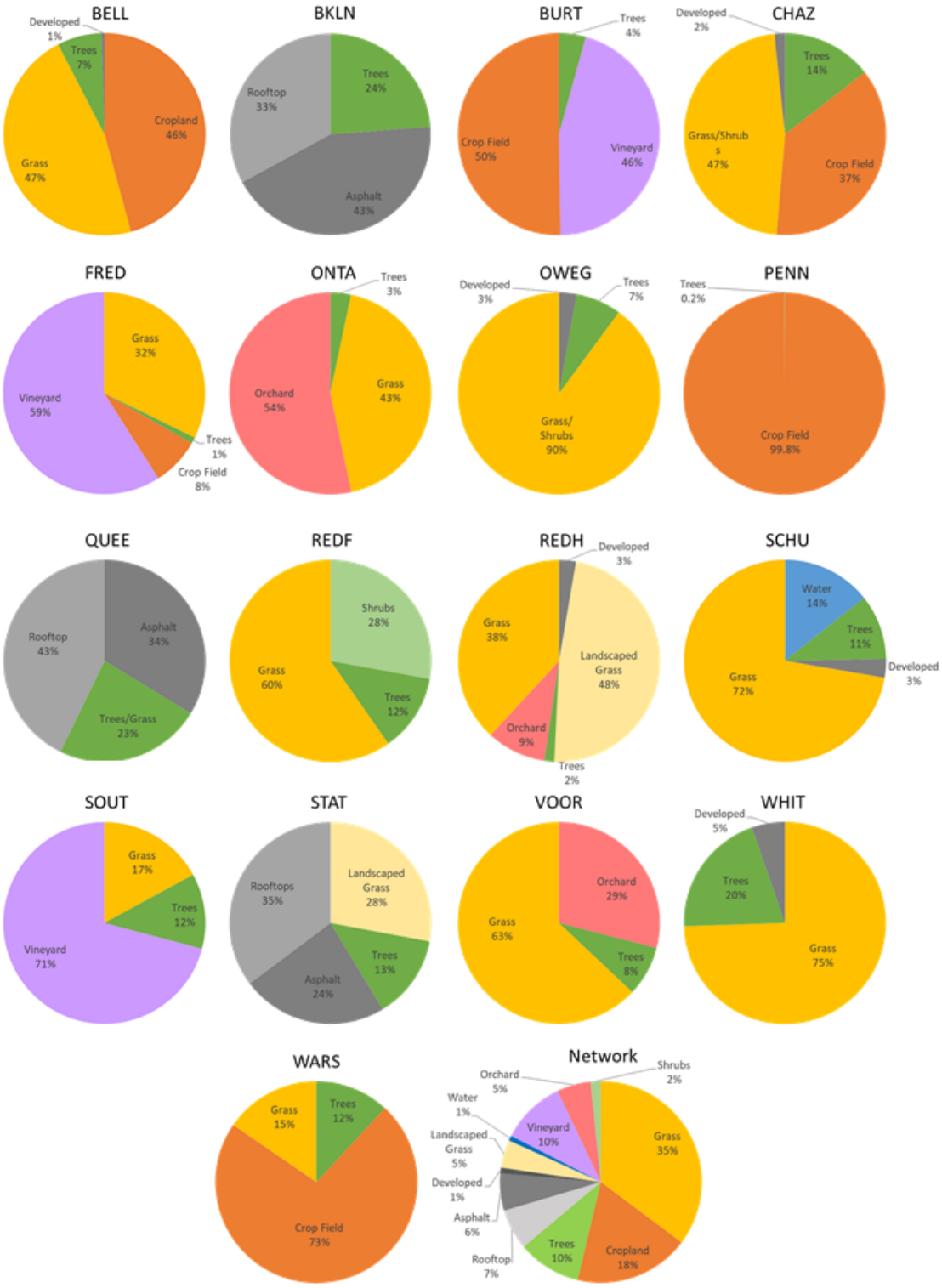

Figure 3.7. Land cover representation determined using Kljun et al.,2015 FFP model. Period of analysis is between Jun 1, 2018 and September 1, 2018, except for SCHU and WARS in which the period of analysis was March 11, 2018 and June 1, 2018.

CHAPTER 4:

Preliminary Results

The goal of this chapter is to present several preliminary results from the first two years of operation of the NYSM Flux Network, with a focus on the spatial and temporal variability in fluxes and CO_2 concentrations. In several instances, hypotheses are presented to explain observed phenomena; however, the in-depth analyses required to evaluate the hypotheses is beyond the scope of this thesis. Rather, these ideas can be viewed as potential topics for future research enabled by the NYSM Flux Network.

4.1 Seasonal Trends

Figure 4.1 shows network-wide composite average time-series of the preliminary quality-controlled fluxes for the lifetime of the Flux Network. NYC sites were excluded from the composite averages. Data were smoothed using a 10-day rolling average and were considered only if their QC grades were < 7.

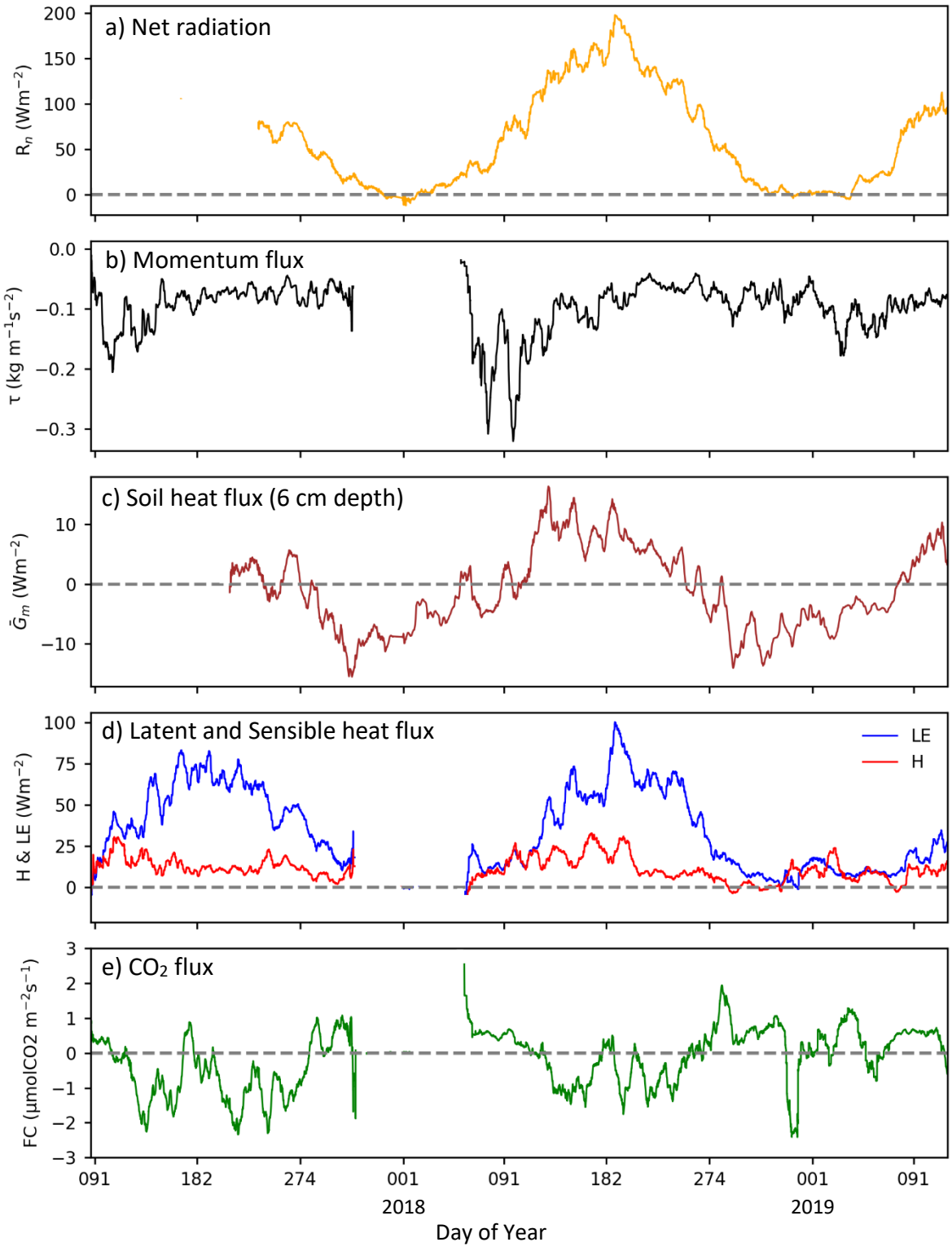

Figure 4.1. Time series of R_n (a), τ (b), $\overline{G_m}$ (c), H (d), LE (d), and FC (e) between March 2017 and April 2019. Time series is a network-wide (less NYC sites) composite average. Data were smooth using a 10-day running mean. QC grade: 1–6.

Seasonal fluctuation of R_n coincides with variation in the solar zenith angle. At its annual maximum in 2018 (day 180), daily average R_n was about 200 Wm^{-2} and daytime R_n was around 680 Wm^{-2}. Net radiation reaches its minimum during the winter (day 1) because of low solar zenith angle, high albedo snow cover, and increased cloudiness. Soil heat flux experiences a similar interannual fluctuation in *Rn*, but peaks in mid spring (~day 130), after which it slowly declines to its minimum around day 315. The peak magnitude of τ in 2018 was -0.30 kg $m^{-1}s^{-2}$ around day 90. Data from 2017, 2018, and 2019 suggest that τ peaks during the winter. Leaf-on conditions are often attributed to lower surface roughness lengths (Maurer et al. 2013). Higher surface roughness lengths during the winter may cause more turbulence that drives momentum flux. This would need to be confirmed for each flux site based on the land cover surroundings.

Sensible heat flux was highest in mid-spring 2018 between days 120 and 200. In 2017, the peak of *H* was around day 100 which was just prior to the start of springtime leaf-out. The peak of *H* prior to springtime leaf-out a common signal in the temperate forests of the Northeastern United States (Fitzjarrald et al. 2001; Wilson et al. 2000). When *H* peaks, R_n is at roughly 80-90% of its annual maximum. The abundance of energy at the surface, combined with the lack of *LE*, results in high *H*. Once leaves emerge and transpiration ramps up, *H* quickly gives way to *LE* as the primary heat flux during the day (Fitzjarrald et al. 2001). Coinciding with increased photosynthetic activity in the growing season, *FC* tends to be negative between days 120 and 270.

The Bowen ratio (β) can be an indicator for timing of spring leaf out (Fitzjarrald et al. 2001). The Bowen ratio describes the proportion of *H* to *LE*:

$$\beta = \frac{H}{LE} \tag{32}$$

Bowen ratios of >1 indicate that most of the heat being exchanged between the surface and the atmosphere is sensible heat (wintertime condition). Values < 1 indicate that most of the heat flux being measured is latent heat (summertime condition). For 2018, visible images collected every 5 minutes at each flux site were analyzed (manually) to determine when the growth of grass and leaves became evident (Table 4.1). The appearance of grass was estimated around April 24, 2018 at most flux sites, and visible leaf emergence began around May 5, 2018. The exceptions were at REDF and WARS where melting of the snow-pack was late relative to the rest of the sites.

Table 4.1: Key dates for Spring 2018 leaf-out (determined from NYSM camera images)

Site	Last day of snowpack* (doy)**	First day of visible grass growth (doy)	First day of visible leaf emergence (doy)
BELL	3/23 (82)	4/24 (114)	5/4 (124)
BURT	3/3 (77)	4/24 (114)	5/4 (124)
CHAZ	3/24 (83)	4/26 (116)	5/4 (124)
FRED	3/24 (83)	4/24 (114)	5/6 (126)
ONTA	3/15 (74)	4/23 (113)	5/6 (126)
OWEG	3/18 (77)	4/26 (116)	5/3 (123)
PENN	3/18 (77)	4/23 (113)	5/7 (127)
REDF	4/24 (114)	5/4 (124)	5/12 (132)
REDH	3/15 (74)	4/24 (114)	5/4 (124)
SCHU	3/24 (83)	4/24 (114)	5/6 (126)
SOUT	3/15 (74)	4/14 (104)	5/4 (124)
VOOR	3/25 (84)	4/22 (112)	5/3 (123)
WARS	4/21 (111)	5/1 (121)	5/8 (128)
WHIT	3/18 (77)	4/25 (115)	5/3 (123)
Average	3/23 (82)	4/24 (114)	5/5 (125)

*Snow on ground is defined as snow pack if it covers about 75% or more of the surface for >48 hours
**Day of year

Figure 4.2 depicts a composite average time series of the noontime (11–13 hrs) β between March 10, 2018 and August 1, 2018 for all non-NYC flux sites. Prior to day 114, β fluctuated around 1.4. Between day 114 and 125, β dropped by ~0.8 as *LE* surpassed *H* due to increased transpiration. This sudden drop in β coincided with leaf-out observed at the flux sites using visible images (Table 4.1). After day 125, β remained under 1 and trended downward to ~0.25 by

day 213. The variability in β observed after day 125 is likely the result of evaporation associated with precipitation events. The troughs of the fluctuation represent periods of higher evaporation and the crests represent periods of lower evaporation.

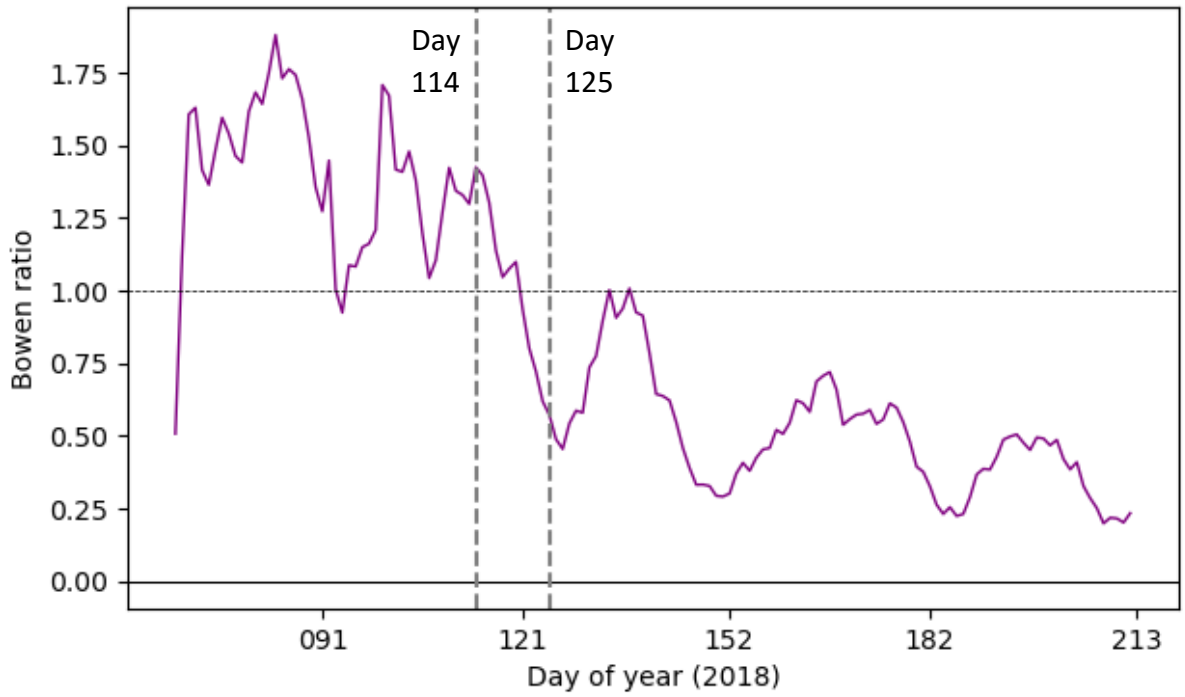

Figure 4.2. Composite average of noontime (11–13 hrs) Bowen ratio for all flux sites excluding BKLN, QUEE, and STAT. The first vertical dotted line to the left indicates the state-wide average day of first visible grass growth (114). The second vertical line represents the average day of first visible leaf emergence (125). Data are valid between March 10, 2018 and August 1, 2018. QC grade: 1–3.

Leaf-out can be confirmed at SCHU using NYSM camera images and *FC*. From the camera images in Figure 4.3c, the growth of new grass can be seen by the increasing intensity of green color in the field. Coinciding with visible grass growth around April 24, 2018, the amplitude of the diurnal cycle of *FC* progressively increases (Figure 4.3a). The diurnal cycle of *FC* became more pronounced once leaves started growing on the trees around May 6 (see May 12 image of Figure 4.3c). The increased variability in *FC* is the result of photosynthesis and

respiration. During the day, the vegetation surrounding SCHU absorbs more CO_2 that it respires. The result is a negative (downward) *FC*. At night, photosynthesis ceases and respiration results in a positive *FC*. CO_2 concentration at night tends to build up, particularly in calm conditions.

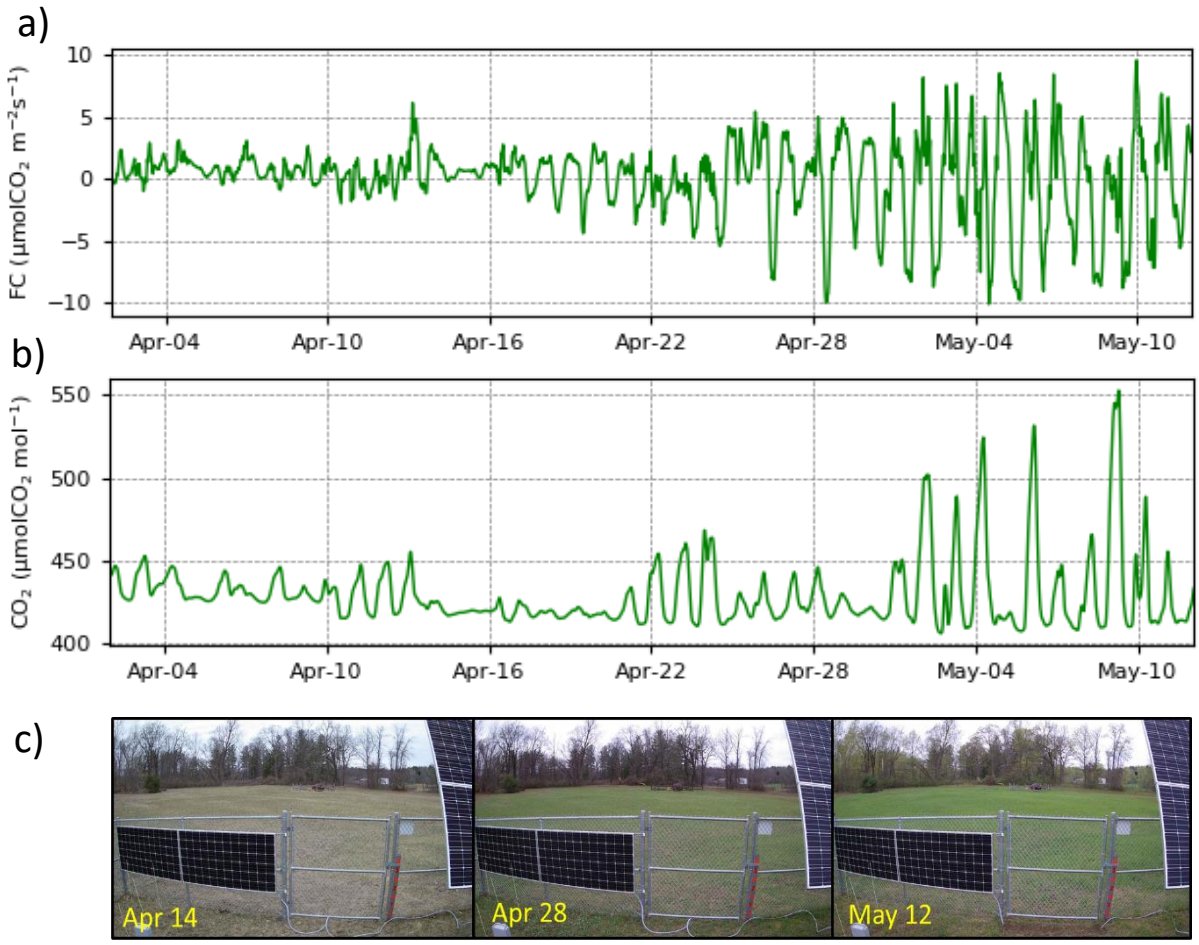

Figure 4.3. (a) Three-hour running mean of FC at SCHU. (b) Three-hour running mean of CO_2 mixing ratio at SCHU. (c) NYSM camera images at SCHU corresponding to the dates noted in yellow. QC grade <9.

Figure 4.4a depicts the seasonal fluctuation of CO_2 mixing ratio at NYC sites (urban) and non-NYC sites (rural). At urban sites, CO_2 achieved its peak mixing ratio during the winter, between day 325 (2018) and day 60 (2019). CO_2 mixing ratios in urban areas tend to be highest during the winter due to emissions from burning of natural gas (Pataki 2003). The rural sites lack

a definitive seasonal peak of CO_2 mixing ratio likely because of the relative lack of anthropogenic emissions.

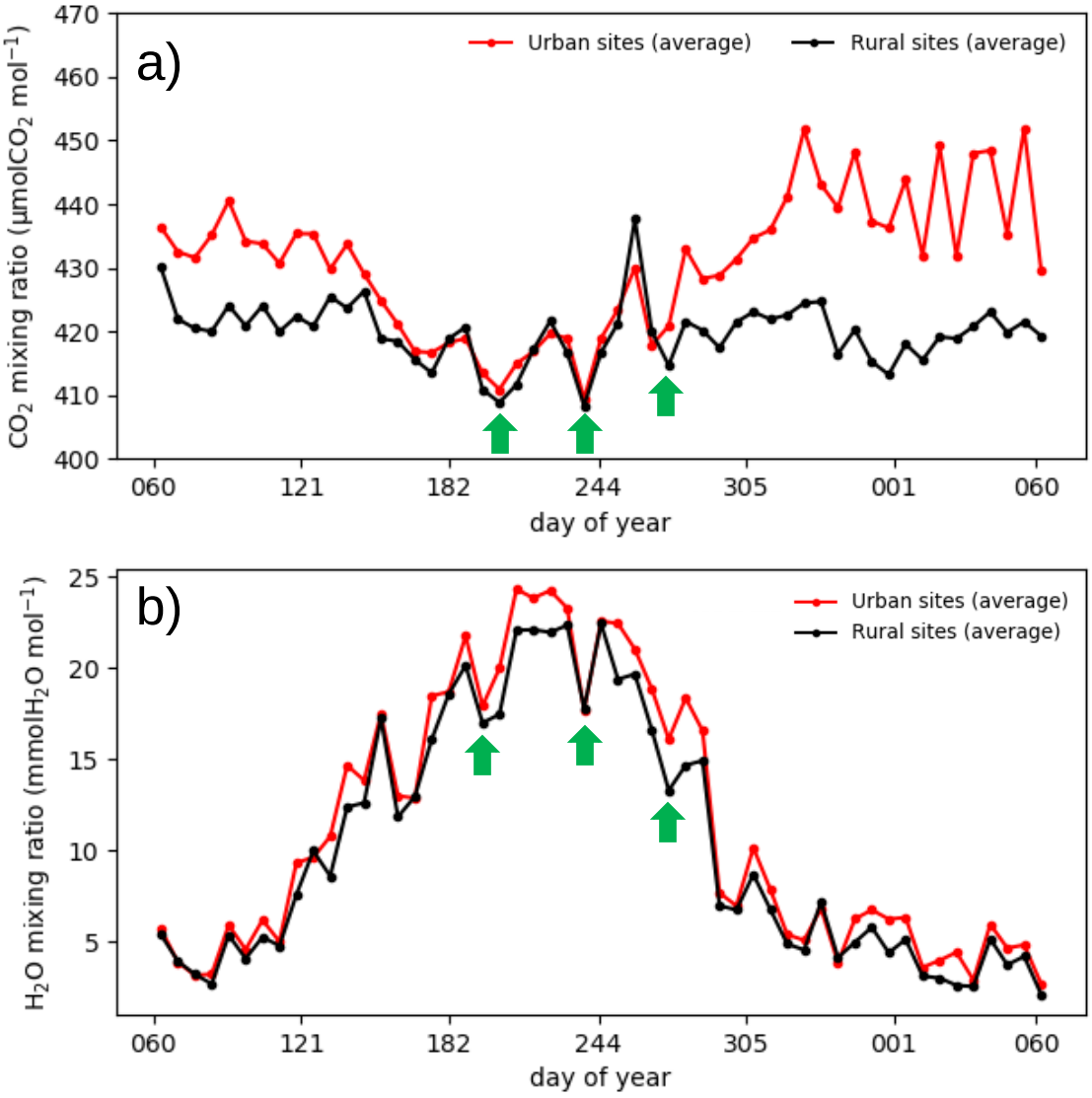

Figure 4.4. (a) Weekly average site composites of CO_2 mixing ratio (a) and H_2O mixing ratio (b). NYC (urban) sites are represented by the red line. All non-NYC (rural) sites are represented by the black line. Green arrows indicate where drops in weekly average CO_2 coincide with drops in weekly average H_2O. These drops are attributed to air mass changes. The data are valid between March 1, 2018 and February 28, 2019.

CO_2 mixing ratio in the summer, at the rural sites appears similar to that of the urban sites when day and night are included in the average (e.g. Table 4.4a). However, the rural sites exhibit

significantly more diurnal variability than the urban sites as a result of respiration and photosynthesis. As shown in Figure 4.5, the standard deviation of CO_2 mixing ratio mixing ratio at rural sites is about 10 ppm higher than the urban sites between days 120 and 275. The highest mixing ratios at the rural sites are measured at night during the summer, due to the buildup of CO_2 in the nocturnal boundary layer from plant respiration. The lowest mixing ratios are measured in the daytime during the summer because the background atmospheric CO_2 is lower, and CO_2 is being absorbed by plants for photosynthesis. Though there are trees present within the footprints of the NYC sites, the diurnal cycle of respiration and photosynthesis is likely masked in the CO_2 signal by variability associated with anthropogenic emissions (i.e. rush hour traffic). This could be explored by comparing the sites based on the quantity of trees within the footprint (e.g. BKLN vs. STAT).

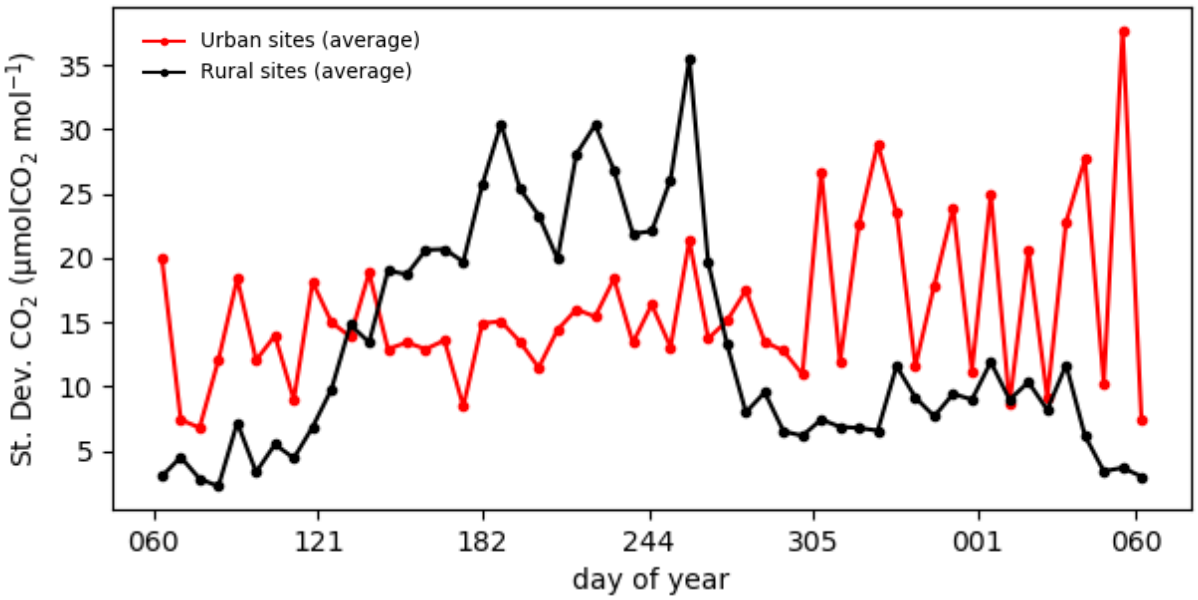

Figure 4.5. Network composite mean of standard deviation of CO_2 mixing ratio over 1-week periods. NYC (urban) sites are represented by the red line. All non-NYC (rural) sites are represented by the black line. The data are valid between March 1, 2018 and February 28, 2019.

Week-to-week variability can be observed in coincident fluctuations of CO_2 and H_2O. Note the green arrows in Figure 4.4. On at least three occasions between days 180 and 300, drops in the weekly average CO_2 mixing ratio coincided with drops in H_2O mixing ratio. The NYC sites and other sites are affected equally by this phenomenon, which is attributed to synoptic variation (e.g. changes in air mass).

4.2 Diurnal Flux Variability

Figures 4.6, 4.7, and 4.8 show diurnal composites of the energy budget terms for 12 flux sites between April 1, 2018 and May 12, 2018. This span of time was selected for the completeness of dataset and to demonstrate spatial variability of fluxes concurrent with springtime leaf-out. Figure 4.6 covers Period 1, between 4/1/2018 and 4/14/2018; Figure 4.7 covers Period 2, between 4/15/2018 and 4/28/2018; and Figure 4.8 covers Period 3, between 4/29/2018 and 5/12/2018.

By comparing each period, signatures of springtime leaf-out can be identified in the diurnal cycle of the turbulent heat fluxes. During Periods 1 and 2, little transpiration occurred throughout the state as evidenced by noon-time Bowen ratios >1. During Period 2, the noon-time Bowen ratio became closer to 1 at several sites (e.g. BELL, SCHU, and CHAZ). This is a signature of increased transpiration. Toward the end of Period 2, around April 24, 2018, new grass became visible at most flux sites. During Period 3, all flux sites, except for REDF, showed signs of increased transpiration with daytime Bowen ratios less than 1. Despite the late onset of grass at WARS, *LE* exceeded *H* during the day, perhaps due to evaporation of snowmelt.

The signature of the snowpack is apparent in the composites of REDF. Relative to the other sites, R_n, H, and LE at REDF was low between hours 8 and 16. There was also no variation in soil heat flux during the day. The high albedo of the snowpack causes a significant proportion of incoming shortwave radiation to reflect to space. Net radiation at the snow-covered surface was likely used for melting (Bilish et al. 2018). Once the snow at REDF melted completely, the diurnal cycle of the fluxes began to more closely resemble those at the other flux sites (Figure 4.8). Because REDF is also an NYSM snow site, the snow melt can be quantified using the snow-water equivalent measurement.

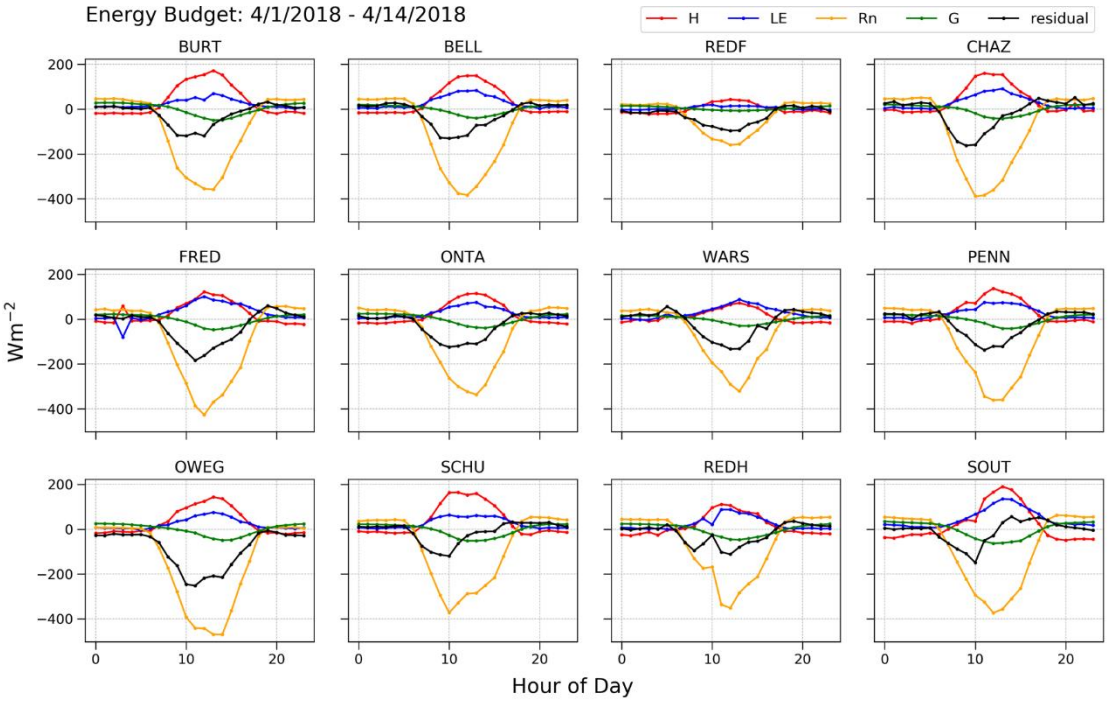

Figure 4.6. Diurnal composite for Period 1 to compare terms of the energy balance including *H*, *LE*, R_n, *G*, and the residual.

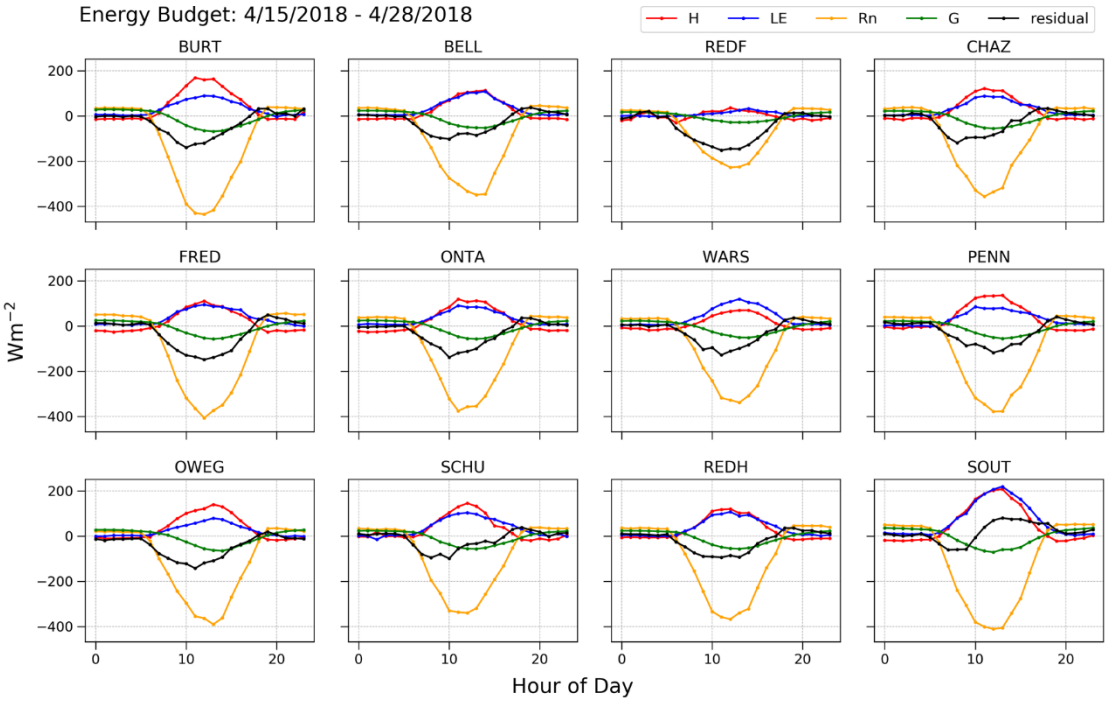

Figure 4.7. Diurnal composite for Period 2 to compare terms of the energy balance including *H*, *LE*, R_n, *G*, and the residual.

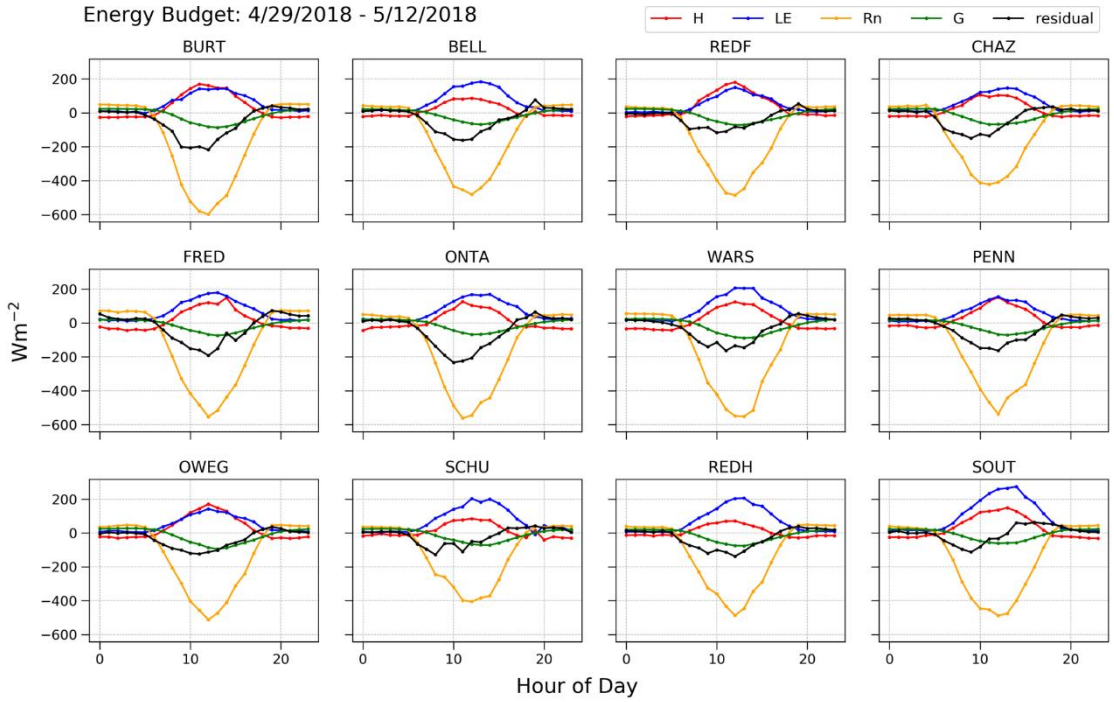

Figure 4.8. Diurnal composite for Period 3 to compare terms of the energy balance including *H*, *LE*, R_n, *G*, and the residual.

4.3 Spatial Variability of Fluxes

Figure 4.9 consists of daytime average of *FC*, *H*, *LE*, τ, R_n, $\overline{G_m}$, H_2O mixing radio, and CO_2 mixing ratio between March 1, 2018 and February 28, 2019. Daytime is defined as any period in which SW$\downarrow \geq 5$ Wm^{-2}. In this analysis, flux sites will be referred to by their U.S. Climate Division as defined in Table 4.2 (Guttman and Quayle 1996). BKLN, QUEE, and STAT were sub-divided from the Coastal division due to the climatological differences with SOUT associated with the NYC urban environment. REDF was sub-divided from the Great Lakes region due to the unique influence of terrain and elevation at the site.

Table 4.2: Modified NOAA climate divisions for NYSM flux sites

Region	Sites
Great Lakes	BELL, BURT, FRED*, ONTA
Great Lakes - Tug Hill Plateau	REDF
Central Lakes	PENN, WARS*
Eastern Plateau	OWEG**
Champlain Valley	CHAZ, WHIT
Hudson Valley	REDH, SCHU, VOOR
Coastal - NYC	BKLN, QUEE, STAT
Coastal	SOUT

*Omitted from annual averages of *FC*, *H*, *LE*, and τ (incomplete year)
**Omitted from annual average of R_n (faulty net radiometer)

The turbulent fluxes are representative of the flux tower footprints, as presented in Chapter 3. Regional averages discussed in coordination with Figure 4.9 should not be interpreted as being representative for entire regions, which are diverse in terms of vegetation, terrain, and land use. However, the footprints are likely influenced by physical and climatological features that define the region that they exist in (e.g. weather patterns, soil type, orographic effects on wind). Sites in the Hudson Valley, for instance, are diverse in terms of land cover representation, but they are impacted by a similar north–south valley wind (Sakai et al. 1998). Likewise, any site on Long Island should be expected to exhibit some ocean influence (e.g. clouds forced by sea breezes) (Freedman et al. 2001). Localized clouds, in particular, can have significant impacts on the surface energy budget and CO_2 fluxes by shading the surface (Freedman et al. 2001; Stull 1988).

Though average turbulent fluxes are presented from the NYC sites in Figure 4.9, they should be interpreted with caution. The degree to which flow distortion impacts the flux measurements has not been fully explored. The NYC sites tend to exhibit relatively high average τ, likely due to the combination of ample turbulence (Section 3.2) and high surface roughness of the urban landscape. It is unclear why there is such a contrast in τ between QUEE and BKLN,

which are surrounded by similar urban landscapes. The representativeness of the NYC flux sites should be explored to better understand such differences in τ and to gain greater confidence in the fluxes.

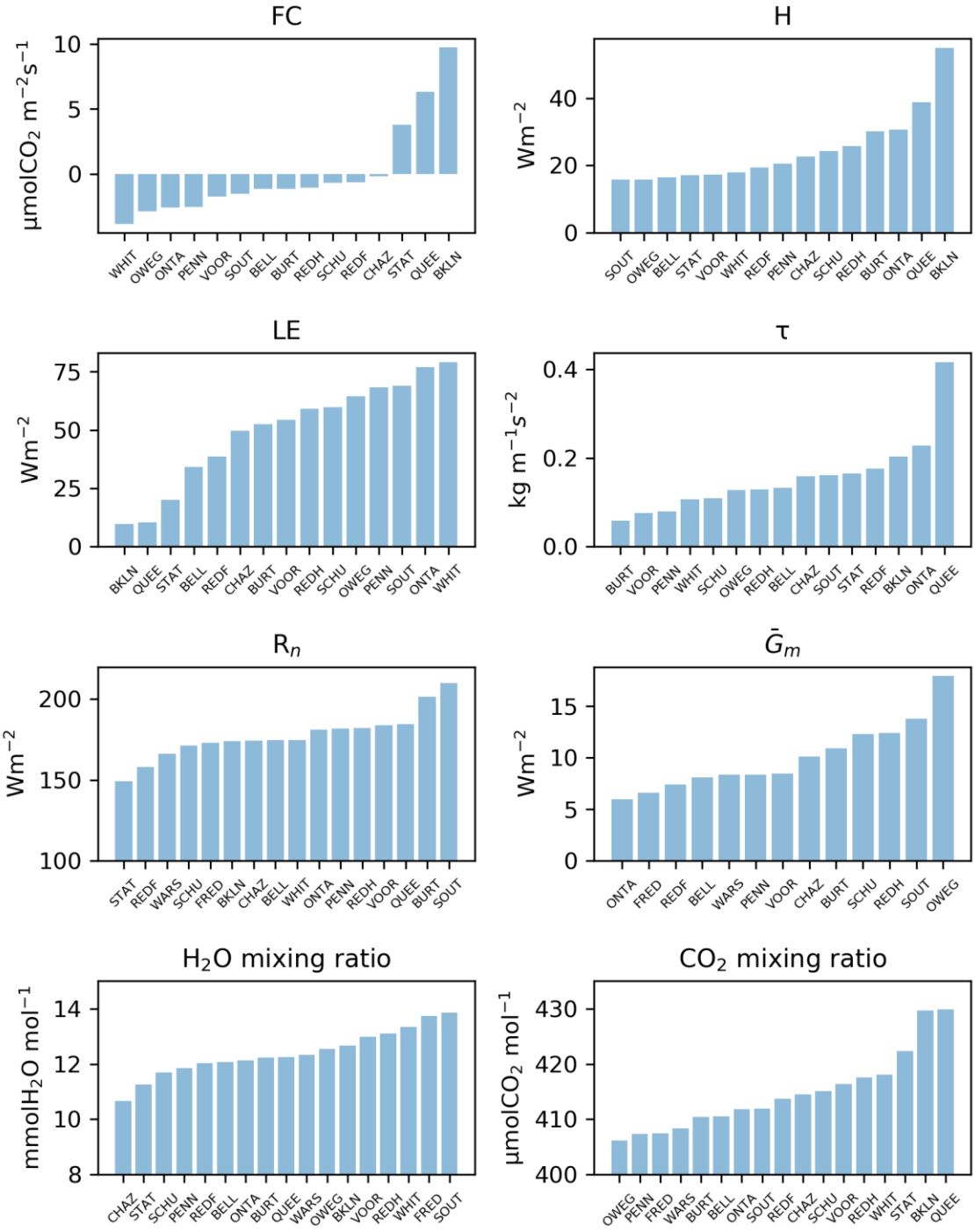

Figure 4.9. Daytime (SW↓ ≥ 5 Wm^{-2}) averages of *FC*, *H*, *LE*, τ, R_n, $\overline{G_m}$, H_2O mixing ratio, and CO_2 mixing ratio for all flux sites. The data period is between March 1, 2018 and February 28, 2019. QC grade: 1–3.

Average *FC* in NYC was 8.0 $\mu molCO_2\, m^{-2}s^{-1}$ higher than the average of all other regions. Urban areas are significant sources for CO_2 due to emissions from vehicles, residential heating, and industrial activities (Mitchell et al. 2018). Average *FC* was negative at all non-urbanized sites likely due to the absorption of CO_2 by the surrounding vegetation and the relative lack of anthropocentric CO_2 emissions. The Central NY sites (OWEG and PENN) had the strongest negative *FC* on average: -2.9 $\mu molCO_2\, m^{-2}s^{-1}$. WHIT had the strongest negative *FC* among individual sites: -3.8 $\mu molCO_2\, m^{-2}s^{-1}$. The spatial variability in *FC* observed among the non-NYC sites is likely influenced by the vegetation characteristics within the footprint of the flux towers. The spatial variability in *FC* should be investigated further by distinguishing the type and characteristics of vegetation surrounding the flux towers.

CO_2 mixing ratio in NYC was 13.9 ppm higher than the average of all other regions. The most urbanized flux sites, BKLN and QUEE had an average CO_2 mixing ratio of 429.7 ppm which is 7.4 ppm higher than STAT, and 11.7 ppm higher than the highest non-NYC site, WHIT. The Hudson Valley exhibits a relatively high average CO_2 mixing ratio compared to other regions in the state — 5.3 ppm higher on average excluding NYC. A hypothesis is proposed for this phenomenon: When the stable boundary layer forms in the Hudson Valley at night, the air in the valley is de-coupled from the free atmosphere (Fitzjarrald and Lala 1989). As a result, CO_2 accumulates in the valley due to plant respiration and anthropogenic emissions. The elevated CO_2 concentration remains high during early daylight hours before the CO_2 can be effectively mixed throughout the PBL. In support of this hypothesis, Figure 4.10 shows a diurnal composite of CO_2 where concentration builds up disproportionally in the valley flux sites (indicated in red).

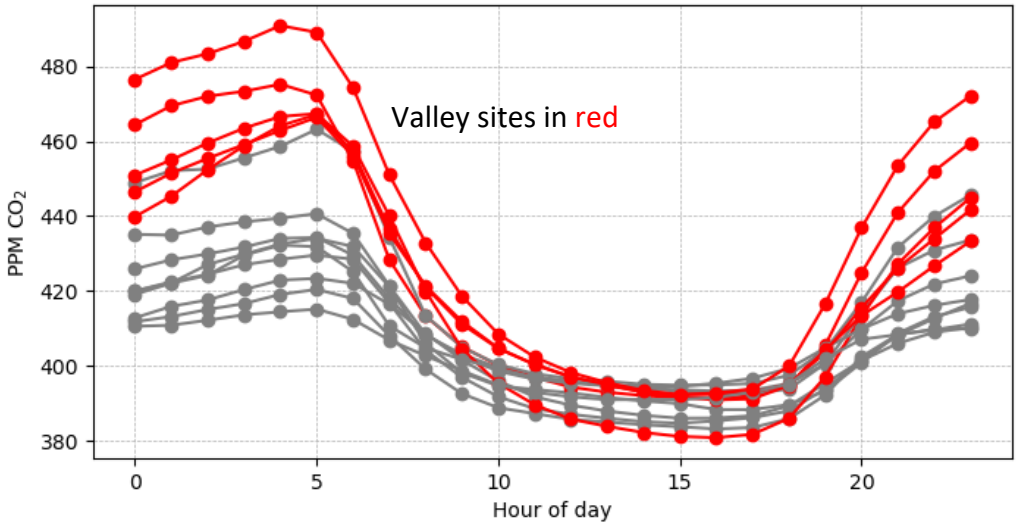

Figure 4.10. Diurnal composite of average CO_2 mixing ratio between June 1, 2018 and August 31, 2018. Each flux sites correspond to a line. Flux sites that exist in valleys, CHAZ, REDH, SCHU, VOOR, and WHIT, are represented by the red lines. NYC sites are excluded from the plot.

The high average *H* (44.7 Wm^{-2}) and low average *LE* (14.3 Wm^{-2}) in NYC is clearly distinguishable from the values in other regions. On average, daytime *LE* at non-NYC sites was 59.2 Wm^{-2}, and *H* was 22.1 Wm^{-2}. The contrast can be attributed to the lack of vegetation in NYC. As discussed in Section 4.1, the seasonal variation of *LE* at QUEE, BKLN, and STAT is minimal compared to the non-NYC sites due to the impact of transpiration on the surface energy budget. Sensible heat flux and *LE* are damped in the Tug Hill Plateau, likely due to the relatively long snow season. Snow cover has high albedo and therefore limits the amount of energy that is absorbed by the surface (Tarboton 1994). Sensible heat flux was 12% lower at REDF than all other sites (NYC excluded) and *LE* was 35% lower than all other sites.

The variability in R_n is a function of cloud cover and surface albedo. R_n for STAT, BKLN, and QUEE is relatively low because the net radiometer faces a high albedo rooftop. SOUT, representing Long Island, has the highest R_n, 209.9 Wm^{-2}, the second highest $\overline{G_m}$, 13.8

Wm^{-2}, and the highest H_2O mixing ratio, 13.8 $mmolCO_2\ m^{-2}s^{-1}$. The weather on Long Island is significantly impacted by the ocean. Net radiation is high due to the relative lack of cloud cover on Long Island compared with other regions in NYS. With more energy being absorbed by the surface, the gradient of temperature in the soil is greater, leading to more heat flux into the soil. Water vapor evaporated from the ocean advects across the region causing the relatively high H_2O mixing ratio.

4.4 Energy Budget Closure

Figure 4.11 shows the linear relationship of total available energy ($R_n - G$) versus turbulent heat fluxes ($H+LE$) between June 1, 2018 – August 31, 2018. Each point represents a single half-hourly flux. Fluxes were included in the calculation of energy budget closure if their QC grade was < 6. A linear regression was performed on the data to determine the slope and y-intercept. In the event of perfect closure of the energy budget, the slope will be 1 and the y-intercept will be 0.

Table 4.3. Daytime (SW↓ ≥ 10 Wm^{-2}) energy budget closure statistics for the period of March 1, 2018 – February 28, 2019. Slope, y-intercept (y-int), and r^2 are results of the linear regression of $R_n - G$ and $H+LE$. Mean and standard deviation (SD) are provided for Residual, and 90% fetch. The number of records included in the analysis is indicated by n.

Site	Slope	y-int.	r^2	Residual	Residual SD	90% Fetch	Fetch SD	n
BELL	0.72	-15.16	0.87	79.5	115.7	318	683	4422
BURT	0.69	5.75	0.89	60.2	117.0	300	470	4229
CHAZ	0.72	1.09	0.86	56.6	117.0	310	804	4504
FRED	0.61	4.87	0.86	65.7	174.0	400	871	1616
ONTA	0.54	24.99	0.75	66.0	167.2	219	186	3736
PENN	0.69	-3.50	0.88	66.6	117.8	662	1729	4056
REDF	0.78	-15.59	0.82	57.0	158.7	202	190	3973
REDH	0.72	4.17	0.81	58.8	143.9	278	593	3468
SCHU	0.77	5.80	0.82	39.9	149.0	137	483	4012
SOUT	0.81	7.05	0.79	32.7	131.4	240	293	5394
VOOR	0.67	3.76	0.87	69.9	127.6	253	340	3731
WHIT	0.72	0.19	0.87	56.4	191.7	292	495	2847
All sites	0.70	1.95	0.84	59.1	142.6	301	595	3832

The statistics from the energy budget closure calculations are included in Table 4.3. The average closure, for all twelve flux sites, according to the linear fit slope was 70%. The site with the highest closure was at SOUT, 81%, and the site with the lowest closure was ONTA, 54%. The r^2 for SOUT was 0.79 and r^2 for ONTA was 0.75. The y-intercepts ranged from -15.59 at REDF to 24.99 at ONTA. At REDF, the closure was 0.78, the second highest of all the sites. NYSM closure is comparable with the closure reported at FLUXNET towers. Wilson (2002) evaluated energy budget closure at 50 FLUXNET towers and found the minimum closure was 55%, the maximum was 99%, and the median was 78%. Brotzge (2000) found an average closure of 92.4% by removing cloudy and rainy days from the data record.

Brotzge (2000) found a weak correlation of energy budget closure to standard deviation and mean of terrain slope within 500 m of Oklahoma Mesonet towers. No statistically significant correlation between mean terrain slope and energy budget closure was found at NYSM sites. Closure decreases about 1% per degree of standard deviation of terrain slope within 500 m of the tower, but the correlation is not significant (r =0.19). Eshonkulov et al. (2019) found that data periods with small footprints tended to exhibit the best energy budget closure. No correlation in footprint size and energy budget closure could be identified at NYSM flux sites.

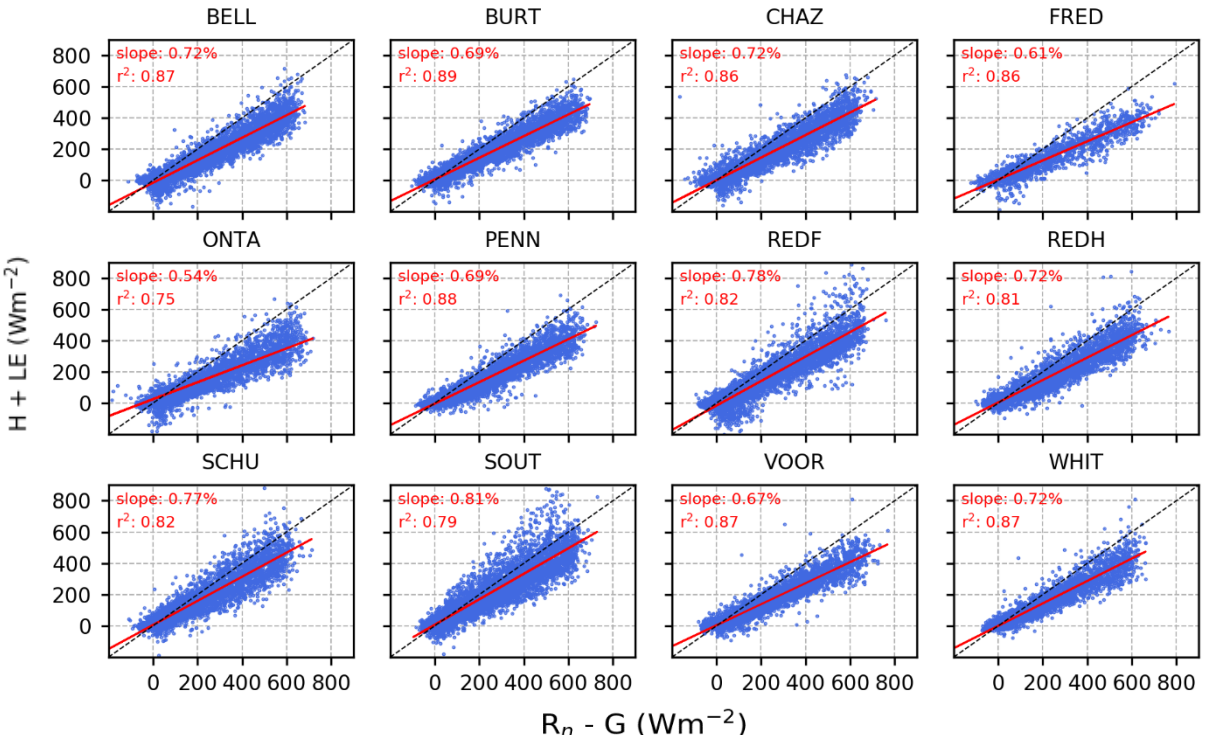

Figure 4.11. Daytime ($SW\downarrow \geq 5$ Wm^{-2}) energy budget closure for 12 flux sites between the period of 6/1/2018 and 9/01/2018. Turbulent fluxes are on the y-axis and the total available energy is shown on the x-axis. Each dot corresponds to a half-hourly flux. Slope indicates the degree to which the energy budget closes when averaged over a time period. QC grade: 1–5.

In Figure 4.11, both REDF and SOUT exhibit a notable concentration of datapoints above the 1:1 line. These datapoints indicate that turbulent fluxes are higher than the total amount of

energy available. This discrepancy may be the result of local advection of heat into the footprint or the result of the difference in footprint size for the net radiometer and the EC instruments.

Figure 4.12 shows wind direction dependence of energy budget closure at the flux sites. The energy budget closure was quantified in terms of energy budget ratio (EBR):

$$EBR = \frac{LE+H}{R_n-G}. \quad (24)$$

EBR was calculated and averaged into groups based on wind direction. Extreme outliers of EBR, exceeding 3 times the inter-quartile range, were omitted from EBR averages. Most fluxes from the NNE are omitted from the data record due to the flow distortion potential from the tower. There is notable direction dependence in the energy budget closure at several flux sites.

At SOUT, wind from the west results in an EBR > 1 (i.e. over-closure). Flux data taken while the wind blows from the west appears to cause the anomalous points noted above. EBR at SOUT is relatively high in all directions (~0.7) compared to the other flux sites. Closure at SOUT is best when wind blows from the south and east. At REDF, the observed over-closure is caused by wind from the north. EBR at REDF is low (~0.25) when wind blows from the south-east. The presence of trees 45 m north, east, and south of the tower are likely impactful on the fluxes. More research will need to be done to establish how the proximity of trees affects the energy budget closure at REDF (i.e. by inducing flow distortion).

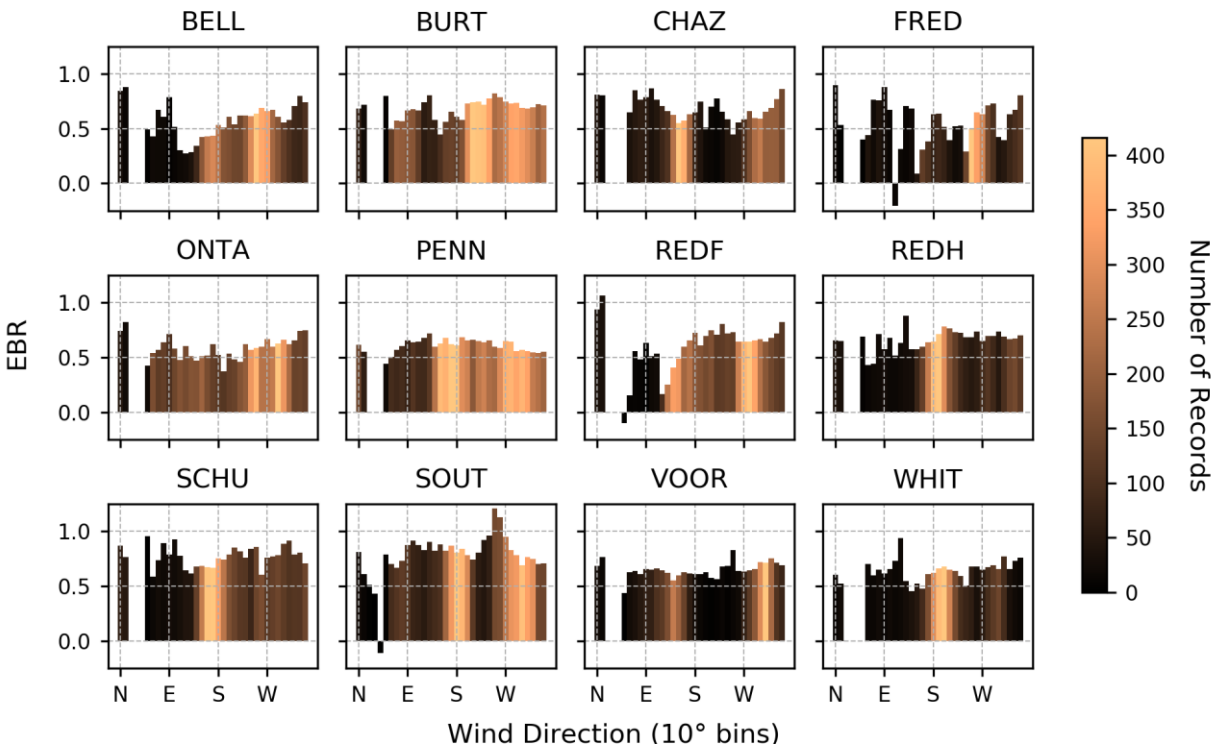

Figure 4.12. EBR averaged into 10° wind direction bins. The colors correspond to the number of records in each bin. Data is between June 1, 2018 and August 31, 2018 and only includes fluxes taken during the day ($SW\downarrow \geq 5$ Wm^{-2}). QC grade: 1–5.

CHAPTER 5:

Future Work

The NYSM is unique among mesonets with regard to the combination of standard meteorological data, vertical profilers, and surface flux measurements. Here, several potential research possibilities are presented. Two types of future work are identified: science and technical/logistical.

Green vegetation fraction (GVF) is proportional to the amount of the land surface covered in green vegetation. As revealed in Section 4.1, the presence of green vegetation strongly impacts the surface energy balance (particularly *LE*). The Noah land surface model (LSM) implemented in current operational NOAA NWP models, uses multi-year monthly averages of GVF derived from satellite imagery (Niu et al. 2011; Fang et al. 2018). The use of climatological values for GVF is problematic when the timing of leaf-out is not consistent year-to year. For instance, the author found that leaf-out occurred about one week earlier in 2019 than in 2018 (NYS average). This difference in GVF between the two years, and the subsequent impact on surface energy balance, is not accounted for in existing NOAA NWP models. The NOAA Earth Systems Laboratory is exploring the use of real-time GVF from geostationary satellites (Fang et al. 2018). The NYSM Flux Network can provide a ground-truth to satellite observations and modelled fluxes, especially when timing leaf-out and measuring its impact on the surface energy balance.

The impact of local and synoptic influences on the surface fluxes could be explored with the Flux Network. As discussed in Section 4.1, synoptic variation can be observed in CO_2 and H_2O mixing ratio. The author hypothesizes that calm, high pressure, conditions across NYS

cause local influences on fluxes (e.g. vegetation type, microscale wind patterns) to be more apparent than synoptic influences (e.g. air mass changes, large scale pressure gradients). It is suspected that windy days caused by large-scale pressure gradients will yield more influence from synoptic phenomena and exhibit less individuality among the flux sites. This hypothesis can be explored using the Flux Network given the distribution of towers across NYS.

Given its spatial distribution, the Flux Network is optimal to study transient phenomena (e.g. frontal passages). Though frontal passages occur a limited number of times during a year, due to the proximity of the flux sites to one another, the flux network could potentially yield seventeen samples of a single front. Comparisons between the flux sites for a single event can both improve confidence in the signals observed (e.g. spikes in CO_2 concentration) and provide insight into how such signals depend on land cover and terrain characteristics.

Further effort is required to better constrain the impact of terrain and surrounding land cover on the fluxes. Determining surface roughness, for instance, can help explain the differences in surface temperature and surface energy distribution between flux sites (Burakowski et al. 2018). Drone video and photos of the flux sites will enable more precise classification of the surrounding land use and vegetation. Down-facing lidar imagery can used to analyze the terrain surrounding each tower and potentially be used to determine the surface roughness (e.g. NYS GIS Clearinghouse 2019).

Flux sites are distinct in their ability to close the energy budget. Closure was observed to vary based on wind direction at several sites (e.g. SOUT and REDF). The lack of energy budget closure at the NYSM flux sites could be from a number of sources documented in the literature These possible sources include, but are not limited to; (1) differences in representativeness of turbulent flux, soil heat flux, and net radiation measurements; (2) instrumentation errors; (3) less

than ideal siting; (4) or high and low frequency losses (Brotzge 2000; Foken 2008; Wilson 2002). Further research will need to be done to determine how each of these potential issues affects NYSM flux measurements.

Nine flux systems are permanently co-located with or within 25 km of atmospheric profilers. This co-location of instruments provides research opportunities related to the interaction of surface fluxes with the composition and structure of the boundary layer. For instance, one could consider how columns of updrafts and downdrafts impact surface fluxes, near-surface H_2O concentration, and CO_2 concentration. The NYSM has the capability to identify effects of these mean flows using lidar wind profiles collected approximately every 5 minutes. Column average vertical wind speed can be temporally averaged and compared to half-hourly fluxes.

The NYSM could be used to evaluate the performance of the datalogger program, EasyFlux DL (introduced in 2015 by CSI). A valuable exercise would be to compare its output and corrections with other community accepted flux computation packages such as eddy4R and the Open Network-Enabled Flux Processing Pipeline (ONEFlux) (Chu and Ladislav 2017; Metzger et al. 2017). An evaluation of EasyFlux DL will improve confidence in the preliminary fluxes and allow the NYSM to better communicate uncertainties in the measurements.

Improved power management is necessary to maximize wintertime data recovery, while minimizing the impact of the flux system on the standard site's operation. Over the coming winters, the limits of the NYSM power system will become clearer and we will be able to implement solutions to operate the flux systems more efficiently. Data recovery over the winter of 2018/19 was significantly improved compared to the prior winter due to a power management scheme that made power saving decisions based on the incoming battery bank voltage. By

considering variables such as air temperature, length of day, and incoming solar radiation, the flux system's power management scheme can make "smarter" power saving decisions that will improve data recovery.

It would be useful to examine the effects of the standard site infrastructure on the flux measurements. As with any flux tower, the structure of the NYSM towers is a source for flow distortion, particularly when wind prevails from the northeast. A computational fluid dynamic model (CFD) could be used to gain a better understanding of how wind flows around (and through) NYSM towers. Some flux sites, most notably SCHU, REDH, and WHIT, are especially affected by flow distortion because they experience northeast winds in valley axis flow. Known flow distortion at SCHU, REDH, and WHIT can be mitigated by moving the IRGA and sonic anemometer to a side of the tower that permits the dominant wind flows to reach the sensor unimpeded. The NYC sites will require a more robust analysis of flow distortion because of their siting on rooftops. It is unclear how the buildings influence the flow around the rooftop tower and how that flow impacts the flux measurements.

CHAPTER 6:
Summary and Conclusions

This thesis focused on the design and implementation of the NYSM Flux Network. The 17 flux sites are co-located with 17 of the NYS Mesonet's 126 standard meteorological stations, and utilize solar power with minimal impact to existing infrastructure. The flux sites feature measurements of incoming and outgoing short- and long-wave radiation, soil heat flux, and eddy covariance momentum, heat, moisture, and carbon dioxide fluxes. Closed-path gas analyzers were used to measure CO_2 and H_2O, which enabled implementation of automatic calibrations referenced to national CO_2 standards. The consistent instrumentation, data acquisition, and computational methods across the flux sites reduces uncertainties due to experimental design and facilitates inter-site comparisons.

To date, the network has archived over 12 billion raw measurements and nearly 250,000 hours of calculated fluxes in a variety of environments across NYS, including agricultural land, grassy fields, urban, wooded, and developed land. Generally, the first two years of the Flux Network's operation demonstrated high data recovery rates and flux data quality during periods with ample solar power. During winter and extended cloudy periods, automated onboard software reduced power usage by turning off components of the flux system. The flux footprints were analyzed for each site to determine the land cover types contributing to the measured fluxes as a

function of wind direction. Preliminary fluxes were graded by considering the development of turbulence, stationarity, and wind direction.

Preliminary results were presented to demonstrate the temporal and spatial variability of surface fluxes, energy balance closure, and CO_2 concentrations. The temporal (diurnal, seasonal) and spatial variability of the fluxes and CO_2 mixing ratio highlight the utility of the mesoscale resolution of the flux network. For example, the spatial variation in timing of spring leaf-out was determined across NYS using a composite of the Bowen ratio and verified by analysis of visible images taken at the flux sites. Variability in CO_2 concentration was found to occur on site-specific, regional, and network-wide scales. A clear contrast in R_n, τ, FC, H, and LE was apparent between rural and urban sites. Synoptic influences on the measurements were identified by multi-day patterns in CO_2 and H_2O mixing ratio consistent across the state. It would be impossible to identify these patterns with a single tower. The flux network provides abundant opportunities for basic and applied research, especially when combined with the NYSM's standard, profile, and snow site networks.

REFERENCES

Aubinet, M., T. Vesala, and D. Papale, eds., 2012: *Eddy Covariance*. Springer Science+ Business Media, 438 pp. http://link.springer.com/10.1007/978-94-007-2351-1.

Baldocchi, D. D., 2003: Assessing the eddy covariance technique for evaluating carbon dioxide exchange rates of ecosystems: past, present and future. *Glob. Chang. Biol.*, **9**, 479–492.

——, and Coauthors, 2001: FLUXNET: A New Tool to Study the Temporal and Spatial Variability of Ecosystem-Scale Carbon Dioxide, Water Vapor, and Energy Flux Densities. *Bull. Am. Meteorol. Soc.*, **82**, 2415–2434, doi:10.1175/1520-0477(2001)082<2415:FANTTS>2.3.CO;2.

Bilish, S. P., H. A. Mcgowan, and J. N. Callow, 2018: Energy balance and snowmelt drivers of a marginal subalpine snowpack. *Hydrol. Process.*, **32**, 3837–3851, doi:10.1002/hyp.13293.

Brock, F. V, 1986: A Nonlinear Filter to Remove Impulse Noise from Meteorological Data. *J. Atmos. Ocean. Technol.*, **3**, 51–58, doi:10.1175/1520-0426(1986)003<0051:ANFTRI>2.0.CO;2.

Brotzge, J. A., 2000: Closure of the Surface Energy Budget. University of Oklahoma, .

——, and K. C. Crawford, 2003: Examination of the Surface Energy Budget : A Comparison of Eddy Correlation and Bowen Ratio Measurement Systems. *J. Hydrometeorol.*, **4**, 160–179.

——, and Coauthors, 2016: The New York State Mesonet Siting Process and Challenges (96th American Meteorological Society Annual Meeting). *AMS 96th Annual Meeting: 18th Symposium on Meteorological Observation and Instrumentation*, USA.

Burakowski, E., A. Tawfik, A. Ouimette, L. Lepine, K. Novick, S. Ollinger, C. Zarzycki, and G. Bonan, 2018: The role of surface roughness, albedo, and Bowen ratio on ecosystem energy balance in the Eastern United States. *Agric. For. Meteorol.*, **249**, 367–376, doi:10.1016/j.agrformet.2017.11.030.

Burgon, R., S. Sargent, T. Zha, and X. Jia, 2015: Field - Performance Verification of Carbon Dioxide , Water , and Nitrous Oxide Closed - Path Eddy Covariance Systems with Vortex.

Burrough, P. A., and R. A. McDonell, 1998: *Principles Of Geographical Information Systems*. Oxford University Press, New York,.

Campbell, G. S., 1977: *An Introduction to Environmental Biophysics*. New York : Springer-Verlag, [1977], 474 pp.

——, and J. M. Norman, 1998: *An Introduction to Environmental Biophysics*. 2nd ed. Springer, New York,.

Campbell Scientific Inc., 2016: Instruction Manual: CO2 and H2O Closed-Path Gas Analyzer. http://www.campbellsci.com.

——, 2017: Instruction Manual: EasyFlux DL. http://www.campbellsci.com.

——, 2018: Product Manual: Dielectric Leaf Wetness Sensor. http://www.campbellsci.com.

Chu, H., and Š. Ladislav, 2017: A rolling list of software/packages for flux-related data processing. https://fluxnet.fluxdata.org/2017/10/10/toolbox-a-rolling-list-of-softwarepackages-for-flux-related-data-processing/ (Accessed December 11, 2018).

Cohen, A. E., S. M. Cavallo, M. C. Coniglio, and H. E. Brooks, 2015: A Review of Planetary Boundary Layer Parameterization Schemes and Their Sensitivity in Simulating Southeastern U.S. Cold Season Severe Weather Environments. *Weather Forecast.*, **30**, 591–612, doi:10.1175/WAF-D-14-00105.1. https://doi.org/10.1175/WAF-D-14-00105.1.

Cuxart, J., L. Conangla, and M. A. Jiménez, 2015: Evaluation of the surface energy budget equation with experimental data and the ECMWF model in the Ebro Valley. *J. Geophys. Res.*, **120**, 1008–1022, doi:10.1002/2014JD022296.

Davis, K. J., and Coauthors, 2017: The Indianapolis Flux Experiment (INFLUX): A test-bed for developing urban greenhouse gas emission measurements.

Dijk, A. Van, 2002: *Extension to 3D of "The Effect of Line Averaging on Scalar Flux Measurements with a Sonic Anemometer near the Surface" by Kristensen and Fitzjarrald*.

——, 2003: The principles of surface flux physics. *Energy*,.

Eshonkulov, R., and Coauthors, 2019: Evaluating multi-year, multi-site data on the energy balance closure of eddy-covariance flux measurements at cropland sites in southwestern Germany. *Biogeosciences*, **16**, 521–540, doi:10.5194/bg-16-521-2019.

Fang, L., X. Zhan, C. R. Hain, and J. Liu, 2018: Impact of Using Near Real-Time Green Vegetation Fraction in Noah Land Surface Model of NOAA NCEP on Numerical Weather Predictions. *Adv. Meteorol.*, **2018**, 1–12, doi:10.1155/2018/9256396.

Fang, Y., and Coauthors, 2016: Monthly land cover-specific evapotranspiration models derived from global eddy flux measurements and remote sensing data. *Ecohydrology*, **9**, 248–266, doi:10.1002/eco.1629.

Fitzjarrald, D. R., and G. G. Lala, 1989: Hudson Valley Fog Environments. *J. Appl. Meteorol.*, **28**, 1303–1328.

——, O. C. Acevedo, and K. E. Moore, 2001: Climatic Consequences of Leaf Presence in the Eastern United States. *J. Clim.*, **14**, 598–614, doi:10.1175/1520-0442(2001)014<0598:CCOLPI>2.0.CO;2. https://doi.org/10.1175/1520-0442(2001)014%3C0598:CCOLPI%3E2.0.CO.

Foken, T., 2008: the Energy Balance Closure Problem: an Overview. *Ecol. Appl.*, **18**, 1351–1367.

——, M. Mauder, L. Mahrt, and J. W. Munger, 2006: Post-Field Data Quality Control Chapter 9. doi:10.1007/1-4020-2265-4.

——, M. Aubinet, and R. Leuning, 2012a: The Eddy Covariance Method BT - Eddy Covariance: A Practical Guide to Measurement and Data Analysis. M. Aubinet, T. Vesala, and D. Papale, Eds., Springer Netherlands, Dordrecht, 1–19 https://doi.org/10.1007/978-94-

007-2351-1_1.

——, R. Leuning, S. R. Oncley, M. Mauder, and M. Aubinet, 2012b: Corrections and Data Quality Control BT - Eddy Covariance: A Practical Guide to Measurement and Data Analysis. M. Aubinet, T. Vesala, and D. Papale, Eds., Springer Netherlands, Dordrecht, 85–131 https://doi.org/10.1007/978-94-007-2351-1_4.

Freedman, J. M., D. R. Fitzjarrald, K. E. Moore, and R. K. Sakai, 2001: Boundary layer clouds and vegetation-atmosphere feedbacks. *J. Clim.*, **14**, 180–197, doi:10.1175/1520-0442(2001)013<0180:BLCAVA>2.0.CO;2.

Fröhlich, C., 1991: History of Solar Radiometry and the World Radiometric Reference. *Metrologia*, **28**, 111–115, doi:10.1088/0026-1394/28/3/001. http://dx.doi.org/10.1088/0026-1394/28/3/001.

Garrett, A. J., 1982: A Parameter Study of Interactions Between Convective Clouds, the Convective Boundary Layer, and a Forested Surface. *Mon. Weather Rev.*, **110**, 1041–1059, doi:10.1175/1520-0493(1982)110<1041:apsoib>2.0.co;2.

Geankoplis, C. J., 1993: *Transport processes and unit operations*. 3rd Editio. Prentice-Hall International, Englewood Cliffs, NJ, 114–131 pp. https://books.google.com/books?id=NKRiDwAAQBAJ.

Geiger, R., 1950: *Climate near the ground*. 2nd ed. M.N. Stewart, Ed. Harvard University Press, Cambridge, MA, 518 pp.

Guttman, N. B., and R. G. Quayle, 1996: A Historical Perspective of U.S. Climate Divisions. *Bull. Am. Meteorol. Soc.*, **77**, 293–304, doi:10.1175/1520-0477(1996)077<0293:AHPOUC>2.0.CO;2. https://doi.org/10.1175/1520-0477(1996)077%3C0293:AHPOUC%3E2.0.CO.

Homer, C., and Coauthors, 2015: Completion of the 2011 National Land Cover Database for the conterminous United States–representing a decade of land cover change information. *Photogramm. Eng. Remote Sens.*, **81**, 345–354.

Horst, T. W., and D. H. Lenschow, 2009: Attenuation of scalar fluxes measured with spatially-displaced sensors. *Boundary-Layer Meteorol.*, **130**, 275–300, doi:10.1007/s10546-008-9348-0.

Humes, K. S., W. P. Kustas, M. S. Moran, W. D. Nichols, and M. A. Weltz, 1994: Variability of emissivity and surface temperature over a sparsely vegetated surface. *Water Resour. Res.*, **30**, 1299–1310, doi:10.1029/93WR03065. https://doi.org/10.1029/93WR03065.

Kaimal, J. C., and J. J. Finnigan, 1994: *Atmospheric Boundary Layer Flows*. 289 pp.

——, S. F. Clifford, and R. J. Lataitis, 1989: Effect of finite sampling on atmospheric spectra. *Boundary-Layer Meteorol.*, **47**, 337–347.

Kipp & Zonen B.V., 2014: CNR4 Net Radiometer Instruction Manual. **1409**, 36. http://www.kippzonen.com/Product/85/CNR4-Net-Radiometer#.WaAd9D596Uk (Accessed January 1, 2017).

Kljun, N., P. Calanca, M. W. Rotach, and H. P. Schmid, 2015: A simple two-dimensional parameterisation for Flux Footprint Prediction (FFP). 3695–3713, doi:10.5194/gmd-8-3695-2015.

Mahmood, R., and Coauthors, 2017: MESONETS: Mesoscale weather and climate observations for the United States. *Bull. Am. Meteorol. Soc.*, **98**, 1349–1361, doi:10.1175/BAMS-D-15-00258.1.

Massman, W. J., 2000: A simple method for estimating frequency response corrections for eddy covariance systems. *Agric. For. Meteorol.*, **104**, 185–198, doi:10.1016/S0168-1923(00)00164-7.

Maurer, K. D., B. S. Hardiman, C. S. Vogel, and G. Bohrer, 2013: Canopy-structure effects on surface roughness parameters: Observations in a Great Lakes mixed-deciduous forest. *Agric. For. Meteorol.*, **177**, 24–34, doi:10.1016/j.agrformet.2013.04.002. http://dx.doi.org/10.1016/j.agrformet.2013.04.002.

McPherson, R. A., and Coauthors, 2007: Statewide monitoring of the mesoscale environment: A technical update on the Oklahoma Mesonet. *J. Atmos. Ocean. Technol.*, **24**, 301–321, doi:10.1175/JTECH1976.1.

Metzger, S., D. Durden, C. Sturtevant, H. Luo, N. Pingintha-durden, and T. Sachs, 2017: eddy4R 0.2.0: a DevOps model for community-extensible processing and analysis of eddy-covariance data based on R, Git, Docker, and HDF5. *Geosci. Model Dev.*, **10**, 3189–3206.

Michel, D., R. Philipona, C. Ruckstuhl, R. Vogt, and L. Vuilleumier, 2008: Performance and uncertainty of CNR1 net radiometers during a one-year field comparison. *J. Atmos. Ocean. Technol.*, **25**, 442–451, doi:10.1175/2007JTECHA973.1.

Miller, S. D., M. L. Goulden, M. C. Menton, H. R. da Rocha, H. C. de Freitas, A. M. e S. Figueira, and C. A. Dias de Sousa, 2004: Biometric and micrometeorological measurements of tropical forest carbon balance. *Ecol. Appl.*, **14**, 114–126, doi:10.1890/02-6005. https://doi.org/10.1890/02-6005.

——, and Coauthors, 2011: Reduced impact logging minimally alters tropical rainforest carbon and energy exchange. *Proc. Natl. Acad. Sci.*, **108**, 19431 LP – 19435, doi:10.1073/pnas.1105068108. http://www.pnas.org/content/108/48/19431.abstract.

Mitchell, L. E., and Coauthors, 2018: Long-term urban carbon dioxide observations reveal spatial and temporal dynamics related to urban characteristics and growth. *PNAS*, **115**, 2912–2917, doi:10.1073/pnas.1702393115.

Moncrieff, J. B., and Coauthors, 1997: A system to measure surface fluxes of momentum, sensible heat, water vapour and carbon dioxide. *J. Hydrol.*, **188**–**189**, 589–611, doi:10.1016/S0022-1694(96)03194-0.

Montgomery, R. B., 1947: Viscosity and thermal conductivity of air and diffusivity of water vapor in air. *J. Meteorol.*, **4**, 193–196, doi:10.1175/1520-0469(1947)004<0193:VATCOA>2.0.CO;2. https://doi.org/10.1175/1520-0469(1947)004%3C0193:VATCOA%3E2.0.CO.

Moore, C. J., 1986: Frequency response corrections for eddy correlation systems. *Boundary-*

Layer Meteorol., **37**, 17–35, doi:10.1007/BF00122754.

Munger, J. W., H. W. Loescher, and H. Luo, 2012: Measurement, Tower, and Site Design Considerations BT - Eddy Covariance: A Practical Guide to Measurement and Data Analysis. M. Aubinet, T. Vesala, and D. Papale, Eds., Springer Netherlands, Dordrecht, 21–58 https://doi.org/10.1007/978-94-007-2351-1_2.

Nielsen-Gammon, J. W., X.-M. Hu, F. Zhang, and J. E. Pleim, 2010: Evaluation of Planetary Boundary Layer Scheme Sensitivities for the Purpose of Parameter Estimation. *Mon. Weather Rev.*, **138**, 3400–3417, doi:10.1175/2010MWR3292.1. https://doi.org/10.1175/2010MWR3292.1.

Niu, G. Y., and Coauthors, 2011: The community Noah land surface model with multiparameterization options (Noah-MP): 1. Model description and evaluation with local-scale measurements. *J. Geophys. Res. Atmos.*, **116**, 1–19, doi:10.1029/2010JD015139.

Novick, K. A., J. Walker, W. S. Chan, A. Schmidt, C. Sobek, and J. M. Vose, 2013: Eddy covariance measurements with a new fast-response, enclosed-path analyzer: Spectral characteristics and cross-system comparisons. *Agric. For. Meteorol.*, **181**, 17–32, doi:10.1016/j.agrformet.2013.06.020. http://dx.doi.org/10.1016/j.agrformet.2013.06.020.

NYS GIS Clearinghouse, 2019: LIDAR Coverage in NYS. https://gis.ny.gov/elevation/lidar-coverage.htm (Accessed December 5, 2019).

Pataki, D. E., 2003: Seasonal cycle of carbon dioxide and its isotopic composition in an urban atmosphere: Anthropogenic and biogenic effects. *J. Geophys. Res.*, **108**, 4735, doi:10.1029/2003JD003865. http://doi.wiley.com/10.1029/2003JD003865.

Sakai, R. K., D. R. Fitzjarrald, M. Czikowsky, and J. M. Freedman, 1998: P4.5 mechanisms of wind channeling in the hudson valley, ny. 2–5.

——, ——, and K. E. Moore, 2002: Importance of Low-Frequency Contributions to Eddy Fluxes Observed over Rough Surfaces. *J. Appl. Meteorol.*, **40**, 2178–2192, doi:10.1175/1520-0450(2001)040<2178:iolfct>2.0.co;2.

——, and Coauthors, 2004: Land-use change effects on local energy, water, and carbon balances in an Amazonian agricultural field. *Glob. Chang. Biol.*, **10**, 895–907, doi:10.1111/j.1529-8817.2003.00773.x. https://doi.org/10.1111/j.1529-8817.2003.00773.x.

Savage, M. J., 2012: Estimation of leaf wetness duration for a short- grass surface. **1862**, doi:10.1080/02571862.2012.750017.

Schmidt, A., C. Hanson, W. S. Chan, and B. E. Law, 2012: Empirical assessment of uncertainties of meteorological parameters and turbulent fluxes in the AmeriFlux network. *J. Geophys. Res.*, **117**, doi:10.1029/2012JG002100.

Schotanus, P., F. T. M. Nieuwstadt, and H. A. R. De Bruin, 1983: Temperature measurement with a sonic anemometer and its application to heat and moisture fluxes. *Boundary-Layer Meteorol.*, **26**, 81–93, doi:10.1007/BF00164332.

Shafer, M. A., C. A. Fiebrich, D. S. Arndt, S. E. Fredrickson, and T. W. Hughes, 2000: Quality assurance procedures in the Oklahoma Mesonetwork. *J. Atmos. Ocean. Technol.*, **17**, 474–

494, doi:10.1175/1520-0426(2000)017<0474:QAPITO>2.0.CO;2.

Shapland, T. M., R. L. Snyder, K. T. Paw U, and A. J. McElrone, 2014: Thermocouple frequency response compensation leads to convergence of the surface renewal alpha calibration. *Agric. For. Meteorol.*, **189**–**190**, 36–47, doi:10.1016/j.agrformet.2014.01.008. http://dx.doi.org/10.1016/j.agrformet.2014.01.008.

Starkenburg, D., S. Metzger, G. J. Fochesatto, J. G. Alfieri, R. Gens, A. Prakash, and J. Cristóbal, 2016: Assessment of Despiking Methods for Turbulence Data in Micrometeorology. *J. Atmos. Ocean. Technol.*, **33**, 2001–2013, doi:10.1175/JTECH-D-15-0154.1. https://doi.org/10.1175/JTECH-D-15-0154.1.

Steinhart, J. S., and S. R. Hart, 1968: Calibration curves for thermistors. *Deep. Res. Oceanogr. Abstr.*, **15**, 497–503. http://10.0.3.248/0011-7471(68)90057-0.

Stull, R. B., 1988: *An Introduction to Boundary Layer Meteorology*. Kluwer Academic Publishers, Dordrecht, NL, 666 pp.

Swinbank, W. C., 1951: The measurement of vertical transfer of heat and water vapor by eddies in the lower atmosphere. *J. Meteorol.*, **8**, 135–145, doi:10.1175/1520-0469(1951)008<0135:TMOVTO>2.0.CO;2. https://doi.org/10.1175/1520-0469(1951)008%3C0135:TMOVTO%3E2.0.CO.

Tanner, C. B., and G. W. Thurtell, 1969: *Anemoclinometer Measurements of Reynolds Stress and Heat Transport in the Atmospheric Surface Layer: Final Report*. US Army Electronics Command, Atmospheric Sciences Laboratory TR ECOM 66-G22-F., 1–10 pp. https://books.google.com/books?id=JI4fHQAACAAJ.

Tarboton, D. G., 1994: Measurements and modelling of snow energy balance and sublimation from snow. *Proceedings of the 1994 International Snow Science Workshop*, Snowbird, Utah http://arc.lib.montana.edu/snow-science/item/1342.

Taylor, G. I., and W. N. Shaw, 1915: I. Eddy motion in the atmosphere. *Philos. Trans. R. Soc. London. Ser. A, Contain. Pap. a Math. or Phys. Character*, **215**, 1–26, doi:10.1098/rsta.1915.0001. https://doi.org/10.1098/rsta.1915.0001.

Trenberth, K. E., J. T. Fasullo, and M. A. Balmaseda, 2014: Earth's energy imbalance. *J. Clim.*, **27**, 3129–3144, doi:10.1175/JCLI-D-13-00294.1.

Wallace, J. M., and P. V Hobbs, 2006: *Atmospheric Science: An Introductory Survey*. 2nd ed. Elsevier Science, Amsterdam,.

Webb, E. K., G. I. Pearman, and R. Leuning, 1980: Correction of flux measurements for density effects due to heat and water vapour transfer. *Q. J. R. Meteorol. Soc.*, **106**, 85–100, doi:10.1002/qj.49710644707. https://doi.org/10.1002/qj.49710644707.

Wilson, K., 2002: Energy balance closure at FLUXNET sites. *Agric. For. Meteorol.*, **113**, 223–243, doi:10.1016/S0168-1923(02)00109-0.

——, P. J. Hanson, and D. D. Baldocchi, 2000: Evaporation and energy fluxes beneath a temperate deciduous forest in North America. *Agric. For. Meteorol.*, **102**, 83-103.

APPENDIX

Appendix A. Statistics for terrain slope at flux sites.

Site	Mean Slope within 500 m	Std. Dev. Slope within 500 m	Mean Slope within 1000 m	Std. Dev. Slope within 1000 m
BELL	0.7	0.4	0.8	0.5
BKLN	0.3	0.2	0.3	0.2
BURT	0.2	0.2	0.3	0.3
CHAZ	0.0	0.0	0.0	0.0
FRED	1.1	0.4	1.2	0.7
ONTA	0.6	0.2	0.5	0.2
OWEG	2.7	1.7	4.0	2.4
PENN	2.4	2.4	3.1	3.5
QUEE	1.0	0.9	0.7	0.7
REDF	1.5	0.4	1.4	0.7
REDH	0.6	0.4	0.4	0.5
SCHU	1.8	1.6	1.9	1.4
SOUT	0.3	0.2	0.3	0.2
STAT	0.7	0.6	1.0	0.8
VOOR	0.0	0.0	0.1	0.6
WARS	2.2	1.0	1.8	1.4
WHIT	0.2	0.2	0.7	1.7

Appendix B. Sample checklist used by NYSM technicians for Fall Pass

Flux Fall 2017 Pass for Penn Yan (FLUX_PENN)

This completed form must be submitted to the Mesonet Operations Center for a station visit to be counted. Please use **BLACK INK** to facilitate scanning.

Date: 10/13/17 Arrival Time (UTC): 11:40 Departure: 16:00 Tech(s): NF, SB

1. **Arrival photos, taken prior to any maintenance**
   - ☒ Ground heat flux footprint
   - ☒ Photos showing anything which might affect instrument performance and/or data quality. 2m fan is quite clogged

   Take the following photos only if vegetation needs to be cut, and submit as standard (not flux) site photos.
   - ☒ Soil Plot
   - ☒ SR50A footprint
   - ☒ Inside SW corner to north center showing vegetation height.
   - ☒ Outside photo from the south taken 10' south of fence showing outside vegetation height.

2. **Site vegetation maintenance**
   Was vegetation cut? ☒ Yes ☐ No ☐ Needs cutting, but unable

3. **General maintenance** (Enter **Y**(es), (n)**O**, or **R**(eplaced) in every box)

Cleaning/Leveling	Clean on arrival?	Cleaned?	Level on arrival?	Leveled?
Net Radiometer	O	Y	Y	O
CNF4 Filter	Y	O	[redacted]	
Vortex Filter	Y	O		
Bypass Tubing	Y	O		
Vortex Chamber	Y	O		
Analyzer Windows	Y	O		

4. **Perform site-specific tasks.**

5. **Inspect pump module**
   - ☒ No action needed because water level rise less than half full
   - ☐ Drained water
   - ☐ Unable to complete

6. **Enclosure desiccant** ☐ Good condition ☒ Replaced ☐ Needs replacing, but unable ☐ Was missing, but added ☐ Was missing, still missing

7. **EC100 desiccant** ☐ Good condition ☒ Replaced ☐ Needs replacing, but unable ☐ Was missing, but added ☐ Was missing, still missing

8. **CNR4 drying cartridge** ☐ Good condition ☒ Replaced ☐ Needs replacing, but unable

9. **Departure photos, after all maintenance is complete**
   - ☒ Ground heat flux footprint
   - ☒ Gas cylinder storage box

   Take the following photos only if vegetation was cut, and submit as standard (not flux) site photos.
   - ☒ Soil plot
   - ☒ SR50A footprint
   - ☒ Inside SW corner to north center showing vegetation height
   - ☒ Outside photo from taken 10' south of fence showing outside vegetation height

Site-Specific Tasks

1. **Tickets**

#5159	GROUND_PLATE	XXXX	Traced: 2017-07-17 18:30:39
Install flux ground plates.			
Comments		**S/N Removed**	**S/N Installed**

will record SN and update location once all SNs are collected

Other pass comments:

Tech Signature Nick Ferry **Date Submitted** 10/16/17

Appendix C. Means of meteorological variables at flux sites for 2018. Precipitation Accumulation is given as a sum. Dominant wind direction is the highest frequency wind direction measured throughout the year.